

AD-A182 159

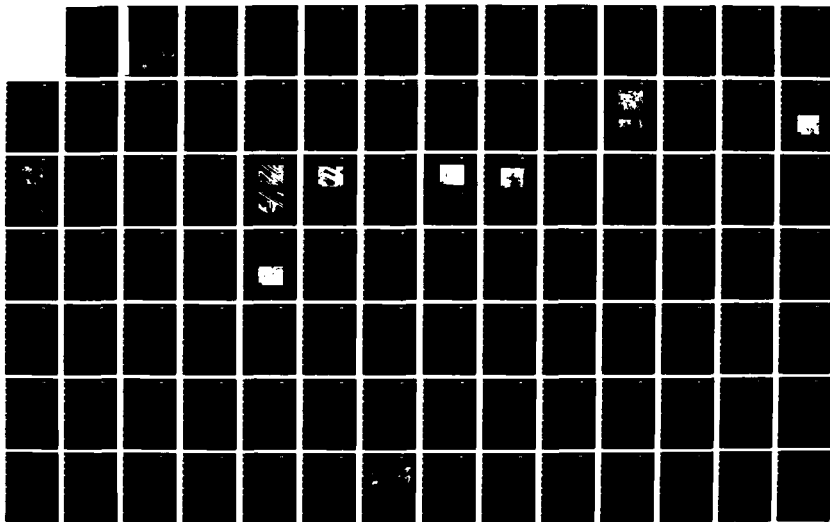
PROCESSING AND PROPERTIES OF AIRFRAME MATERIALS(U)
ROCKWELL INTERNATIONAL THOUSAND OAKS CA SCIENCE CENTER
C G RHODES ET AL JUN 87 SC5358-4FR AFOSR-TR-87-0015
F49620-81-C-0035

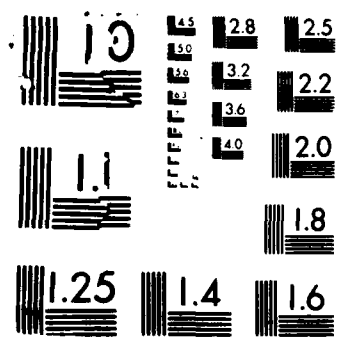
1/2

UNCLASSIFIED

F/G 1/3

NL





SC5358.4FR

AD-A182 159

SC5358.4FR

DTIC FILE COPY

Copy No. 7

PROCESSING AND PROPERTIES OF AIRFRAME MATERIALS

Approved for public release;
distribution unlimited.

FINAL REPORT FOR THE PERIOD
January 01, 1983 through February 28, 1986

CONTRACT NO. F49620-83-C-0055

Prepared for

Air Force Office of Scientific Research
Directorate of Electronic and Materials Sciences
Building 410
Bolling Air Force Base, DC 20332

PART I

C.G. Rhodes, J.C. Chesnutt, J.A. Wert

PART II

A.K. Ghosh

JUNE 1987

DTIC
ELECTE

JUL 06 1987

D

AIR FORCE OFFICE OF SCIENTIFIC RESEARCH (AFSC)
NOTICE OF TRANSMISSION TO DTIC

This technical report has been reviewed and is
approved for public release IAW AFR 190-12.
Distribution is unlimited.

MATTHEW J. KERPER

Chief, Technical Information Division

Approved for public release; distribution unlimited



Rockwell International
Science Center

87 7 2 066

UNCLASSIFIED

SECURITY CLASSIFICATION OF THIS PAGE

REPORT DOCUMENTATION PAGE

1a. REPORT SECURITY CLASSIFICATION UNCLASSIFIED			1b. RESTRICTIVE MARKINGS						
2a. SECURITY CLASSIFICATION AUTHORITY			3. DISTRIBUTION/AVAILABILITY OF REPORT Approved for public release; distribution unlimited						
2b. CLASSIFICATION/DOWNGRADING SCHEDULE									
4. PERFORMING ORGANIZATION REPORT NUMBER(S) SC5358.4FR			5. MONITORING ORGANIZATION REPORT NUMBER(S) AFOSR-TR-87-0815						
6a. NAME OF PERFORMING ORGANIZATION ROCKWELL INTERNATIONAL Science Center		6b. OFFICE SYMBOL (If Applicable) NE		7a. NAME OF MONITORING ORGANIZATION AFOSR/NE					
6c. ADDRESS (City, State, and ZIP Code) 1049 Camino Dos Rios Thousand Oaks, CA 91360			7b. ADDRESS (City, State and ZIP Code) Bldg 410 Bolling AFB, DC 20332-6448						
8a. NAME OF FUNDING/SPONSORING ORGANIZATION Air Force Office of Scientific Research		8b. OFFICE SYMBOL (If Applicable) NE		9. PROCUREMENT INSTRUMENT IDENTIFICATION NUMBER CONTRACT NO. F49620-83-C-0055					
8c. ADDRESS (City, State and ZIP Code) Building 410 Bolling Air Force Base, DC 20332			10. SOURCE OF FUNDING NOS.						
11. TITLE (Include Security Classification) PROCESSING AND PROPERTIES OF AIRFRAME MATERIALS (U)			<table border="1"> <tr> <td>PROGRAM ELEMENT NO. 61102F</td> <td>PROJECT NO. 2306</td> <td>TASK NO. A1</td> <td>WORK UNIT NO.</td> </tr> </table>			PROGRAM ELEMENT NO. 61102F	PROJECT NO. 2306	TASK NO. A1	WORK UNIT NO.
PROGRAM ELEMENT NO. 61102F	PROJECT NO. 2306	TASK NO. A1	WORK UNIT NO.						
12. PERSONAL AUTHOR(S) Rhodes, C.G., Ghosh, A.K., Chesnutt, J.C., Wert, J.A.									
13a. TYPE OF REPORT Final Report		13b. TIME COVERED FROM 01/01/83 TO 12/31/85		14. DATE OF REPORT (Yr., Mo., Day) 1987, JUNE					
15. PAGE COUNT 118									
16. SUPPLEMENTARY NOTATION									
17. COSATI CODES			18. SUBJECT TERMS (Continue on reverse if necessary and identify by block number)						
FIELD	GROUP	SUB. GR.	Metals Processing, Titanium, Aluminum, Fatigue, Superplasticity, Void Closure Powder Consolidation, Cavitation, Dynamic Recrystallization, Dynamic Grain Growth						
19. ABSTRACT (Continue on reverse if necessary and identify by block number)									
<p>This report describes the results of a three-year research program to study the relationship between microstructure and processing conditions and the effect of processing conditions on the performance of structural airframe materials. Part I of the program was an examination of the influence of beta processing methods on the interaction of fatigue cracks with microstructural elements. These beta-phase processing methods were chosen to provide variations in beta-phase volume fraction and continuity, alpha plate size, and alpha colony size in plate and forging material. The microstructures of the beta-processed materials were quantitatively characterized using scanning electron microscopy (SEM) and scanning transmission electron microscopy (STEM). The results have demonstrated that the widespread in da/dN data reported in the literature for beta-processed Ti-6Al/4V tested at R = 0.1 or at R = 0.7 can be accounted for by microstructural variations. Linear regression analyses revealed that beta phase volume fraction was most influential and colony size least influential on fatigue crack growth rates. (KEYWORDS:)</p>									
20. DISTRIBUTION/AVAILABILITY OF ABSTRACT UNCLASSIFIED/UNLIMITED <input checked="" type="checkbox"/> SAME AS RPT. <input type="checkbox"/> DTIC USERS <input type="checkbox"/>			21. ABSTRACT SECURITY CLASSIFICATION UNCLASSIFIED						
22a. NAME OF RESPONSIBLE INDIVIDUAL Rosenstein			22b. TELEPHONE NUMBER (Include Area Code) (202) 49051 373-4545 767-4933		22c. OFFICE SYMBOL NE				

DD FORM 1473, 83 APR

EDITION OF 1 JAN 73 IS OBSOLETE

UNCLASSIFIED

SECURITY CLASSIFICATION OF THIS PAGE

87 7 2 066

UNCLASSIFIED

SECURITY CLASSIFICATION OF THIS PAGE

In Part II, the micromechanics of superplastic deformation was studied to determine how the microstructural variables affect the macroscopic deformation behavior. Experiments were performed with 7475 Al having various grain sizes. The flow stress vs strain rate behavior for the mixed grain size materials is best described using the iso-strain rate concept. Observations of dynamic grain growth and dynamic recrystallization have led to new perceptions of how these processes may alter the mechanical response of the materials during superplastic deformation. Based on these observations, the new dynamic model of the superplastic deformation has been developed. Controlled experiments have revealed that hydrostatic pressure can influence both the nucleation and growth of superplastic voids. An analytical study of the process of pore closure during powder consolidation has been carried out. The study predicts the kinetics of pore closure as well as shape changes occurring internally. Parallel experiments with 7075 aluminum powder and premachined voids have shown excellent agreement with analysis.

UNCLASSIFIED

SECURITY CLASSIFICATION OF THIS PAGE



TABLE OF CONTENTS

	<u>Page</u>
1.0 EXECUTIVE SUMMARY	1
2.0 INTRODUCTION	5
3.0 PART I - EFFECT OF PROCESSING ON MICROSTRUCTURE AND DESIGN PROPERTIES OF TITANIUM AIRFRAME ALLOYS.....	8
3.1 Background	8
3.2 Experimental Procedures	9
3.3 Result	10
3.3.1 Materials	10
3.3.2 Microstructural Development	11
3.3.3 Tensile Properties	24
3.3.4 Fatigue Crack Propagation and Crack Path Analysis	25
3.4 Discussion	59
3.4.1 Microstructure	59
3.4.2 Fatigue Crack Propagation Behavior	60
3.4.3 Correlation of Crack Propagation with Microstructure	62
3.5 Conclusions	65
3.6 Part I - References	67
4.0 MECHANISTIC ASPECTS OF SUPERPLASTICITY IN Al ALLOYS	69
4.1 Background	69
4.2 Objectives	71
4.3 Progress	71
4.3.1 Microstructural Changes	75
4.3.2 Progress in Superplastic Cavitation	90
4.3.3 Progress in the Understanding of Consolidation of Al Alloy Powder	92
4.4 Part II - References	105
5.0 ACTIVITIES	107
5.1 Publications	107
5.2 Personnel Associated with Research, Part I	107
5.3 Personnel Associated with Research, Part II	107
5.4 Interaction (Coupling Activities)	107



A-1



LIST OF FIGURES

<u>Figure</u>		<u>Page</u>
3.3-1	Light micrograph of Ti-6Al-4V plate material, after beta treatment of 1025°C/10 min/AC	12
3.3-2	Light micrograph of Ti-6Al-4V forged material, as forged	12
3.3-3	SEM of Ti-6Al-4V plate given heat treatment No. 1. Beta phase is white	15
3.3-4	SEM of Ti-6Al-4V, plate, given heat treatment No. 2. Beta phase is white	16
3.3-5	SEM of Ti-6Al-4V, plate, given heat treatment No. 3. Beta phase is white	16
3.3-6	LM of Ti-6Al-4V plate give heat treatment No. 1. Alpha phase is light, beta phase is dark	17
3.3-7	LM of Ti-6Al-4V plate given heat treatment No. 2. Alpha phase is light, beta phase is dark	18
3.3-8	LM of Ti-6Al-4V plate given heat treatment No. 3. Alpha phase is light, beta phase is dark	18
3.3-9	TEM of Ti-6Al-4V plate given heat treatment No. 1	20
3.3-10	TEM of Ti-6Al-4V plate given heat treatment No. 2	20
3.3-11	TEM of Ti-6Al-4V plate given heat treatment No. 3	21
3.3-12	LM of Ti-6Al-4V forging, as-forged	23
3.3-13	LM of Ti-6Al-4V given heat treatment No. 2	23
3.3-14	LM of Ti-6Al-4V given heat treatment No. 3	24
3.3-15	da/dN vs ΔK for plate material, heat treatment No. 1, $R = 0.1$	26
3.3-16	da/dN vs ΔK for plate material, heat treatment No. 2, $R = 0.1$	26
3.3-17	da/dN vs ΔK for plate material, heat treatment No. 3, $R = 0.1$	27
3.3-18	da/dN vs ΔK , special test of plate material, heat treatment No. 1, $R = 0.1$	28



LIST OF FIGURES (continued)

<u>Figure</u>		<u>Page</u>
3.3-19	da/dN vs crack length, special test of plate material, R = 0.1	28
3.3-20	Lineal roughness vs ΔK for plate material, heat treatment No. 1, including load shed, load increment segments, R = 0.1	29
3.3-21	Lineal roughness vs ΔK for plate material, heat treatment No. 2, including load shed and load increment segments, R = 0.1	30
3.3-22	Lineal roughness vs ΔK for plate materials, heat treatment No. 3, including load shed and load increment segments, R = 0.1	30
3.3-23	Secondary cracking vs ΔK for plate material, heat treatment No. 1, including load shed and load increment segments, R = 0.1	31
3.3-24	Secondary cracking vs ΔK for plate material, heat treatment No. 2, including load shed and load increment segments, R = 0.1	31
3.3-25	Secondary cracking vs ΔK for plate material, heat treatment No. 3, including load shed and load increment segments, R = 0.1	32
3.3-26	Total da/dN (see text) vs ΔK for plate material, heat treatment No. 1, including load shed and load increment segments, R = 0.1	33
3.3-27	da/dN vs ΔK for plate material, heat treatment Nos. 1, 2, 3. Load increment data only, R = 0.1	33
3.3-28	SEM of crack moving across alpha colony boundary maintaining high angle with alpha plates	34
3.3-29	Lineal roughness vs ΔK for plate material, heat treatments No. 1, 2, 3. Load increment data only, R = 0.1	35
3.3-30	Ratio of crack branching to main crack vs ΔK for plate material, heat treatments No. 1, 2, 3, R = 0.1	36
3.3-31	da/dN vs ΔK , forged material, as-forged, R = 0.1	37
3.3-32	da/dN vs ΔK , forged material, heat treatment No. 2, R = 0.1	37
3.3-33	da/dN vs ΔK , forged material, heat treatment No. 3, R = 0.1	38
3.3-34	Lineal roughness vs ΔK , forged material, as-forged, including load shed and load increment segments, R = 0.1	38



LIST OF FIGURES (continued)

<u>Figure</u>		<u>Page</u>
3.3-35	Lineal roughness vs ΔK , forged materials, heat treatment No. 2, including load shed and load increment segments, $R = 0.1$	39
3.3-36	Lineal roughness vs ΔK , forged materials, heat treatment No. 3, including load shed and load increment segments, $R = 0.1$	39
3.3-37	Secondary cracking vs ΔK , forged materials, as-forged, including load shed and load increment segments, $R = 0.1$	40
3.3-38	Secondary cracking vs ΔK , forged materials, as-forged, heat treatment No. 2, including load shed and load increment segments, $R = 0.1$	41
3.3-39	Secondary cracking vs ΔK , forged materials, as-forged, heat treatment No. 3, including load shed and load increment segments, $R = 0.1$	41
3.3-40	da/dN vs ΔK , forged material, heat treatments No. 1, 2, 3 load increment data only, $R = 0.1$	42
3.3-41	Lineal roughness vs ΔK , forged material, heat treatments No. 1, 2, 3, load increment data only, $R = 0.1$	43
3.3-42	Secondary cracking vs ΔK , forged material, heat treatments 1, 2, 3, load increment data only, $R = 0.1$	44
3.3-43	Measured da/dN vs calculated da/dN at $R = 0.1$ for plate and forged materials, using Eq. (1)	46
3.3-44	da/dN vs volume fraction beta phase at $R = 0.1$, using Eq. (1)	46
3.3-45	da/dN vs beta phase discontinuities at $R = 0.1$, using Eq. (1)	47
3.3-46	da/dN vs alpha plate width at $R = 0.1$, using Eq. (1)	47
3.3-47	da/dN vs alpha colony size at $R = 0.1$, using Eq. (1)	48
3.3-48	da/dN vs ΔK , plate material, heat treatments No. 1, 2, 3, $R = 0.7$	49
3.3-49	Lineal roughness vs ΔK , plate material, heat treatments No. 1, 2, 3, load increment data only, $R = 0.7$	50



LIST OF FIGURES (continued)

<u>Figure</u>		<u>Page</u>
3.3-50	Secondary cracking vs ΔK , plate material, heat treatment No. 1, 2, 3, load increment data only, $R = 0.7$	50
3.3-51	Comparison of da/dN vs ΔK , plate material, heat treatment No. 1, at $R = 0.1$ and $R = 0.7$	51
3.3-52	Comparison of da/dN vs ΔK , plate material, heat treatment No. 2, at $R = 0.1$, $R = 0.7$	52
3.3-53	Comparison of da/dN vs ΔK , plate material, heat treatment No. 3, at $R = 0.1$, $R = 0.7$	52
3.3-54	da/dN vs ΔK , forged material, heat treatments No. 1, 2, 3	53
3.3-55	Lineal roughness vs ΔK , forged material, heat treatment No. 1, 2, 3, load increment data only, $R = 0.7$	54
3.3-56	Secondary cracking vs ΔK , forged material, heat treatments No. 1, 2, 3, load increment data only, $R = 0.7$	54
3.3-57	da/dN vs ΔK , forged material, as forged, at $R = 0.1$ and $R = 0.7$	55
3.3-58	da/dN vs ΔK , forged material, heat treatment No. 2, at $R = 0.1$ and $R = 0.7$	56
3.3-59	da/dN vs ΔK , forged material, heat treatment No. 3 at $R = 0.1$ and $R = 0.7$	56
3.3-60	Measured da/dN vs calculated da/dN , at $R = 0.7$ for plate and forged materials using Eq. (2)	58
4.3-1	Grain structures of the constituent fine grain (1), coarse grain (b) materials, and the resultant mixed grain model material (c). All sections in LS plane for 7475 Al. Average grain sizes are 12, 75 and 45 μm , respectively	73
4.3-2	(a) Stress vs strain-rate data from step strain-rate test, and (b) m (slope of (a)) vs strain rate for three different grain size conditions	74
4.3-3	Stress strain curves at various constant strain rates for (a) fine grain, (b) coarse grain, and (c) mixed grain size 7475 Al alloys	76



LIST OF FIGURES (continued)

<u>Figure</u>		<u>Page</u>
4.3-4	Dynamic grain growth from interrupted tests at various constant strain rates compared with static grain growth for the fine grain 7475 Al	77
4.3-5	Microstructure for coarse grain 7475 Al; (a) zero strain, (b) $\epsilon = 0.55$ at 516°C , $\dot{\epsilon} = 2 \times 10^{-4} \text{ s}^{-1}$	78
4.3-6	Distribution of grain intercept along rolling direction after various strain levels for (a) fine grain and (b) coarse grain 7475 Al	79
4.3-7	The transition from diffusion to power-law creep depends on the grain size. This transition can be characterized in terms of a strain rate $\dot{\epsilon}^*(L)$ which is a function of the grain size L	80
4.3-8	Stress-strain curves for superplastic 7475 Al at various strain rates	82
4.3-9	Strain-induced grain refinement function assumed during dislocation creep. q is the volume fraction of the original material which is recrystallized, and ϵ_c is a pseudo-nucleation strain. A gradual transition in (a) might be justified on the basis that the nucleation strains may have a distribution of values. An alternative is a single value as illustrated in (b)	85
4.3-10	Possible mechanism of strain-induced grain growth during superplastic flow	87
4.3-11	The computed stress-strain behavior at various strain rates for a bimodal initial grain size. $a = 2.5$, $b = 5$ and $\epsilon_c = 4$. σ is normalized with respect to σ_0^* and ϵ is normalized with respect to ϵ_0^*	88
4.3-12	Initial and final grain size distributions obtained for the stress-strain curves in Fig. 4.3-11	89
4.3-13	Superplastic cavitation under two test conditions: (1) without hydrostatic pressure; and (2) with 600 psi pressure to a strain of 1.0, then no hydrostatic pressure	91
4.3-14	Superplastic cavitation under two test conditions: (1) without pressure; and (3) without pressure up to $\epsilon = 1.0$, then with 600 psi pressure to failure	92



LIST OF FIGURES (continued)

<u>Figure</u>		<u>Page</u>
4.3-15	Strain states in various powder compaction processes	94
4.3-16	(a) Representative volume element showing spherical void for analysis; (b) a section of a horizontal slab for analysis	95
4.3-17	Progressive closure of a spherical void under different states of deformation	98
4.3-18	Void closure under different states as functions of compressive strain and void surface area	100
4.3-19	Void closure in 7075 Al powder, first undergoing hot pressing, then pure compression	102
4.3-20	Micrographs of 7075 Al powder compact at two stages of consolidation (460°C)	102
4.3-21	Micrographs of 7075 Al powder compact at three stages of consolidation (482°C)	103
4.3-22	High rate compaction of 7075 Al powder showing dynamic recrystallization effects and particle flow	103
4.3-23	Progressive void closure in samples containing premachined spherical voids	104
4.3-24	Void closure under various stress states - prediction vs experiment	105



LIST OF TABLES

<u>Table</u>		<u>Page</u>
3.2.1	Chemical Compositions of Ti-6Al-4V Lots	9
3.3-1	Heat Treatment Schedule to Follow Beta Anneal	14
3.3-2	Volume Fraction and Discontinuity of Beta Phase in Ti-6Al-4V Plate	15
3.3-3	Alpha Phase Dimensions in Ti-6Al-4V Plate	17
3.3-4	Compositions of Alpha and Beta Phases in Ti-6Al-4V Plate	19
3.3-5	Volume Fraction and Discontinuity of Beta Phase in Forged Ti-6Al-4V	22
3.3-6	Alpha Phase Dimensions in Forged Ti-6Al-4V	22
3.3-7	Tensile Properties of Plate Material	25
3.3-8	Tensile Properties of Forged Material	25
3.4-1	Specimen Width:Colony Size for Ti-6Al-4V	63



1.0 EXECUTIVE SUMMARY

This report describes the results of a three-year program in which two important aspects of processing of airframe materials were investigated. The objectives of this two-part program were to understand the relationship between microstructure and processing conditions, and how the processing conditions influence the performance of structural airframe materials. In Part I, microstructural characteristics of beta-processed titanium alloys were correlated with the fracture path through the microstructure and with tensile and fatigue crack propagation properties. In Part II, several mechanistic aspects of superplastic forming of high-strength aluminum alloys were investigated to aid in understanding the importance of grain size and grain size distribution on superplastic forming of I/M and P/M alloys.

Part I of the program was an examination of the influence of beta-processing methods on the interaction of fatigue cracks with microstructural elements. These beta-phase processing methods were chosen to provide variations in beta-phase continuity, alpha- and beta-volume fractions, alpha plate size, and alpha colony size in plate and forged materials. Microstructures of the beta-processed materials were quantitatively characterized using scanning electron microscopy and scanning/transmission electron microscopy.

The results have demonstrated that the wide spread in da/dN data reported in the literature for beta-processed Ti-6Al-4V tested at $R = 0.1$ or at $R = 0.7$ can be accounted for by microstructural variations. The mechanisms by which microstructure influences crack propagation rates are (1) changing the inherent resistance to crack propagation by altering the reversed plastic zone size through changes in the yield strength (2) changing the direction of the advancing crack to produce varying degrees of crack path tortuosity, and (3) changing the tendency for bifurcation of the crack.

Linear regression analysis was used to describe the manner by which volume fraction beta phase, continuity of beta phase, width of alpha phase plates, and size of Widmanstätten alpha colonies influence fatigue crack propagation rates in beta-treated Ti-6Al-4V. This analysis, for tests conducted at $R = 0.1$, showed that fatigue crack propagation resistance can be improved by decreasing the volume fraction and continuity



of the beta phase, by decreasing the alpha plate width, or decreasing the Widmanstatten alpha colony size. The extent to which each of these microstructural features influences crack growth rate varies: beta phase volume fraction is found to be the most influential while colony size is the least influential. The regression analysis was performed on the combined data from both plate and forged materials, hence, the microstructural analysis holds for both.

Crack growth rates are significantly faster at $R = 0.7$ than at $R = 0.1$ for all microstructural conditions, which can be explained in terms of roughness-induced crack closure. Regression analysis for plate and forged materials tested at $R = 0.7$ showed similar results to those for tests at $R = 0.1$. That is, fatigue crack growth resistance at $R = 0.7$ can be improved by reducing the volume fraction of beta phase and the width of alpha plates. Again, volume fraction of beta phase was found to be the most influential and Widmanstatten alpha colony size the least influential.

An unusual result was observed during load shed test conditions: crack growth rates for both plate and forged material at $R = 0.1$ were faster during K-decreasing (load shedding) test segments compared to K-increasing (load increment) test regimes. Crack path analyses revealed that there was significantly more crack path tortuosity and secondary cracking during the K-increasing test segment, thereby correlating with slower growth rates. Although the reasons for the change in crack path behavior during the K-increasing portions of the tests are not clear and can only be speculated upon at this time, it is apparent that the stress conditions in and around the crack tip are different for the different test conditions.

Superplastic forming is a process of considerable interest for fabricating aerospace components. In Part II of the program, several aspects of superplasticity mechanisms and powder consolidation have been examined in aluminum-base I/M and P/M alloys. Superplasticity mechanisms were examined in high-strength alloy 7475, which was thermomechanically processed to fine grain size. Model materials fabricated by combining coarse and fine grains showed that overall flow behavior follows isostrain composite behavior rather than isostress in the various grains.

In this real material, a distributed grain size leads to mixed mode deformation with corresponding stress-strain behavior, since the fine grain size regions deform by



diffusional creep and the coarse grain regions by dislocation creep. The grain size distribution can change during deformation since strain is known to produce grain growth when a polycrystal deforms predominantly by diffusion creep, and grain refinement when it deforms by dislocation creep. New evidence of this has been found for 7475 Al, and it is clear that both grain growth and refinement can be simultaneously present in the same material during superplastic flow. Numerical calculations based on these assumptions predict the change in the grain size distribution with strain, as well as the resulting stress-strain behavior under constant strain rate. In general, we find that the model predicts stress-strain behavior consisting of three stages. In the first stage, the flow stress increases with strain, in the second stage, it reaches a plateau, and in the third stage, the flow stress oscillates with strain. The amplitude of the oscillation tends to increase as the applied strain increases. Generally, at slow strain rates, Stage I is more pronounced, while at high strain rates, Stage II is dominant. The shape of the stress-strain curves is in qualitative agreement with results from superplastic Al.

The model contains assumptions regarding the form of the equations used to describe grain growth during diffusional creep and grain refinement during dislocation creep. Grain growth has been assumed to be linear with strain, while grain refinement was assumed to vary sigmoidally with strain which is typical of nucleation and growth phenomena.

An examination of superplastic cavitation in 7475 Al has been carried out to pinpoint the influence of hydrostatic pressure on the nucleation and growth of voids in these alloys. By prenucleating voids during superplastic straining and using hydrostatic pressure during subsequent straining, it is possible to close up voids, which are previously produced. Furthermore, by maintaining a sufficiently high hydrostatic pressure during superplastic forming, the nucleation of voids may be delayed to a very large strain. Thus, it has been found that hydrostatic pressure can influence both the nucleation and growth of cavities.

Since emerging P/M aluminum alloys are of considerable interest in aerospace structures, consolidation science of these materials must be properly understood. A model of void closure has been developed for these materials and parallel experiments were carried out with P/M 7075 alloy to verify the plasticity-based model. It has been



demonstrated that uniaxial compression (with no constraints) is not a suitable means of consolidation, even though oxide breakup is caused by emerging new surfaces. The model agrees well with experimentally determined void shape changes. Small shear stresses when present in conjunction with hydrostatic compression provides the best condition for consolidation. Dynamic recrystallization leads to "necklace" grain formation at prior particle boundaries which aids in increased shear in these areas to aid the consolidation process.



2.0 INTRODUCTION

Structural properties of airframe materials depend on the processing methods used for component fabrication. The processing methods can either be separate heat treatments designed to produce specific properties, or they can be fabrication steps, such as forging or forming operations. This report describes the results of a three-year program to investigate two important aspects of processing of airframe materials.

The overall objectives of this two-part program were to understand the relationship between microstructure and processing conditions, and how the processing conditions influence the performance of structural airframe materials. In Part I, microstructural characteristics of beta processed titanium alloys were correlated with the fracture path through the microstructure and with tensile and fatigue crack propagation properties. In Part II, several mechanistic aspects of superplastic forming of high strength aluminum alloys were investigated to aid in understanding the importance of grain size and grain size distribution on superplastic forming of I/M and P/M Al alloys.

Beta processed Ti alloys, investigated in Part I, can display attractive combinations of strength and fatigue crack propagation (FCP) resistance. However, beta processed alloys have not been used extensively for airframe applications and the microstructures are not well characterized compared with conventional alpha-beta processed alloys. Furthermore, a wide range of fatigue crack propagation rates are often found for similar beta processing routes. This program was designed to enhance our understanding of the relationship between processing, microstructure, and FCP properties of beta processed Ti alloys.

Several beta processing routes for Ti-6Al-4V were investigated. The effect of these processing steps on the microstructure in both plate and forged material were carefully characterized to understand the effect of the processing method on features such as phase morphology, phase composition, and continuity of the retained beta phase. The effect of processing method on FCP properties was also studied to correlate with microstructural results. The paths that fatigue cracks follow through the various microstructures were determined. Combination of these results have led to an understanding of how the various microstructural features control fatigue crack propagation.



Such understanding will allow selection of beta processing routes that provide attractive property combinations for airframe components designed to damage tolerant specifications.

Part II of this program is concerned with superplastic forming of metals. The value of superplastic forming (SPF) as a cost-effective method of fabricating structurally efficient aerospace components is becoming increasingly apparent.¹⁻³ Significant cost and weight reductions have been demonstrated over conventional fabrication methods. While this technology is reasonably well developed for Ti alloys, high strength Al alloys provide a potentially larger application of SPF technology. This is because of the very widespread use of aluminum in aircraft, spacecraft and missile applications.

A processing method has been developed at the Rockwell International Science Center to impart superplasticity to 7475 Al which has demonstrated the capability of being formed into complex structural components.³ The primary development has been a thermomechanical processing method for grain refinement, which provides the fine grain size necessary for superplasticity. Aspects of the grain refinement process and its effect on service properties of 7075 Al were previously investigated under AFOSR sponsorship.⁴ However, development of superplastic aluminum is at a relatively early stage, and the importance of various microstructural features such as grain size distribution are not yet understood. Furthermore, much emphasis is currently being placed on P/M Al alloys that offer high strength levels. Development of superplasticity in these alloys would provide benefits from both high strength and improved formability.

In Part II, with an aim of developing an understanding of the role of key microstructural variables on superplasticity of single phase materials, critical experiments were made to assess the roles of grain size distribution, dynamic grain growth, and dynamic recrystallization effects during superplastic flow in a fine grain 7475 Al alloy. Model material, fabricated by mixing a specific fine and coarse grain combination, has shown that stress-strain rate characteristics, m values, and stress vs strain curves are intermediate between the data for the individual grain size materials. The composite data are best described by an iso-strain rate assumption applied on the constituent fine and coarse grains. Studies on microstructural changes indicated that dynamic grain growth, although significantly more rapid than static growth, is relatively



sensitive to applied strain rate. The distribution of grain size, including the median size, moves to larger sizes with increasing superplastic deformation. While dynamic growth is most common for the finer grains and slower strain rates, the coarser grains and higher strain rates give rise to concurrent grain refinement (i.e., dynamic recrystallization). Based on these observations, a model has been developed that incorporates (1) the gradual development of dislocation structure, (2) enhancement of diffusional creep rates with increasing grain deformation rate, and (3) dynamic grain growth. The model predicts strain hardening occurring from grain growth effects as well as stress oscillations arising from flow softening due to concurrent refinement effects. With regard to cavitation during superplastic forming and the suppression of cavitation by using hydrostatic pressure controversy existed on the role of pressure on nucleation or growth voids. Critical experiments were designed to address this issue in this program.

With the advent of high strength RSP aluminum alloys, considerable interest exists for superplastic forming of the alloys. However, the first order priority is to consolidate a void-free and metallurgically bonded, well consolidated powder compact for thermomechanical processing. In this report, an analytical study of the powder consolidation process was carried out to examine the degree of consolidation and powder oxide breakup occurring under a variety of deformation conditions. Both powder alloy 7075, as well as premachined void samples of 7475 aluminum, are utilized to conduct compaction studies and develop a better understanding of the micromechanics of void consolidation in aluminum.



3.0 PART I - EFFECT OF PROCESSING ON MICROSTRUCTURE AND DESIGN PROPERTIES OF TITANIUM AIRFRAME ALLOYS

3.1 Background

Current and future generation high performance aircraft are being designed with alloys that have high specific strength levels. Current design philosophies utilize the Air Force structural integrity philosophy, as described in military standard MIL-STD-1530A, Aircraft Structural Integrity Program, Airplane Requirements. Inherent in this design philosophy is a requirement for resistance to fatigue crack propagation (FCP). This emphasis upon damage tolerant design and fatigue crack propagation resistant materials has led to consideration of beta processed Ti alloys for fracture-critical applications. In the context of this program, beta processing refers to microstructures that have been produced by either working above the beta transus, heat treating above the beta transus subsequent to working operations, or a combination of the two. The titanium alloy Ti-6Al-4V has been utilized in such fracture critical designs, but requires a special heat treatment, termed recrystallization anneal, to provide adequate toughness and FCP resistance.

A significant potential also exists for replacing components which are extensively machined with precision forged Ti alloys. Forging at temperatures above the beta transus, where the flow stress is significantly reduced, would allow production of more complex geometries than are possible by forging below the beta transus.

The effect of processing above the beta transus on microstructure and fatigue crack propagation resistance has not been well characterized. In a study at the Rockwell International Science Center, Rhodes has evaluated the effect of processing below the beta transus on fracture properties of Ti-6Al-4V. His results showed that the fracture properties could be correlated with the distribution and morphology of the alpha and beta phases, and with the chemical partitioning between the two phases.¹ A second program showed that the distribution and continuity of the retained beta phase affected the fracture toughness of beta processed Ti alloys of various compositions.²

Although beta processing can lead to improved fatigue crack propagation resistance in Ti alloys, there is an attendant increase in the variation of crack propagation rates compared to alpha-beta processed alloys. It is thought that much of this variability



in properties stems from the path that the fatigue cracks follow through the microstructure and the crack's interaction with various microstructural features. Part I of this program was an examination of the relationships between microstructure, crack path, and FCP properties.

3.2 Experimental Procedures

Ti-6Al-4V was obtained in two different processed conditions: plate and forging. The plate material was finish rolled below the beta transus to a final thickness of 19 mm. The forged material was upset forged into pancake, finishing through the beta transus to a final thickness of 57 mm. The analyzed compositions of the two lots of material are given in Table 3.2-1.

Table 3.2-1
Chemical Compositions of Ti-6Al-4V Lots

Lot	Al	Element, b. weight percent					Ti
		V	O	C	N	H	
Plate	6.08	3.98	0.124	0.015	0.009	0.0074	Bal.
Forging	6.00	3.80	0.13	0.040	0.008	0.0050	Bal.

All heat treatments were carried out in vacuum furnaces equipped with programmable controllers.

Tensile tests were conducted in accordance with ASTM E8 using an Instron test machine with a 90kN load cell. Specimens with a 6.4 mm diameter by 25.4 mm long gauge length were tested at a strain rate of $1.67 \cdot 10^{-4} \text{ s}^{-1}$.

Fatigue crack propagation measurements were made on MTS computer controlled testing machines in accordance with the proposed ASTM standard test method using the load shedding technique down to a crack growth rate of $\sim 1 \cdot 10^{-7} \text{ mm/cycle}$. Upon reaching this growth rate, several data points were obtained at constant load. The load was then incrementally increased, with two or three data points being obtained at



each load. All other test conditions conformed to ASTM E647 using a compact tension type specimen with $B = 12.7$ mm and $W = 50$ mm. Tests were conducted in laboratory air (~ 50% relative humidity) at a frequency of 30 Hz. Crack extensions were measured by microscopic examination of prepolished surfaces.

Metallographic examinations of the crack paths were made at the centers of the compact tension specimens on a plane normal to the plane of the crack and parallel to the crack propagation direction. After completion of the fatigue test, each specimen was sectioned longitudinally to expose the center plane. Metallographic preparation then allowed examination of the specimens in regions of plane strain.

Quantification of the microstructure was made by various techniques. Volume fraction of beta phase was measured using the point count method³ on scanning electron microscope (SEM) images. Beta phase discontinuities were measured by counting the number of terminations of beta phase strips per area on a polished and etched surface, again on SEM images. Lineal roughness⁴ and roughness profile⁴ were measured using a Videoplan 2 computerized image analysis instrument.

3.3 Results

3.3.1 Materials

Crystallographic texture is an effect that can influence mechanical properties in alpha/beta titanium alloys that have been unidirectionally formed, such as rolling to plate.⁵ However, it has been well documented that heating above the beta transus will eliminate texture effects.^{6,7} Therefore, no texture measurements were made on the plate material used in this program, as it is assumed that no significant texture effects would be present in the beta processed condition. Nevertheless, all test specimens, fatigue and tensile, were extracted from the plate in the T-L orientation, i.e. the crack propagated in the rolling direction in a plane perpendicular to the rolling plane.

Because of the nature of the deformation, titanium alloy forgings generally have weak texture,⁸ and such is assumed in the present case. A more common problem with forgings is a change in microstructure from center to surface because of cooling rate variations within the workpiece during forging. Metallographic samples taken from



several positions in the pancake forging indicated a slight, but not significant, variation in size of prior beta grains and alpha plates from center to surface. All test specimens, fatigue and tensile, were taken from the forging in the C-R orientation.

3.3.2 Microstructural Development

3.3.2.1 Heat Treatments

The plate material, having been finished in the alpha/beta phase field, required a beta heat treatment to develop the transformed beta microstructure. The two significant microstructural features that must be considered when Ti alloys are processed in the beta phase field are the beta grain size and grain boundary alpha. Yoder and co-workers^{9,10} demonstrated that an increased beta grain size is beneficial for fatigue crack propagation resistance, but detrimental to tensile strength and ductility. In this program, it was decided to select a beta grain size intermediate to those examined by Yoder, et al, so that neither the FCP resistance nor the tensile properties would be seriously degraded. The solution treatment selected for these studies was a 10 min exposure at 1025°C (beta transus + 25°C). Grain boundary alpha forms at beta phase grain boundaries during cooling from above the beta transus. The amount of grain boundary alpha present in the microstructure is a function of the cooling rate, with more alpha forming as the cooling rate decreases. However, because thick sections of Ti-6Al-4V used in airframe applications cannot always be cooled rapidly enough to preclude grain boundary alpha, the beta anneal treatment has been followed by an air cool rather than a quench. Although this procedure results in the formation of grain boundary alpha, it will closely simulate the sort of microstructure that will be present in thick sections. Figure 3.3-1 illustrates the beta annealed microstructure of the plate material.

The forging was beta finished, and therefore required no subsequent beta heat treatment. In this way, comparisons can be made between transformed beta microstructures that have been produced by different processes: viz. heat treatment vs thermo-mechanically processed. As was the case for the heat treated plate, there is some grain boundary alpha present in the as-forged microstructure, Fig. 3.3-2.



SC27904

SC5358.4FR



Fig.3.3-1 Light micrograph of Ti-6Al-4V plate material, after beta treatment of 1025°C/10 min/AC.

SC40704

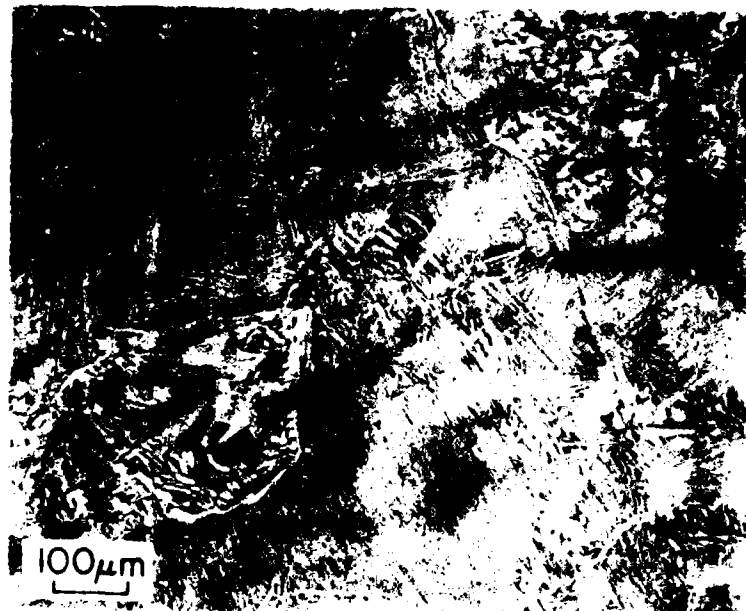


Fig.3.3-2 Light micrograph of Ti-6Al-4V material, as forged.



The objective of this program was to study the influence of beta-processed microstructure on fatigue crack propagation. The microstructure of a beta-processed titanium alloy such as Ti-6Al-4V can vary significantly depending upon the type of processing that the alloy undergoes. Those features that may affect fatigue properties are volume fractions and compositions of alpha and beta phases, size of alpha and beta grains, and continuity of beta phase. Heat treatments that follow the beta anneal have been devised to systematically vary these elements of the microstructure so that their effect on fatigue may be evaluated.

The three heat treatments that have been used in this study are listed in Table 3.3-1. Treatment No. 1 involves a hold midway in the alpha-beta phase field to generate a moderate amount of discontinuous beta phase, followed by an air cool, which will result in a fairly fine alpha plate size with a high aspect ratio. Treatment No. 3 includes a very slow cool from just above the beta transus to room temperature to develop a low volume fraction of continuous beta phase and a coarse alpha plate size with a moderate aspect ratio. Treatment No. 2 is intended to produce microstructures intermediate to those generated by Treatments No. 1 and No. 3. To achieve this, the alloy is held for a short time high in the alpha + beta phase field to provide some coarsening of the pre-existing beta phase, followed by a slow cool to develop larger alpha plate size and continuity of the beta phase. Finally, air cooling from a temperature midway in the alpha + beta phase field essentially retains the alpha-beta mixture attained during the slow cooling step.

The plate material received the three heat treats listed in Table 3.3-1. The forged material, on the other hand, was tested in the as-forged condition in lieu of heat treatment No. 1. The forging was also tested in Conditions No. 2 and No. 3.

3.3.2.2 Microstructural Characterization, Plate

The beta annealed condition, Fig. 3.3-1, has a prior beta grain size of about 350 micrometers and nearly continuous grain boundary alpha that is approximately 3 micrometers wide. None of the three post-beta anneal heat treatments significantly alters the prior beta grain size or the amount of grain boundary alpha.



Table 3.3-1
Heat Treatment Schedule to Follow Beta Anneal

Condition No.	Treatment
1	750°C/1 h/air cool
2	925°C/30 min/cool at 60°C/h to 750°C/air cool
3	1000°C/10 min/cool at 50°C/h to room temperature

The volume fractions, compositions and dimensions of alpha and beta grains, and continuity of beta phase have been evaluated as function of heat treatment. Table 3.3-2 lists the volume fractions and continuity of beta phase for the three treatments. As anticipated, Condition No. 1 exhibits the largest volume fraction of beta phase and a more discontinuous beta phase. Figures 3.3-3 through 3.3-5 illustrate the relative distributions of beta phase in the three heat treatment conditions. Continuity of the beta phase is reported as discontinuities per cubic centimeter of alloy, and is measured by counting the number of terminations of beta strips per area on a polished and etched surface. Clearly, then, a larger number of discontinuities represents a less continuous beta phase. Although the number of discontinuities will be related to the volume fraction of beta phase, there is not a simple one-to-one ratio for the heat treatments utilized in this study. Hence, whether the discontinuities are reported as the absolute values measured (as listed in Table 3.3-2) or as values normalized to volume fraction beta, heat treatment No. 1 results in more than an order of magnitude greater number of discontinuities than treatments No. 2 or No. 3. The heat treatments have succeeded in varying the volume fraction of beta phase by a factor of two, and beta phase discontinuity by more than an order of magnitude.

The alpha phase parameters are listed in Table 3.3-3. Treatment No. 1 has resulted in the finest alpha plate size and the largest aspect ratio, while Treatment No. 3, as expected, has produced the largest alpha plate size and the smallest aspect ratio. The alpha colony size, which is defined as the distance across similarly oriented alpha plates in a direction normal to the major plate axis, increases with alpha plate size. The microstructures are illustrated in Figs. 3.3-6 through 3.3-8.



Table 3.3-2
Volume Fraction and Discontinuity of Beta Phase
in Ti-6Al-4V Plate

Condition No.	Volume Fraction Beta Phase	Discontinuities of Beta Phase, Per cm ³
1	0.19	6.5×10^{12}
2	0.14	1.9×10^{11}
3	0.10	1.2×10^{11}

SC27903

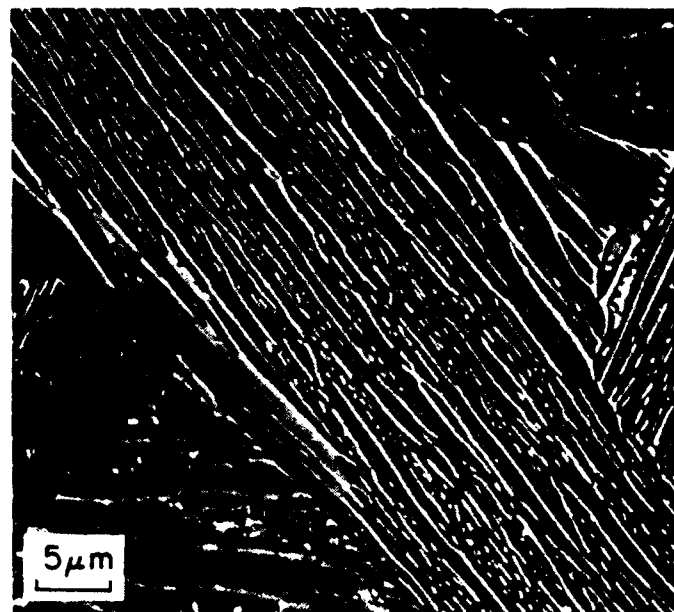


Fig. 3.3-3 SEM of Ti-6Al-4V plate given heat treatment No. 1. Beta phase is white.



SC27903

SC5358.4FR

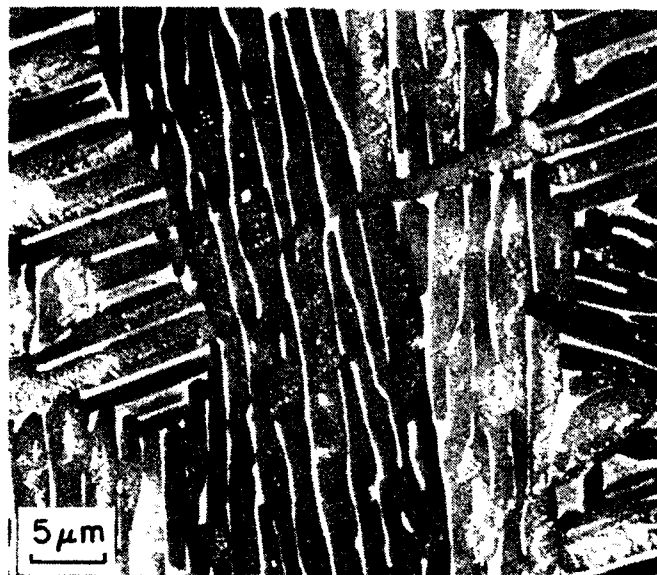


Fig. 3.3-4 SEM of Ti-6Al-4V plate given heat treatment No. 2. Beta phase is white.

SC27903

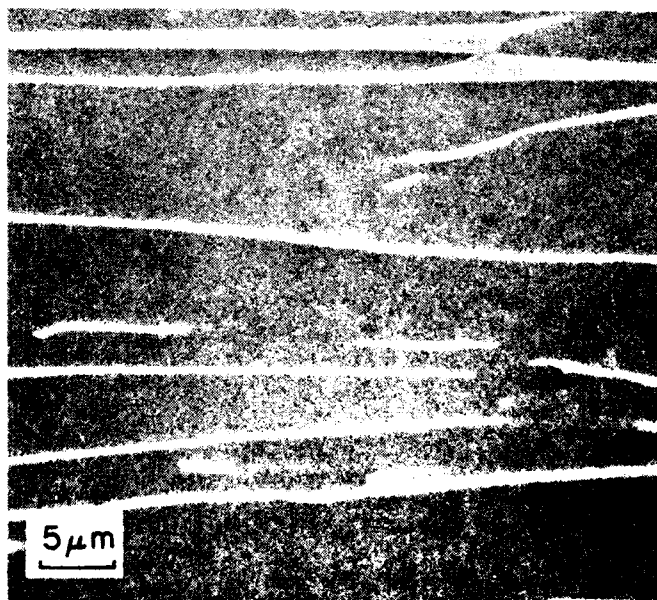


Fig. 3.3-5 SEM of Ti-6Al-4V plate given heat treatment No. 3. Beta phase is white.



SC5358.4FR

Table 3.3-3
Alpha Phase Dimensions in Ti-6Al-4V Plate

Condition No.	Average Length Alpha Phase Plates (μm)	Average Width Alpha Phase Plates (μm)	Alpha Phase Aspect Ratio	Colony Size (μm)
1 21	0.9	24:1	30	
2 32	1.8	17:1	58	
3 80	6.0	13:1	190	

SC27905

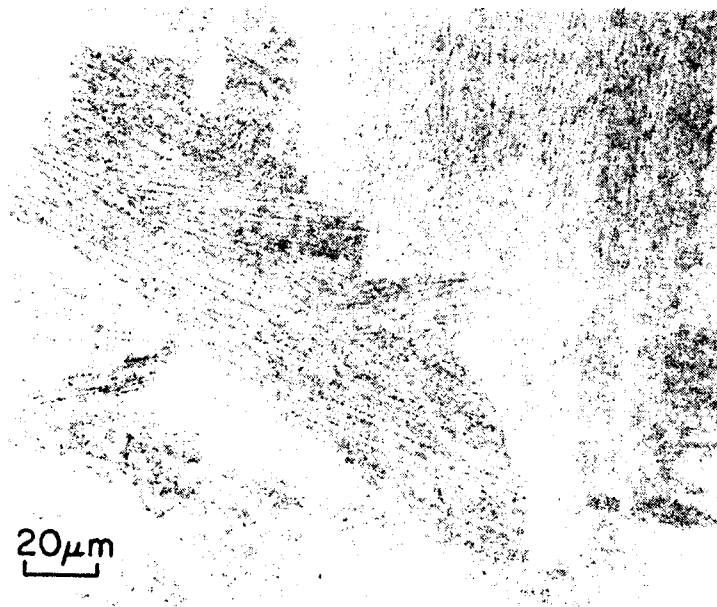


Fig. 3.3-6

LM of Ti-6Al-4V plate given heat treatment No. 2. Alpha phase is light, beta phase is dark.



SC5358.4FR

SC27905

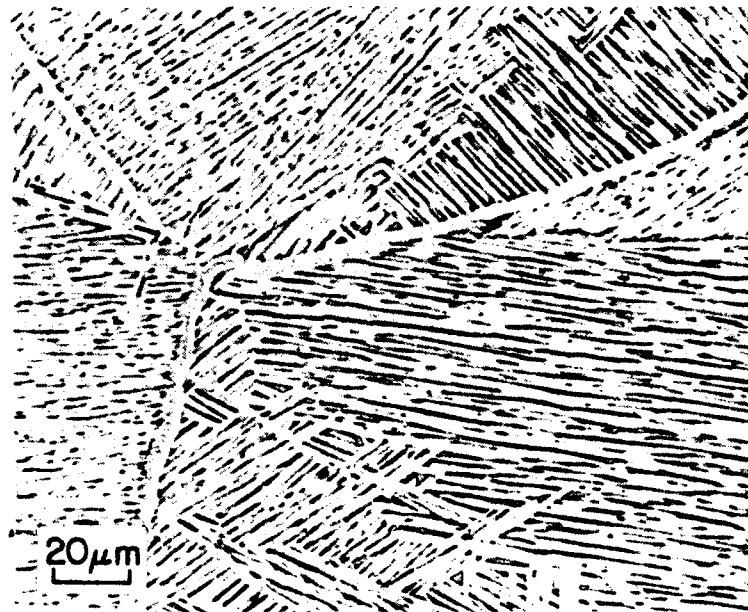


Fig. 3.3-7

LM of Ti-6Al-4V plate given heat treatment No. 2. Alpha phase is light, beta phase is dark.

SC27905

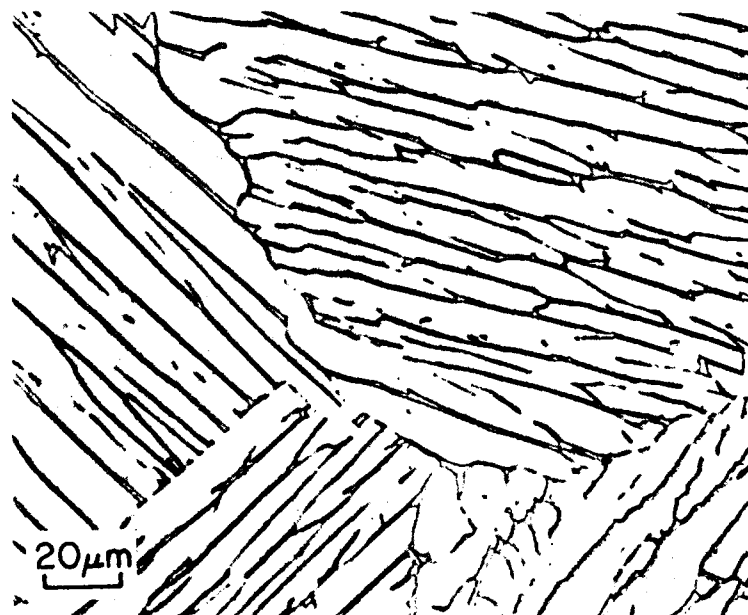


Fig. 3.3-8

LM of Ti-6Al-4V plate given heat treatment No. 3. Alpha phase is light, beta phase is dark.



The final microstructural parameters analyzed in this program are the compositions of the alpha and beta phases. The chemical analyses have been accomplished by means of thin-foil scanning/transmission electron microscopy using a quantitative x-ray energy dispersive spectroscopy technique developed previously.¹¹ The results, presented in Table 3.3-4, reveal the degree to which Al partitions to the alpha phase and V to the beta phase. The alpha phase data given in Table 3.3-4 are for the matrix alpha plates, and do not include the grain boundary alpha which would be expected to contain slightly higher Al and lower V contents.¹¹ Among the three treatments, the Al and V concentrations in alpha vary only slightly, whereas they vary significantly in the beta phase. These compositional variations are closely related to the volume fractions of the two phases, which vary only by about 10% for the alpha phase (from 0.81 to 0.90), but by 90% for the beta phase (from 0.10 to 0.19). Typical microstructures are illustrated in Figs. 3.3-9 through 3.3-11.

Table 3.3-4
Compositions of Alpha and Beta Phases in Ti-6Al-4V Plate

Condition No.	Alpha Phase		Beta Phase	
	Wt% Al	Wt% V	Wt% Al	Wt% V
1	7.2	1.8	3.5	15.8
2	7.7	1.7	2.1	17.3
3	7.3	1.5	1.7	23.2

3.3.2.3 Microstructural Characterization, Forging

The as-forged condition, Fig. 3.3-2, has a prior beta grain size of about 400 micrometers and nearly continuous grain boundary alpha. None of the heat treatments significantly alters the prior beta grain size or the grain boundary alpha. The forged material was given each of the three heat treatments listed in Table 3.3-1 and all microstructural features were measured. Because only three conditions could be tested in this program, two of the three heat treatments were selected to accompany the as-forged condition for test specimens. The selection of heat treatments No. 2 and No. 3 was based on achieving the widest possible variation in microstructures.



SC5358.4FR

SC40705



Fig. 3.3-9 TEM of Ti-6Al-4V plate given heat treatment No. 1.

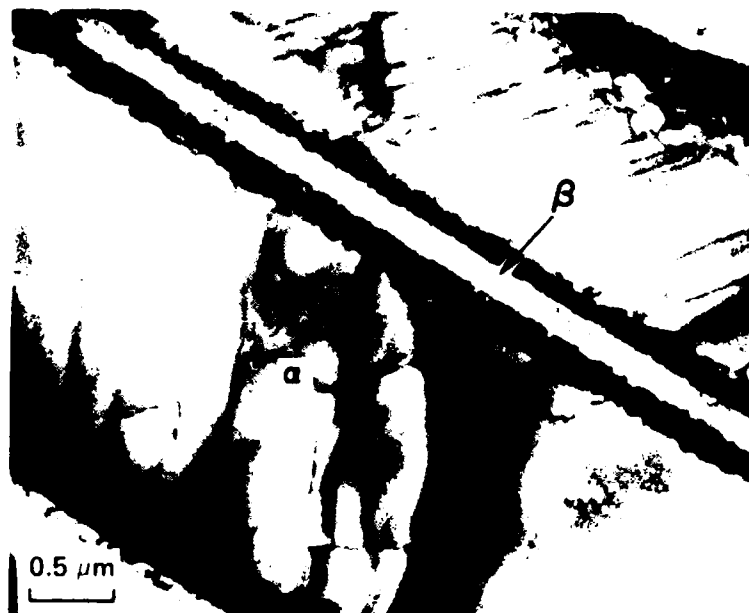


Fig. 3.3-10 TEM of Ti06Al-4V plate given heat treatment No. 2.



SC40705



Fig. 3.3-11 TEM of Ti-6Al-4V plate given heat treatment No. 3.

The volume fractions and dimensions of alpha and beta grains and continuity of beta phase were measured as a function of heat treatment. The volume fractions and continuity of beta phase are listed in Table 3.3-5. Similar to the plate material, heat treatment No.1 results in a greater volume fraction and more discontinuous beta phase than the other two treatments. However, the as-forged condition has a higher volume fraction and more discontinuous beta phase than any of the three post-forge heat treatment conditions. The heat treatments have succeeded in varying the volume fraction of beta phase by a factor of 1.5 and beta phase discontinuity by more than an order of magnitude.



Table 3.3-5
Volume Fraction and Discontinuity of Beta Phase
in Forged Ti-6Al-4V

Condition No.	Volume Fraction Beta Phase	Discontinuities of Beta Phase, per cm ³
as-forged	0.17	1.6×10^{12}
1	0.14	3.3×10^{11}
2	0.12	6.4×10^{10}
3	0.11	9.8×10^{10}

Alpha phase parameters are listed in Table 3.3-6. The microstructures are illustrated in Figs. 3.3-12 through 3.3-13. The average width of the alpha plates, which is probably the most significant of these dimensions, increases about four-fold from the as-forged condition through heat treatment No. 3. In contrast to the plate material, the alpha colony size does not vary in the same ratio that the alpha plate width varies.

Table 3.3-6
Alpha Phase Dimensions in Forged Ti-6Al-4V

Condition No.	Alpha Phase Plate Length (μm)	Alpha Phase Plate Width (μm)	Alpha Phase Aspect Ratio	Colony Size (μm)
as-forged	34	1.4	25:1	125
1	20	1.9	11:1	n.d.
2	92	4.9	19:1	124
3	43	5.5	8:1	189

n.d. - Not determined.



SC5358.4FR

SCA0708

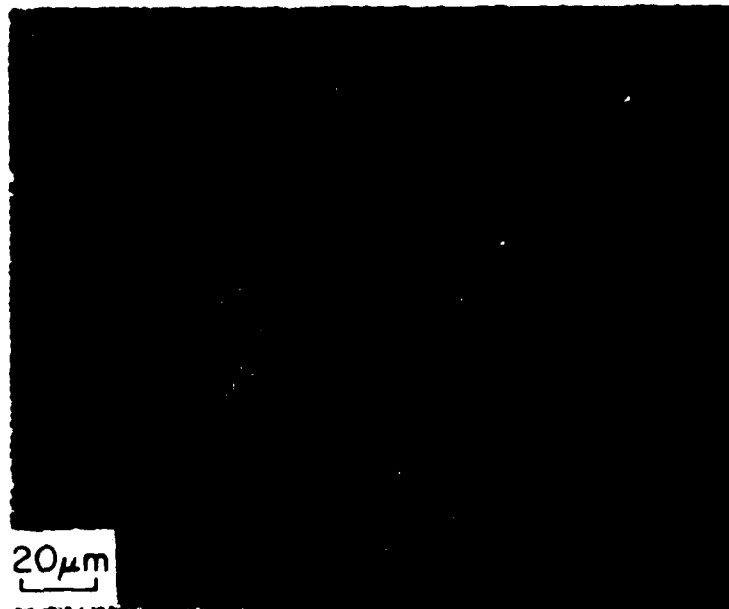


Fig. 3.3-12 LM of Ti-6Al-4V forging, as-forged.

SCA0708

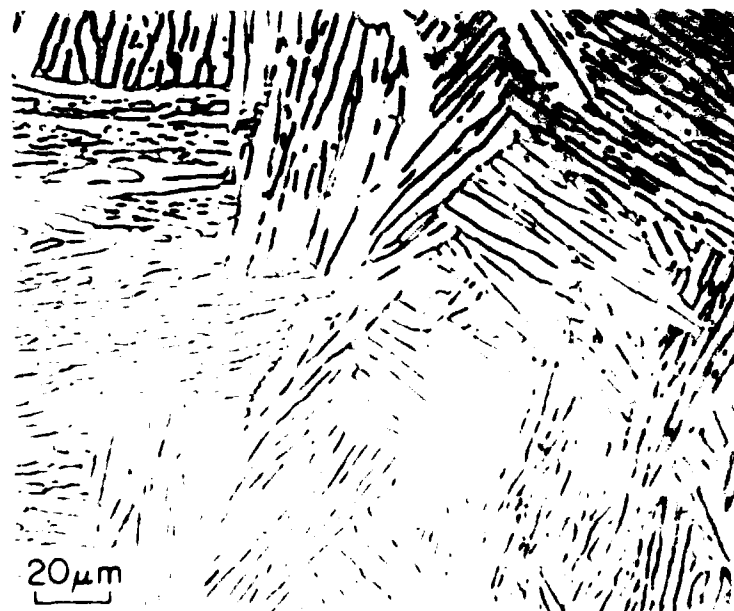


Fig. 3.3-13 LM of Ti-6Al-4V forging given heat treatment No. 2.



SC40706

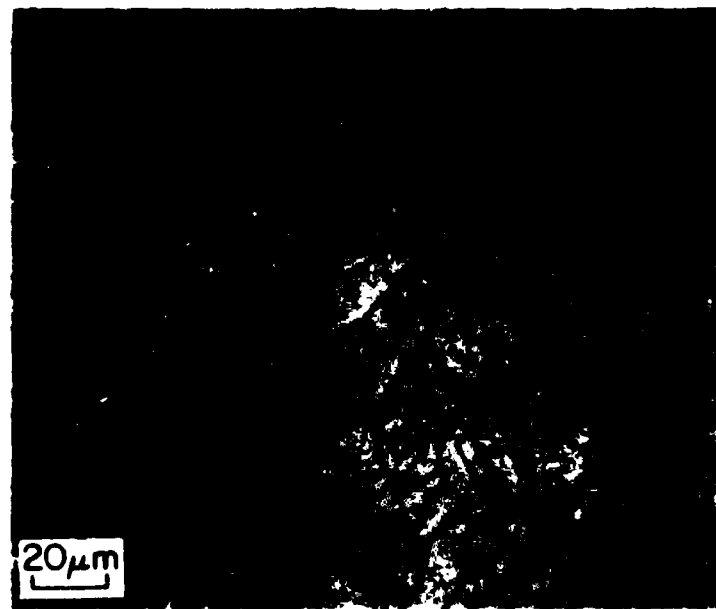


Fig. 3.3-14 LM of Ti-6Al-4V forging given heat treatment No. 3.

3.3.3 Tensile Properties

Room temperature tensile tests were conducted on samples from plate and from forged materials. The results from the plate material are presented in Table 3.3-7. It can be seen that the tensile properties vary with heat treatment, such that heat treatment No. 1 exhibits the highest strength and lowest ductility of the three conditions tested, while the material given heat treatment No. 3 is at the other extreme. The variations in microstructure, then, have influenced tensile properties, but not, as will be seen, in precisely the same way as fatigue crack propagation behavior was influenced.

The tensile data for the forged material are shown in Table 3.3-8. The as-forged condition has a higher strength than was seen for Condition No. 1 of the plate material. The tensile strengths of Conditions No. 2 and No. 3 are reduced from the as-forged condition, but are stronger than their plate material counterparts. The elongations of the forged material are generally larger than those observed for the plate material, but the reductions in area are smaller for the forged material.



Table 3.3-7
Tensile Properties of Plate Material

Condition No.	Yield Stress (MPa)	Ultimate Tensile Strength (MPa)	Elongation (%)	Reduction in Area (%)
1	805	867	7.7	20
	773	843	8.3	22
2	737	815	9.7	25
	764	836	9.3	25
3	704	773	10.7	29
	701	771	10.3	29

Table 3.3-8
Tensile Properties of Forged Material

Condition No.	Yield Stress (MPa)	Ultimate Tensile Strength (MPa)	Elongation (%)	Reduction in Area (%)
1	820	913	8.9	16.6
	816	905	9.7	21.7
2	787	857	9.2	19.7
	787	878	14.4	20.4
3	763	847	14.1	25.6
	768	842	12.2	27.9

3.3.4 Fatigue Crack Propagation and Crack Path Analysis

3.3.4.1 Plate Material, R = 0.1

Fatigue crack propagation results for the three microstructural conditions tested at an R ratio (minimum load/maximum load) of 0.1 are shown in Figs. 3.3-15 through 3.3-17. In all three plots, the data obtained by load shedding (K-decreasing) are represented by the filled symbols. The crack growth rates for the load shedding portion of the tests are slightly faster than the growth rates for the K-increasing (open symbols)

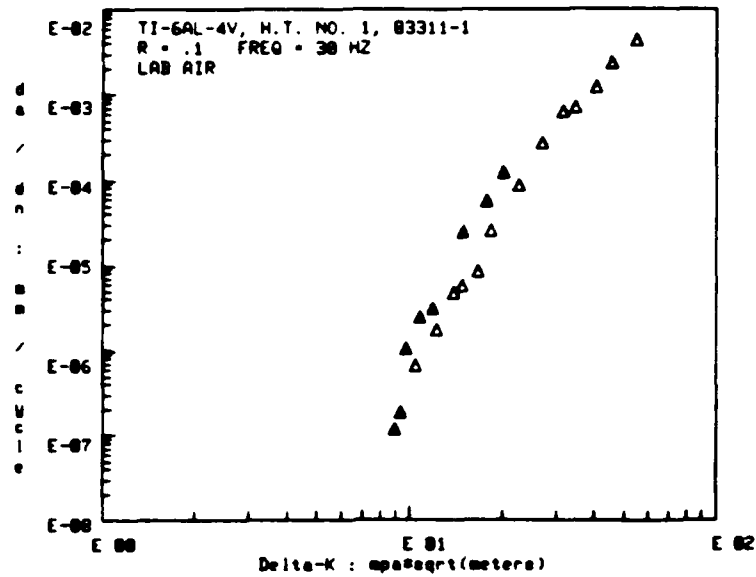


Fig. 3.3-15 da/dN vs ΔK for plate material, heat treatment No. 1, $R = 0.1$.

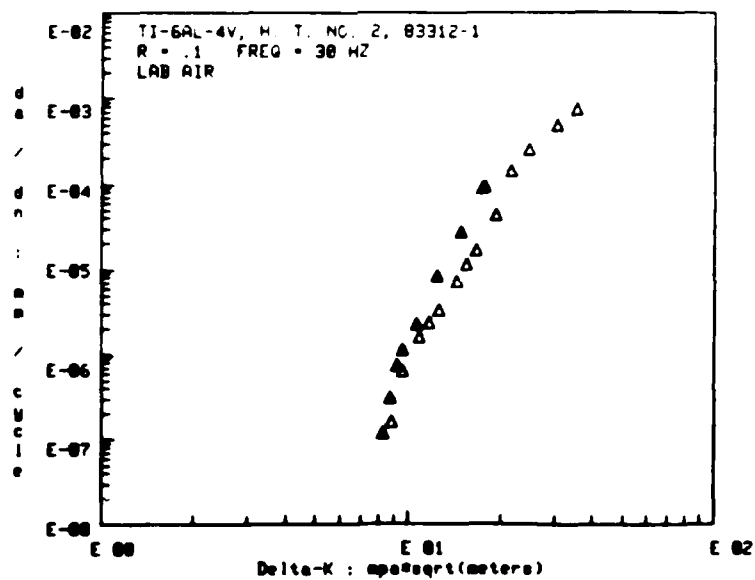


Fig. 3.3-16 da/dN vs ΔK for plate material, heat treatment No. 2, $R = 0.1$.

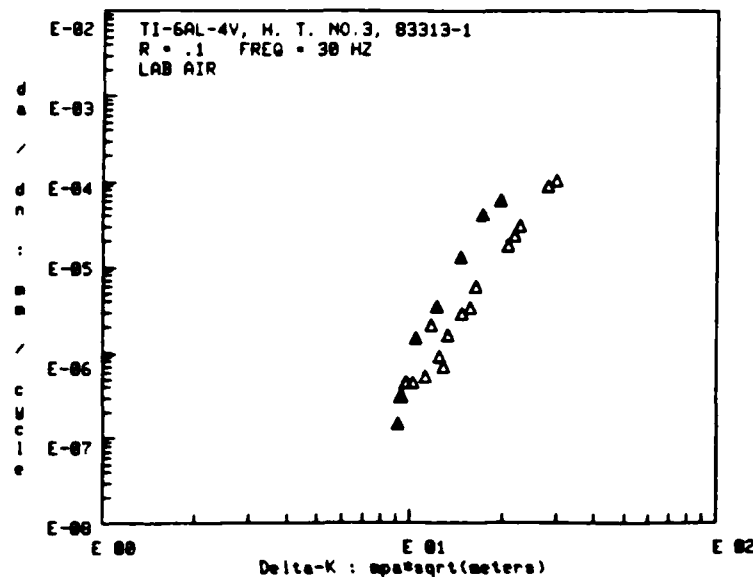


Fig. 3.3-17 da/dN vs ΔK for plate material, heat treatment No. 3, $R = 0.1$.

portion of the tests. This behavior has been reported for other alloy systems,¹² where the K-decreasing data are seen to be on the high side of the data set. Microstructure, which is the focus of this study, cannot be the source of the load-shed/load-increment phenomenon.

A special test was conducted to determine if crack length was the primary contributor to the load-shed/load-increment effect. A specimen given heat treat No. 1 was first load shed to propagate the crack under a K-decreasing condition, then load increased (or held constant) for K-increasing, reversed to K-decreasing, and once again reversed to a K-increasing condition. The results are plotted in Fig. 3.3-18, where it can be seen that the phenomenon is not due simply to crack length. For instance, the second K-decreasing region moves immediately upon decreasing the load to an increased crack growth rate. The growth rate falls, however, to a value lower than that observed for the initial load-shedding regime while staying greater than the initial load-increment portion of the test. A plot of crack growth rate as a function of crack length for three ΔK values demonstrates the lack of a significant effect of crack length on da/dN , Fig. 3.3-19.



SC5358.4FR

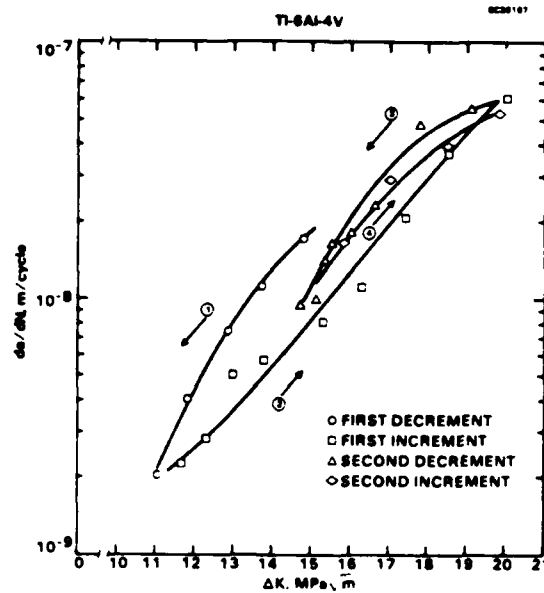


Fig. 3.3-18 da/dN vs ΔK special test of plate material, heat treatment No. 1, $R = 0.1$.

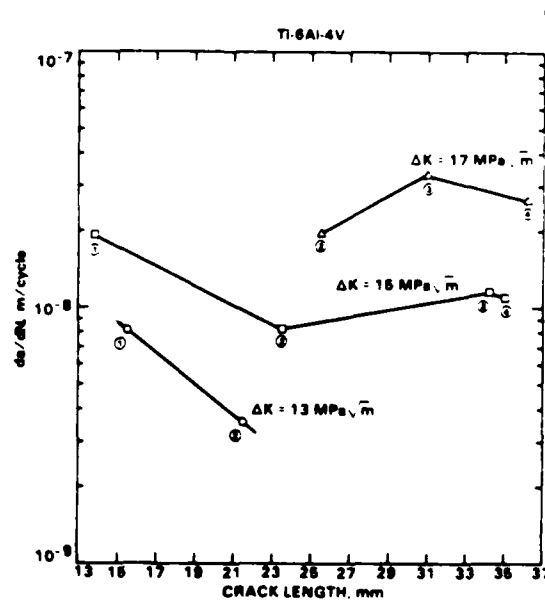


Fig. 3.3-19 da/dN vs crack length, special test of plate material, $R = 0.1$.



The K-decreasing/K-increasing phenomenon, however, can be explained in terms of crack path tortuosity and secondary cracking. Lineal roughness, which is an excellent parameter for the quantification of crack path tortuosity, was measured along the crack lengths of the specimens whose test results are shown in Figs. 3.3-15 through 3.3-17. The lineal roughness values, Figs. 3.3-20 through 3.3-22, clearly show that the cracks are more divergent during the K-increasing portions of the tests than during the K-decreasing regimes. The apparent crack growth rates, i.e., the rate measured on the test specimens, are therefore faster during load-shedding because the cracks are propagating over shorter distances.

Secondary cracking also contributes to the difference in growth rate between the K-decreasing and K-increasing portions of the tests. For instance, the ratio of branched (secondary) crack length to the main crack length is plotted against ΔK for the three tests in Figs. 3.3-23 through 3.3-25. By normalizing the secondary crack lengths to the actual length of the main crack, the contribution of the secondary cracks to the apparent crack growth rate can be evaluated. The figures demonstrate the increase in secondary cracking during the K-increasing test regime over the K-decreasing portion of the tests.

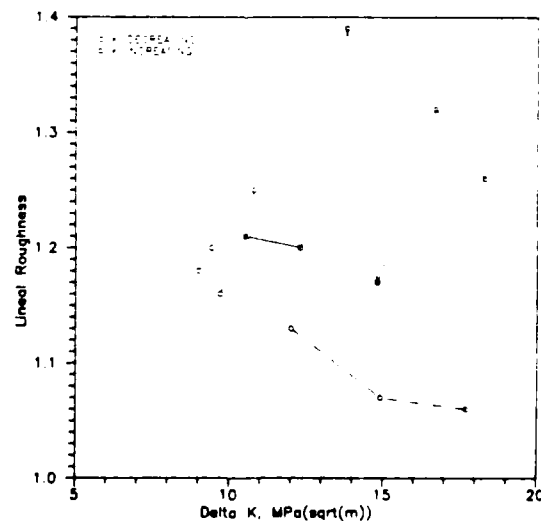


Fig. 3.3-20 Lineal roughness vs ΔK for plate material, heat treatment No. 1, including load shed and load increment segments, $R = 0.1$.

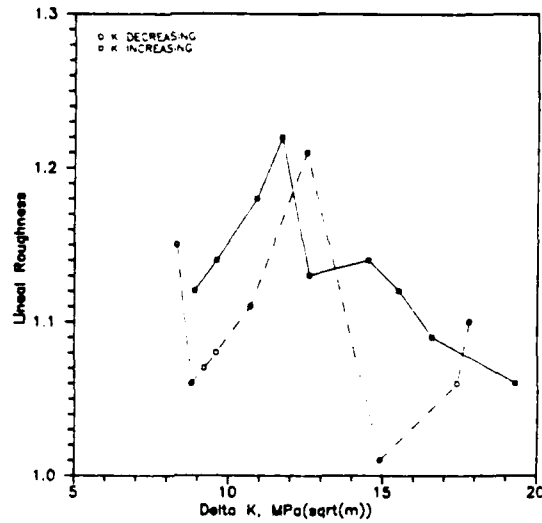


Fig. 3.3-21 Lineal roughness vs ΔK for plate material, heat treatment No. 2, including load shed and load increment segments, $R = 0.1$.

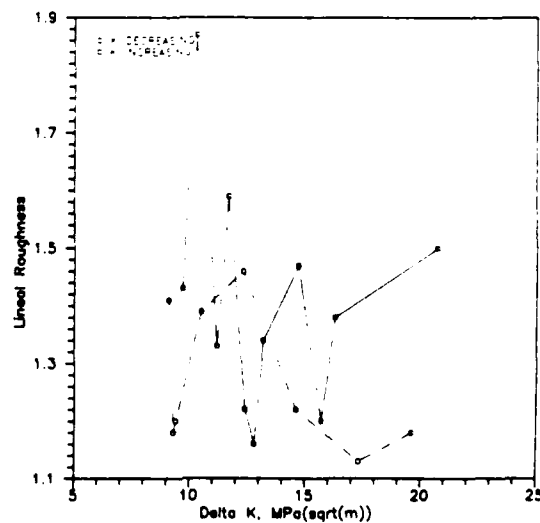


Fig. 3.3-22 Lineal roughness vs ΔK for plate materials, heat treatment No. 3, including load shed and load increment segments, $R = 0.1$.



SC5358.4FR

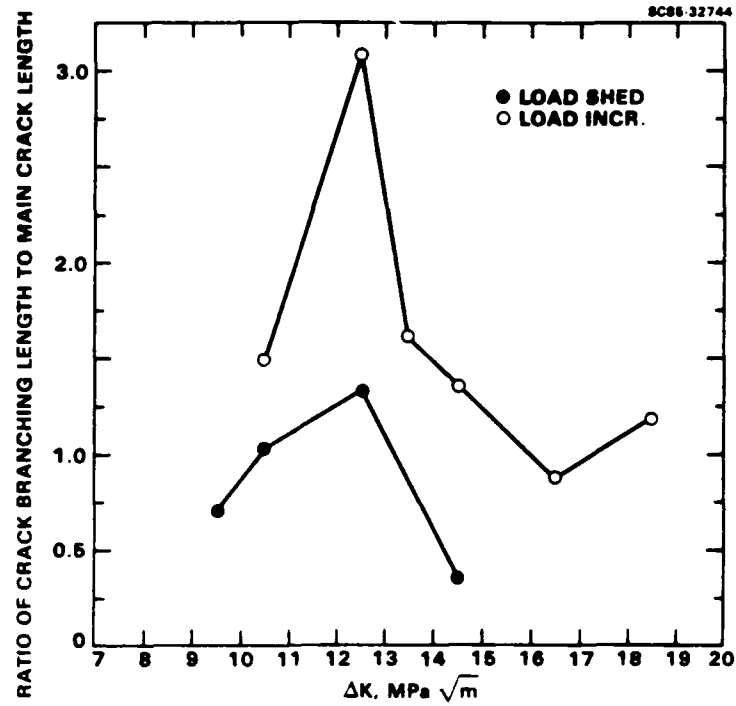


Fig. 3.3-23 Secondary cracking vs ΔK for plate material, heat treatment No. 1, including load shed and load increment segments, $R = 0.1$.

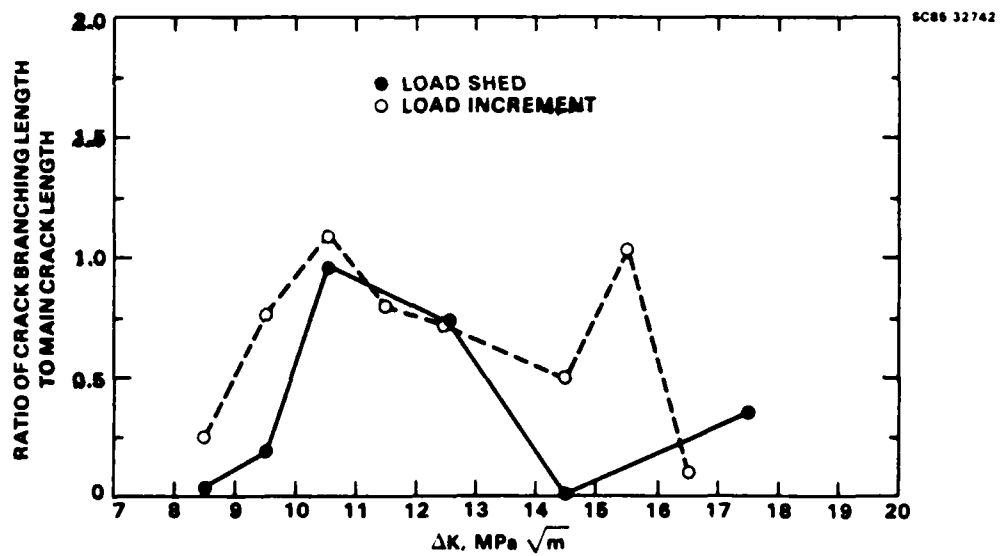


Fig. 3.3-24 Secondary cracking vs ΔK for plate material, heat treatment No. 2, including load shed and load increment segments, $R = 0.1$.



SC5358.4FR

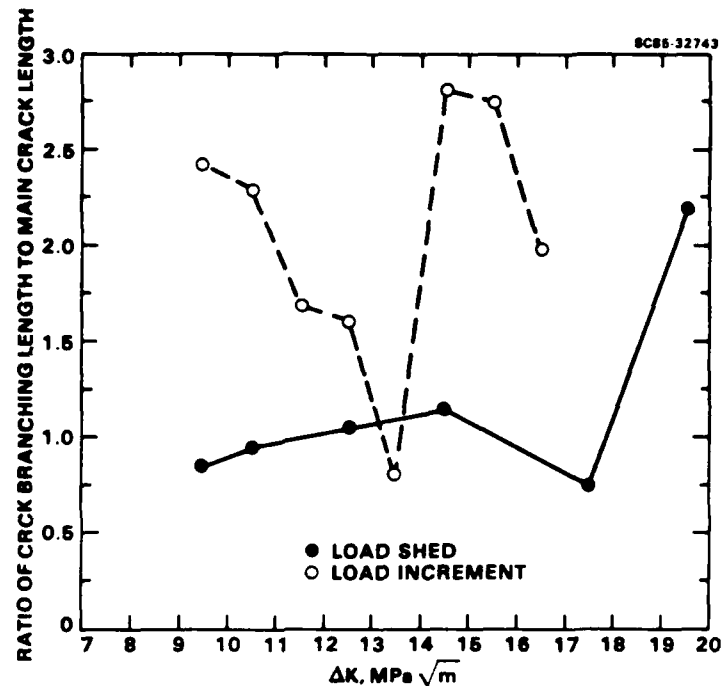


Fig. 3.3-25 Secondary cracking vs ΔK for plate material, heat treatment No. 3, including load shed and load increment segments, $R = 0.1$.

The total contribution of crack path tortuosity and crack branching can be assessed by plotting the da/dn vs ΔK data using the microscopic crack extension per cycle rather than the macroscopic extension measured during testing. The microscopic crack extension is the sum of the actual main crack length and the secondary crack length for each ΔK increment. An example of the result obtained when using this approach is given in Fig. 3.3-26. The data points for the K-decreasing and K-increasing portions of the test are seen to converge to a single curve.

Comparisons among the three heat treat conditions are most meaningful when made using only K-decreasing or K-increasing regions. The latter case is presented in Fig. 3.3-27, where it can be seen that, although the growth rates are not widely varying, Condition No. 3 exhibits a consistently slower growth rate than conditions No. 1 or No. 2. Furthermore, Condition No. 2 has the fastest growth rate of the three conditions tested.



SC5358.4FR

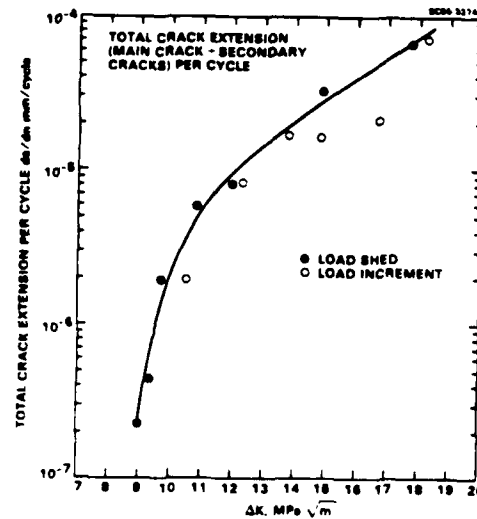


Fig. 3.3-26 Total da/dN (see text) vs ΔK for plate material, heat treatment No. 1, including load shed and load increment segments, $R = 0.1$.

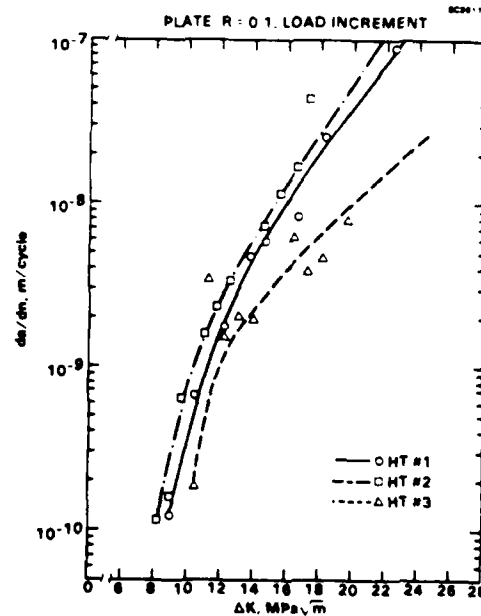


Fig. 3.3-27 da/dN vs ΔK for plate material, heat treatment Nos. 1, 2 and 3. Load increment data only, $R = 0.1$.



Correlations of individual, quantified microstructural features with crack growth rates require that all features other than that being analyzed be held constant. Such is not the case with the data of Fig. 3.3-27. The influence of individual microstructural features on crack growth rate will be presented later, in conjunction with the data from the forged material.

Detailed examination of crack paths reveals that the cracks tend to move through the microstructures in a similar manner in the three test specimens. The cracks generally change direction when passing from one colony to the next so as to maintain a fairly large angle with the alpha plates about 70% of the crack lengths make an angle of 45° or larger with the alpha plates, Fig. 3.3-28. Grain boundary alpha appears to have no influence on the cracks, since the cracks frequently cross these features without a change of direction.

SC40707



Fig. 3.3-28 SEM of crack moving across alpha colony boundary maintaining high angle with alpha plates.



Lineal roughness values for the three microstructural conditions are shown in Fig. 3.3-29. Condition No. 2, which has the fastest crack growth rate, has the least amount of lineal roughness. That is, this is the smoothest fracture surface of the three. Condition No. 3, the slowest of the three, shows the roughest fracture surface, while Condition No. 1 is intermediate to the others. This represents a direct correlation between crack growth rate and lineal roughness.

The degree of crack branching, or secondary cracking, is given in Fig. 3.3-30, where the secondary crack length is again normalized to the main crack actual length. Condition No. 2 is seen to exhibit the least amount of secondary cracking, just as it has the least amount of main crack tortuosity. Conditions No. 1 and No. 3, on the other hand, contain secondary cracking to a much larger extent than Condition No. 2. Crack path tortuosity and secondary cracking, with their attendant roughness induced closure, then, can account for the differences in crack growth rates observed for the three different microstructural conditions.

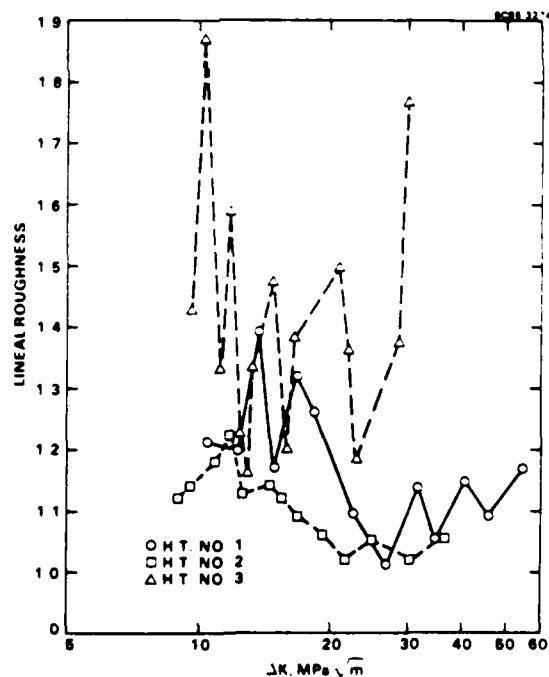


Fig.3.3-29 Lineal roughness vs ΔK for plate material, heat treatments No. 1, 2 and 3. Load increment data only $R = 0.1$.



SC5358.4FR

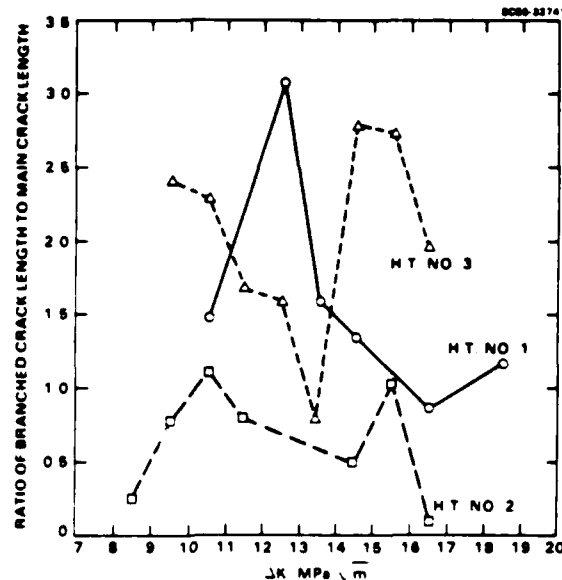


Fig. 3.3-30 Ratio of crack branching to main crack vs ΔK for plate material, heat treatments No. 1, 2 and 3, $R = 0.1$.

3.3.4.2 Forged Material, $R = 0.1$

Fatigue crack propagation rates for the three conditions of forged Ti-6Al-4V tested at an R ratio of 0.1 are presented in Figs. 3.3-31 through 3.3-33. The data obtained during the K -decreasing portion of the tests are shown as filled symbols, while the open symbols represent the measurements taken for increasing K . Similar to the plate material, the cracks have propagated at a faster rate during the K -decreasing segments of the tests. However, for the forged material, the differences in growth rates between the K -decreasing and the K -increasing portions of the tests are considerably less than those observed for the plate material, cf. Figs. 3.3-15 through 3.3-17 and 3.3-31 through 3.3-33.

Inspection of Figs. 3.3-31 through 3.3-33 reveals that microstructural Condition No. 2 exhibits the largest difference between K -decreasing and K -increasing crack growth rates. Lineal roughness measurements, Figs. 3.3-34 through 3.3-36 show that Condition No. 2 has a significant increase in crack path tortuosity during the



SC5358.4FR

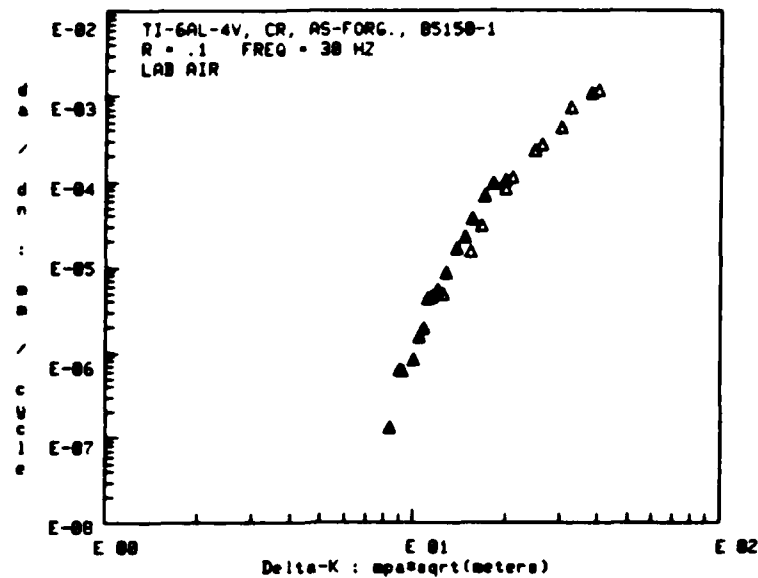


Fig. 3.3-31 da/dN vs ΔK , forged material, as forged, $R = 0.1$.

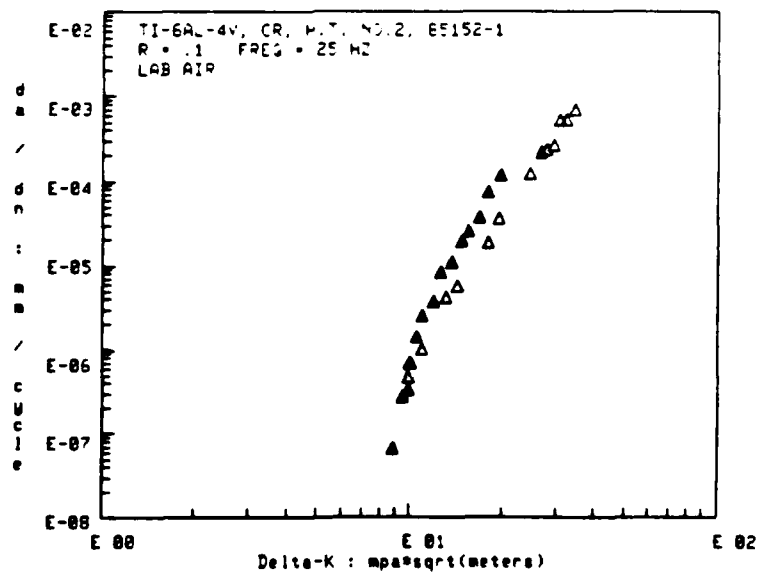


Fig. 3.3-32 da/dN vs ΔK , forged material, heat treatment No. 2, $R = 0.1$.

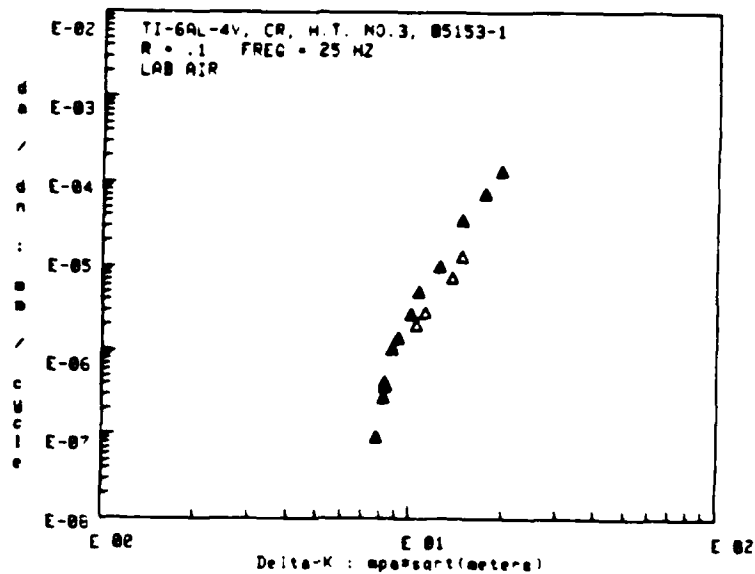


Fig. 3.3-33 da/dN vs ΔK , forged material, heat treatment No. 3, $R = 0.1$.

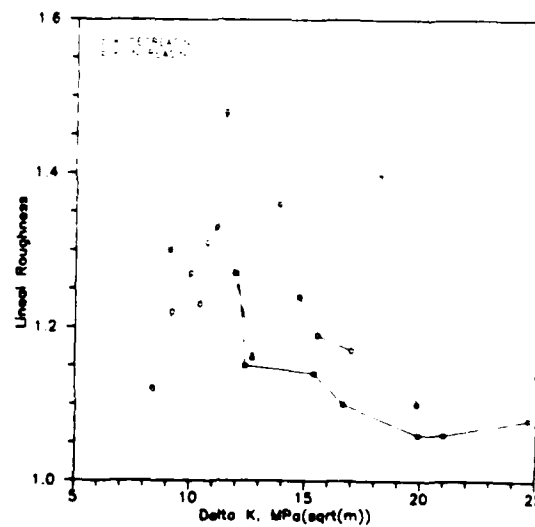


Fig. 3.3-34 Lineal roughness vs ΔK , forged material, as-forged, including load shed and load increment segments, $R = 0.1$



SC5358.4FR

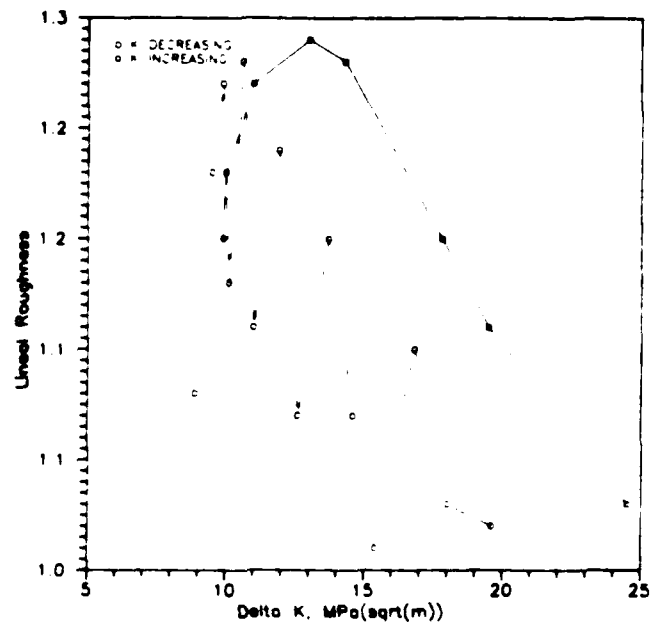


Fig. 3.3-35 Lineal roughness vs ΔK , forged material, heat treatment No. 2, including load shed and load increment segments, $R = 0.1$.

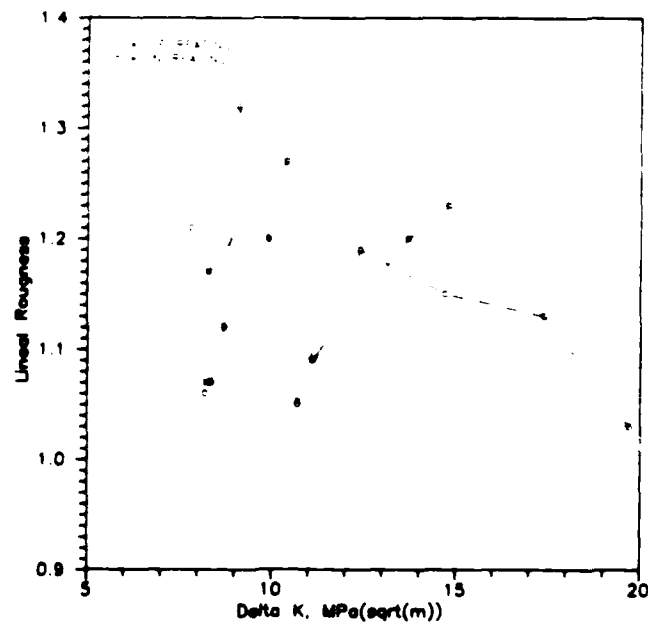


Fig. 3.3-36 Lineal roughness vs ΔK , forged materials, heat treatment No. 3, including load shed and load increment segments, $R = 0.1$.



K-increasing portion of the fatigue test over the K-decreasing segment. Condition No. 3 has about equal amounts of crack path tortuosity during the two test segments, while Condition No. 1 appears to have slightly greater tortuosity during the K-decreasing portion of the test. Crack branching measurements, Figs. 3.3-37 through 3.3-39 demonstrate that Condition No. 2 has the greatest increase in the amount of secondary cracking during the K-increasing test segment compared to the K-decreasing portion. The as-forged microstructure appears to have only slightly more secondary cracking during the K-increasing test regime, whereas Condition No. 3 appears to have slightly more secondary cracking during the K-decreasing segment of the test. This behavior is consistent with the observations made for the plate material that crack path tortuosity and secondary cracking can account for the differences in crack growth rates between the K-decreasing and K-increasing segments of the tests.

A comparison of crack growth rate among the three heat treated conditions for the K-increasing regime is presented in Fig. 3.3-40. In contrast to the plate material, Condition No. 2 exhibits the slowest crack growth rate, with Conditions No. 1 and No. 3

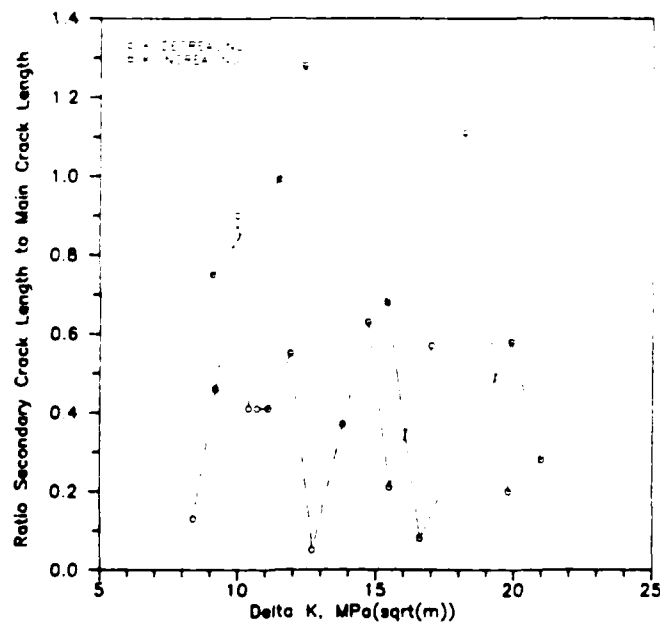


Fig. 3.3-37 Secondary cracking vs ΔK , forged materials, as-forged, including load shed and load increment segments, $R = 0.1$



SC5358.4FR

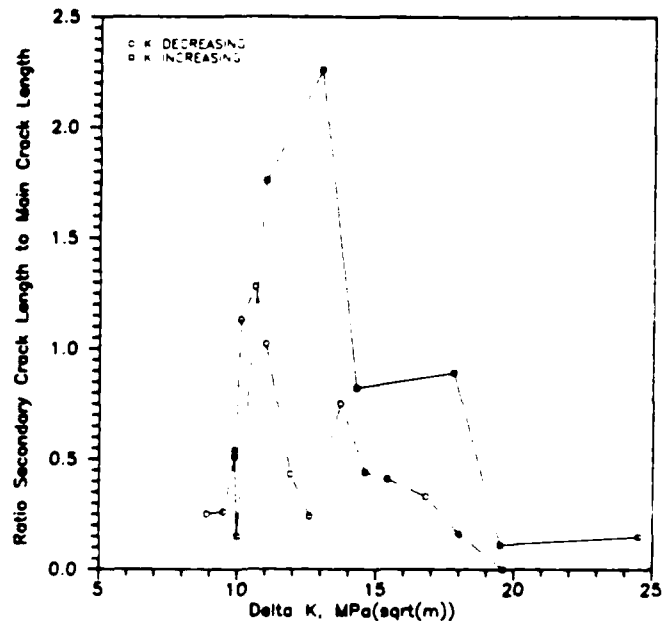


Fig. 3.3-38 Secondary cracking vs ΔK , forged material, as-forged, heat treatment No. 2, including load shed and load increment segments, $R = 0.1$.

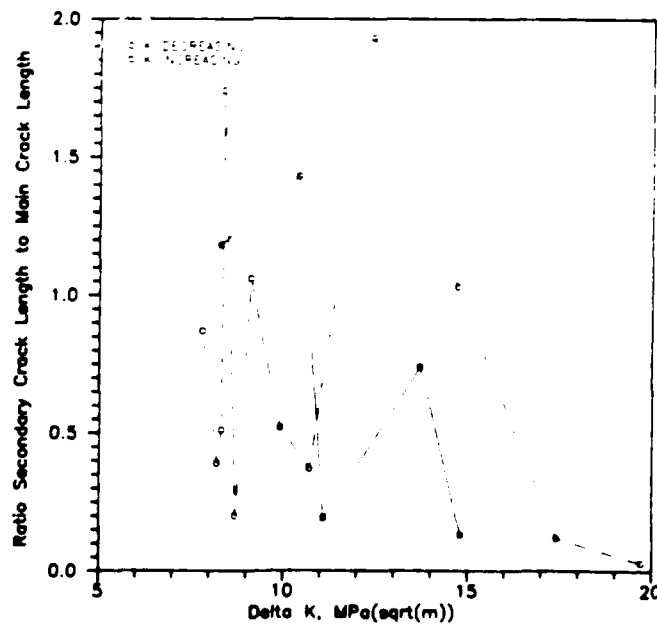


Fig. 3.3-39 Secondary cracking vs ΔK , forged material, as-forged, heat treatment No. 3, including load shed and load increment segments, $R = 0.1$.

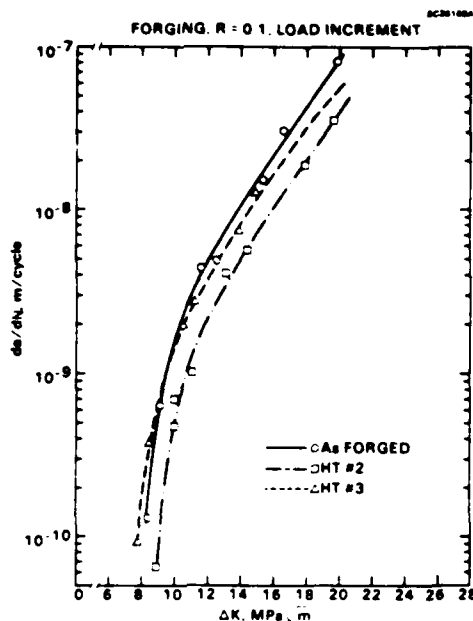


Fig. 3.3-40 da/dN vs ΔK , forged material, heat treatments No. 1, 2 and 3, load increment data only, $R = 0.1$.

having nearly identical growth rates. Comparison of the crack growth behavior with the plate material, cf. Figs. 3.3-40 and 3.3-27 demonstrates that cracks propagate at a faster rate in the forging than in the plate. For instance, the growth rate in Condition No. 2 of the forged material is about equivalent to the growth rate of Condition No. 1 of the plate material.

As was the case with the plate material, correlations of individual microstructural features has not been attempted for the data of Fig. 3.3-40. The correlation of microstructure with crack growth rate will be performed in the following section, where plate and forged material results are combined.

Crack path analyses demonstrate that the cracks move through the microstructures of the forging in a manner similar to the cracks in the plate material. That is, the cracks change direction as they pass from one colony to the next so as to maintain a fairly large angle with the individual alpha plates. As was observed in the plate material, grain boundary alpha appears to have little influence on the crack propagation direction.



Comparisons of crack path tortuosity and secondary cracking among the three microstructural conditions for the K-increasing test condition are given in Figs. 3.3-41 and 3.3-42. Condition No. 2 has significantly more secondary cracking than either the as-forged or heat treat No. 1 conditions, and only slightly less crack path tortuosity than the as-forged condition. These two parameters, then, can account for the differences in crack growth rates measured in the three different microstructural conditions.

3.3.4.3 Combined Results from Plate and Forged Materials, $R = 0.1$

Inspection of the quantified microstructural data of Tables 3.3-2 through 3.3-6 reveals no significant correlation of individual features with crack growth rate data shown in Figs. 3.3-27 and 3.3-40. The lack of correlation of individual microstructural features with da/dn indicates that the total effect of microstructure is a combination of the individual parameters. One approach to quantifying the synergistic effects of individual microstructural parameters is to perform regression analysis of the data. This reduces the correlation of microstructure and fatigue crack growth rate to a mathematical form and provides a weighting factor to the contribution of the various microstructural features. For the regression analyses to be meaningful, we must have identified all

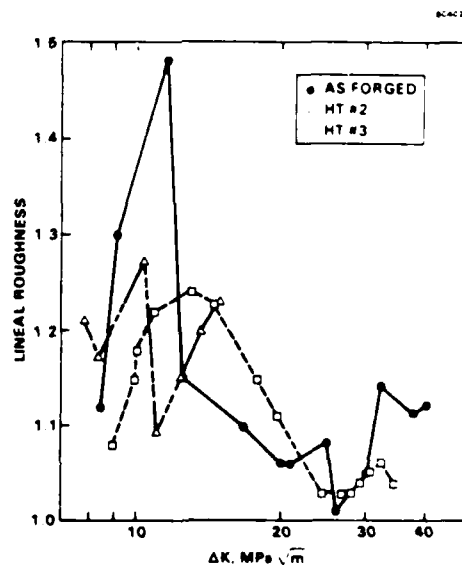


Fig. 3.3-41 Lineal roughness vs ΔK , forged material, heat treatments No. 1, 2 and 3, load increment data only, $R = 0.1$.

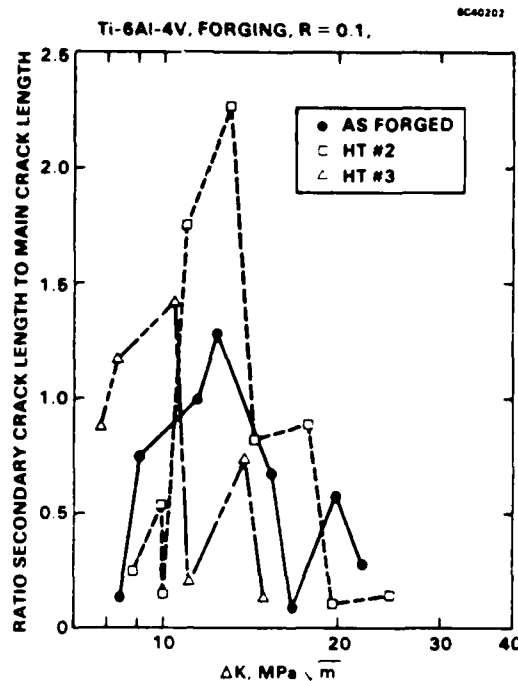


Fig. 3.3-42 Secondary cracking vs ΔK , forged material, heat treatments No. 1, 2 and 3, load increment data only, R = 0.1.

parameters that make significant contributions to the fatigue crack propagation resistance. It is well-known that da/dn is a function of the tensile strength of the alloy, and it was shown earlier that the degree of secondary cracking will influence crack growth rate. These parameters, however, are not included in the regression analysis because they, too, are a function of the microstructure. That is, an analysis of the microstructural contribution to da/dn will inherently include the microstructural effects on tensile properties and the propensity for secondary cracking, as well as crack path tortuosity. Oxygen level is also known to influence tensile properties of titanium alloys. For the present case, however, the oxygen levels are nearly the same, Table 3.2-1, and oxygen will not be a factor. The resulting analysis, then, will apply to beta processed Ti-6Al-4V having an oxygen level around 1200-1300 ppm. Carbon is known to have only a slight effect on tensile strength¹³ over the range included in the two heats tested, and, therefore, has not been included in the analysis. Compositions of alpha and beta phases



were introduced as microstructural variables, Table 3.3-4, that may influence properties. However, only the beta phase exhibits a significant variation in composition and, for the case of these equilibrium structures, a measure of volume fraction of beta phase will essentially duplicate the measure of composition. Composition of alpha and beta phases has therefore not been included in the analysis.

Multiple linear regression analysis was performed using the microstructural features quantified individually in Tables 3.3-2, 3.3-3, 3.3-5 and 3.3-6. The expression that comes from the analysis is

$$\ln da/dn = -11.10 + 38.57X1 - 0.33X2 + 0.15X3 + 0.0016X4 + 0.35X5 \quad (1)$$

where $X1$ = volume fraction beta phase,
 $X2$ = number of beta phase discontinuities $\times 10^{12} \text{ cm}^{-3}$,
 $X3$ = alpha phase plate width in micrometers,
 $X4$ = alpha colony size in micrometers,
 $X5$ = ΔK in $\text{MPa}\sqrt{\text{m}}$,

and da/dn is in meters per cycle, $\times 10^{-8}$. Figure 3.3-43 demonstrates the ability of Eq. (1) to predict fatigue crack growth rate in beta processed Ti-6Al-4V, where measured values are plotted against calculated values, with the straight line being a one-to-one correlation. The data points in Fig. 3.3-43 are from curves in Figs. 3.3-27 and 3.3-40 at stress intensity levels from 12-20 $\text{MPa}\sqrt{\text{m}}$. It can be seen that the Equation gives values that are well within a factor of two from the measured values.

Examination of the weighting factors in Eq. (1) reveals the manner in which each of the microstructural features influences crack growth rate. For instance, it can be seen that increasing the volume fraction of beta phase, the continuity of the beta phase, the width of alpha plates, the size of alpha colonies, or the stress intensity level increases the crack growth rate. The rates at which each of these features affects da/dn are shown in Figs. 3.3-44 through 3.3-47; the constant values used for the calculations were as follows: volume fraction beta = 0.1, beta phase discontinuities = $0.12 \times 10^{12} \text{ cm}^{-3}$, alpha plate width = 6 mm, and alpha colony size = 190 mm. Varying



SC5358.4FR

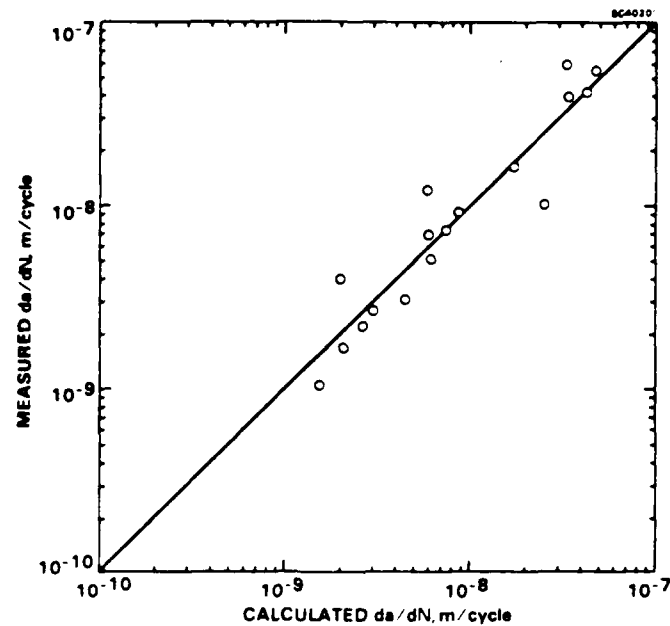


Fig. 3.3-43 Measured da/dN vs calculated da/dN at $R = 0.1$ for plate and forged materials using Eq. (1)

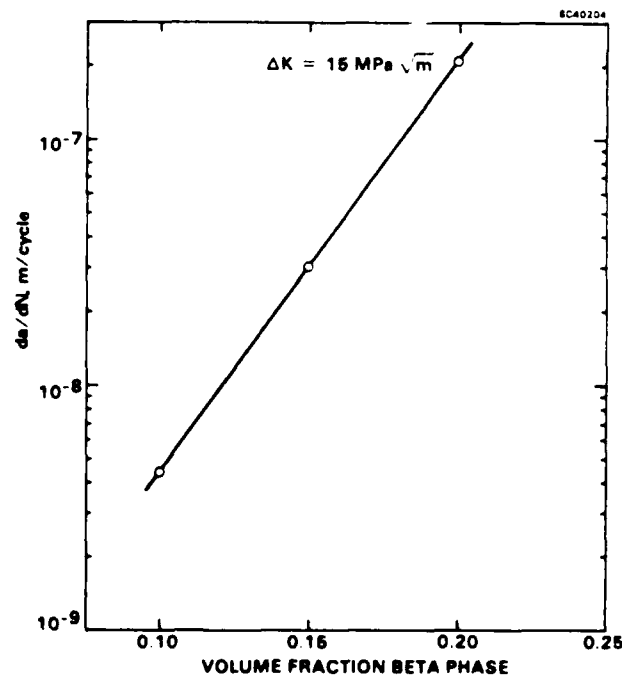


Fig. 3.3-44 da/dN vs volume fraction beta phase at $R = 0.1$, using Eq. (1).

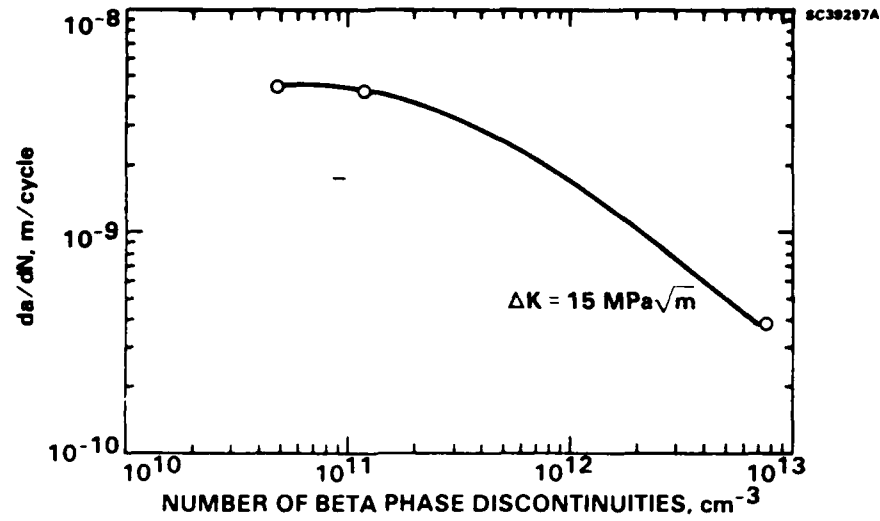


Fig.3.3-45 da/dN vs beta phase discontinuities at $R = 0.1$, using Eq. (1).

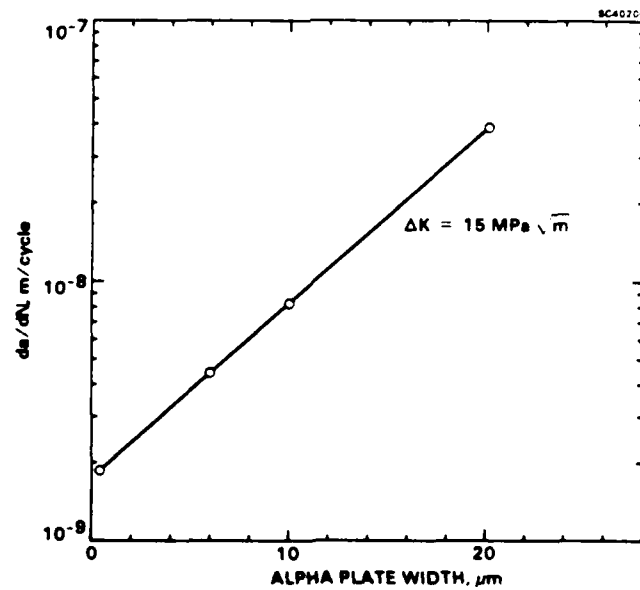


Fig. 3.3-46 da/dN vs alpha plate width at $R = 0.1$, using Eq. (1).

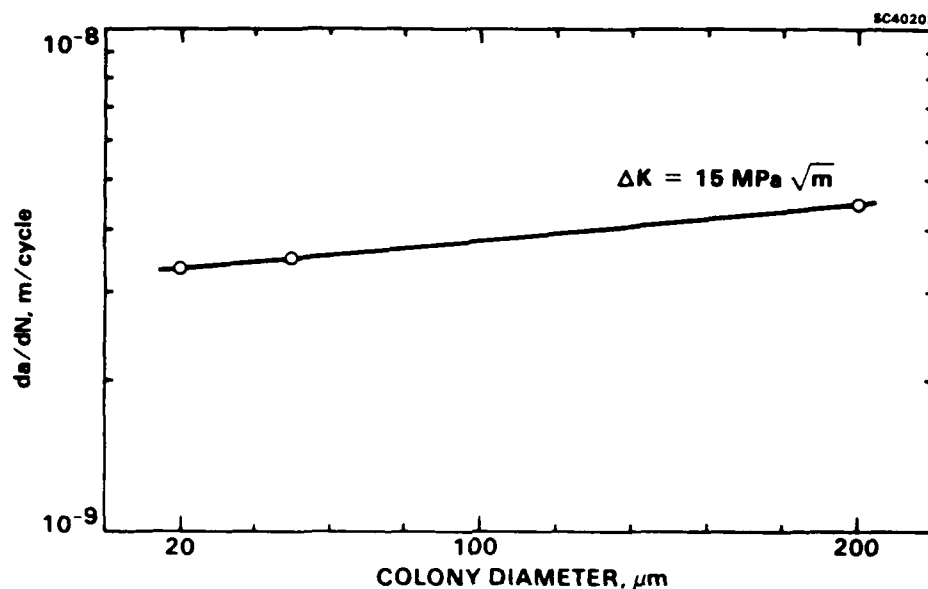


Fig. 3.3-47 da/dN vs alpha colony size at $R = 0.1$, using Eq. (1).

the volume fraction of beta phase from 0.1 to 0.2, which is about the limit for beta treated Ti-6Al-4V, increases the fatigue crack growth rate by two orders of magnitude, Fig. 3.3-44. In the same vein, Fig. 3.3-45 shows that increasing the number of beta phase discontinuities, i.e., decreasing the continuity of the beta phase, from 5×10^{10} to $7.5 \times 10^{12} \text{ cm}^{-3}$ results in an order of magnitude reduction in crack growth rate. These two results support the conclusion that the crack growth resistance of beta processed Ti-6Al-4V can be improved by reducing the volume fraction of beta phase in the microstructure.

Continuing the examination of the effect of individual microstructural features on crack growth rate, Fig. 3.3-46 reveals that da/dN can be reduced by decreasing the width of the alpha plates. A variation in width of alpha plates from 0.5-20 micrometers, a reasonable range of sizes for beta processed 6-4, increases the crack growth rate by about an order of magnitude. Finally, the influence of alpha colony size on da/dN is shown in Fig. 3.3-47. Surprisingly, there is little effect on crack growth rate of increasing the colony size from 20-200 micrometers.



3.3.4.4 Plate Material, $R = 0.7$

Fatigue crack propagation rates for the three conditions tested at an R ratio of 0.7 are presented in Fig. 3.3-48. In contrast to the $R = 0.1$ data, samples tested at $R = 0.7$ exhibit no differences in growth rate between K -decreasing and K -increasing test regimes.

Inspection of Figure 3.3-48 reveals that Condition No. 3 has a consistently slower growth rate than Conditions No. 1 or No. 2, both of which have approximately the same growth rate. The effect of heat treatment on fatigue crack growth rate, then, is similar for tests conducted at R ratios of 0.1 and 0.7, cf. Figs. 3.3-27 and 3.3-48. Detailed crack path measurements indicate that Condition No. 3 has significantly more crack path tortuosity than either Conditions No. 1 or No. 2, Fig. 3.3-49. This observation is in agreement with the results of the $R = 0.1$ tests of the plate material, see Fig. 3.3-29. Measurements of secondary cracking, however, show that Condition No. 3 has the least, Fig. 3.3-50, in contrast to the $R = 0.1$ results. Comparisons of microscopic crack growth rates, i.e., the actual length of the main crack plus the length of all secondary cracks per cycle, show that crack path tortuosity and secondary cracking do

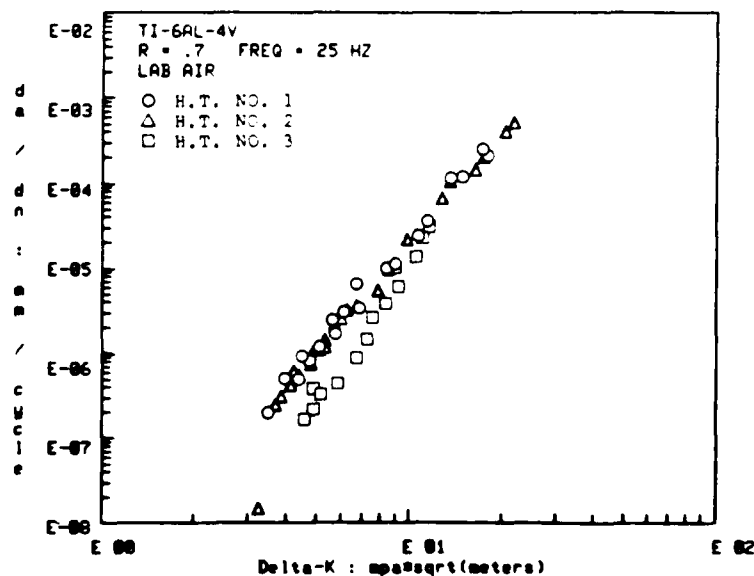


Fig. 3.3-48 da/dN vs ΔK , plate material, heat treatments No. 1, 2 and 3, $R = 0.7$.

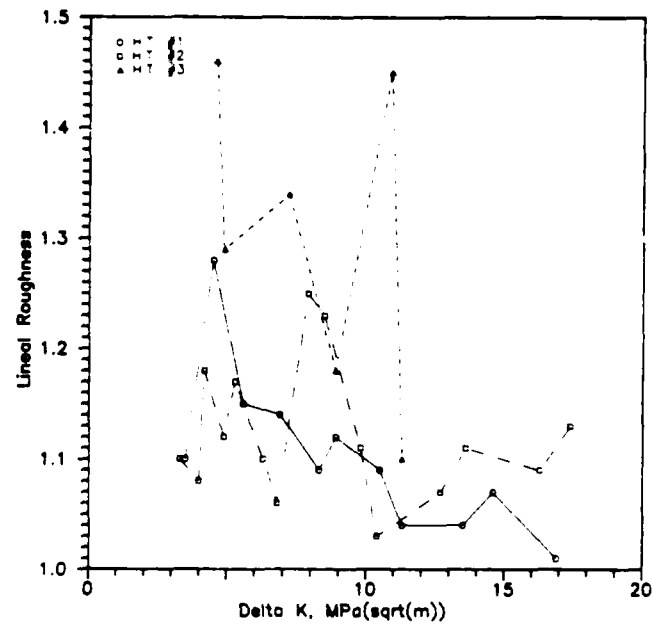


Fig. 3.3-49 Lineal roughness vs ΔK , plate material, heat treatments No. 1, 2 and 3, load increment data only, $R = 0.7$.

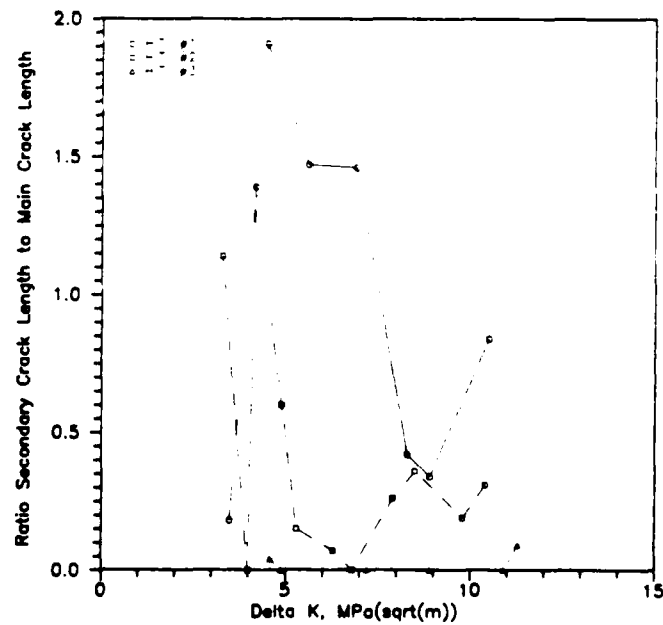


Fig. 3.3-50 Secondary cracking vs ΔK , plate material, heat treatments No. 1, 2 and 3, load increment data only, $R = 0.7$.



not account for the differences in growth rates in the three microstructural conditions. Such behavior indicates that microstructural variables contribute to the intrinsic crack propagation resistance.

3.3.4.5 Plate Material, R Ratio Effect

The effect of R ratio on crack growth rate is shown for the three heat treat conditions in Figs. 3.3-51 through 3.3-53. For each Condition, the crack propagates at a significantly faster rate when tested at $R = 0.7$ compared to $R = 0.1$. This behavior, which is typical of most alloy systems, has been explained in terms of crack closure effects (e.g., Refs. 14, 15). That is, the higher minimum stress that accompanies $R = 0.7$ shortens the time that the crack is closed during each cycle, resulting in a faster growth rate.

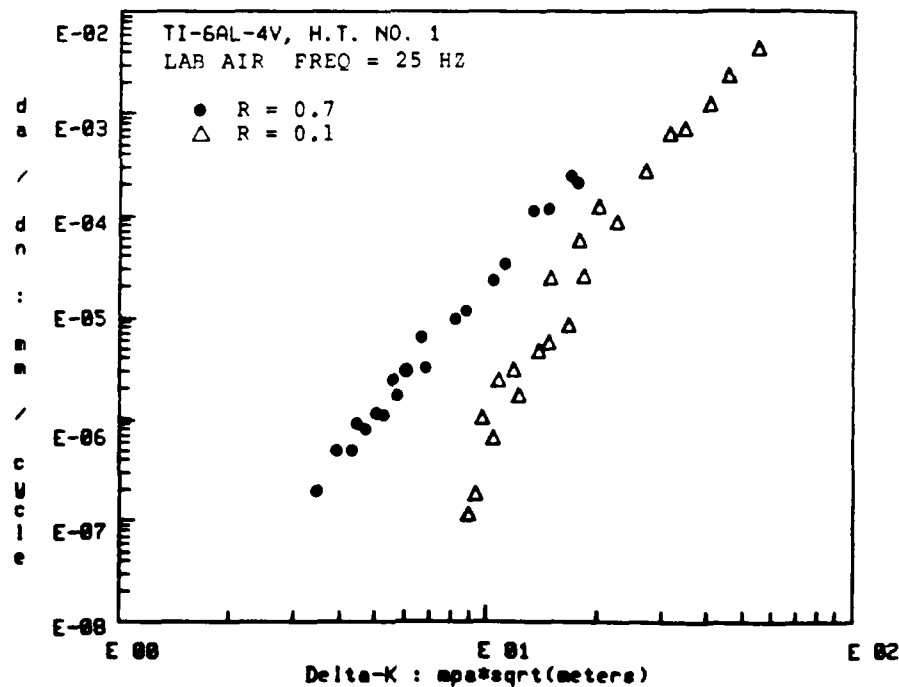


Fig. 3-3-51 Comparison of da/dN vs ΔK , plate material, heat treatment No. 1, at $R = 0.1$ and $R = 0.7$.

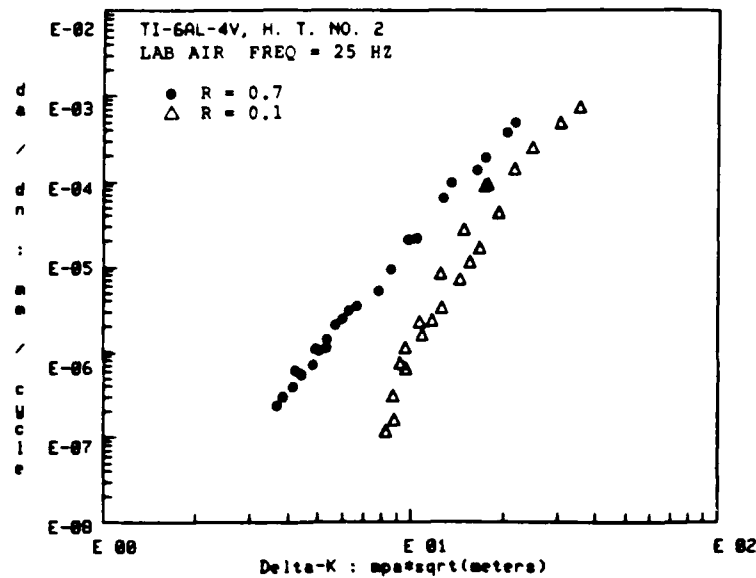


Fig. 3-3-52 Comparison of da/dN vs ΔK , plate material, heat treatment No. 2, at $R = 0.1$ and $R = 0.7$.

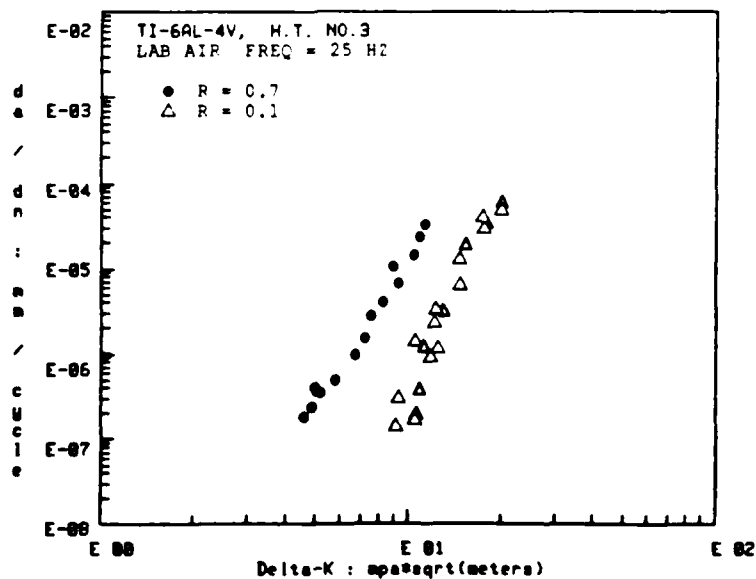


Fig. 3-3-53 Comparison of da/dN vs ΔK , plate material, heat treatment No. 3, at $R = 0.1$ and $R = 0.7$.



3.3.4.6 Forged Material, $R = 0.7$

Test data for the three conditions tested at an R ratio of 0.7 are shown in Fig. 3.3-54. As was observed for the plate material, the forged material tested at $R = 0.7$ exhibited no differences in growth rates between K -decreasing and K -increasing segments of the tests. Because the major difference in test conditions between $R = 0.1$ and 0.7 is the amount of closure the crack tip undergoes during each cycle, it can be assumed that roughness induced closure accounts for the differences in crack growth rates during K -decreasing and K -increasing portions of the tests at $R = 0.1$. Further, the lack of closure at $R = 0.7$ can explain the convergence of K -decreasing and K -increasing crack growth rate data of the forged material.

It is apparent from Fig. 3.3-54 that there are essentially no differences in crack growth rates among the three microstructural conditions. Crack path tortuosity, as measured by lineal roughness, is not significantly different among the three microstructural conditions, Fig. 3.3-55. The amount of secondary cracking is slightly greater for Condition No. 2 than for the other microstructural conditions, Fig. 3.3-56, especially

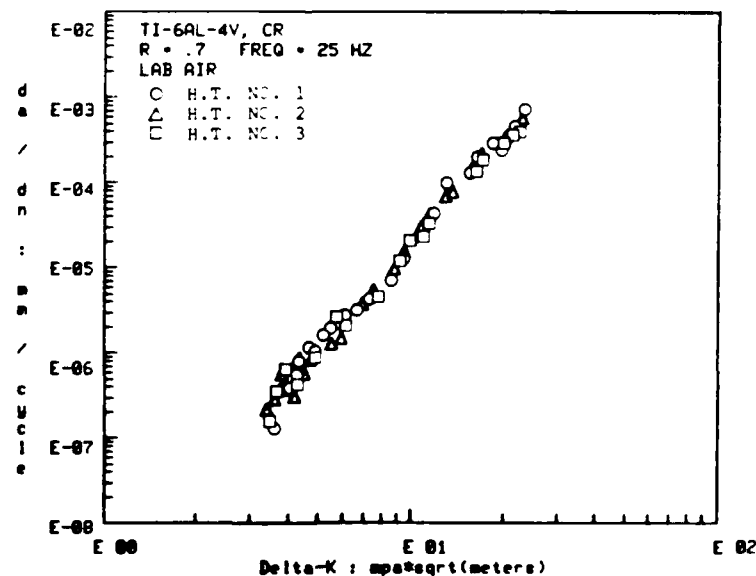


Fig. 3.3-54 da/dN vs ΔK , forged material, heat treatments No. 1, 2 and 3.

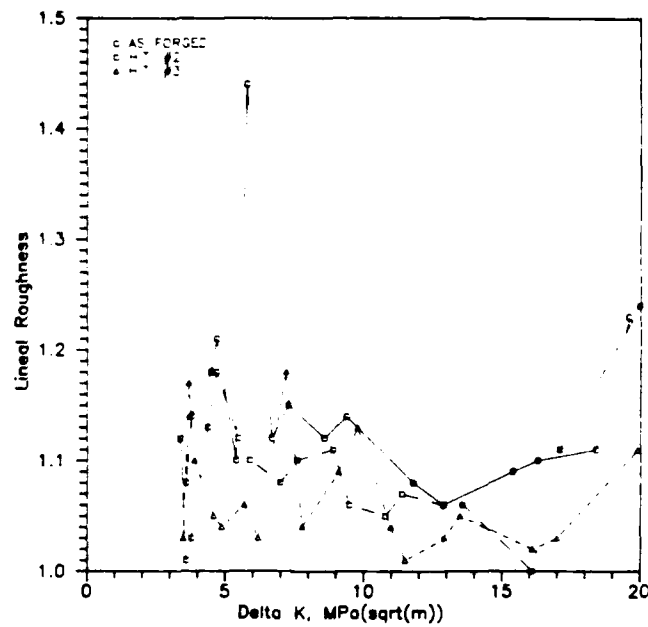


Fig. 3.3-55 Lineal roughness vs ΔK , forged material, heat treatments 1, 2 and 3, load increment data only, $R = 0.7$.

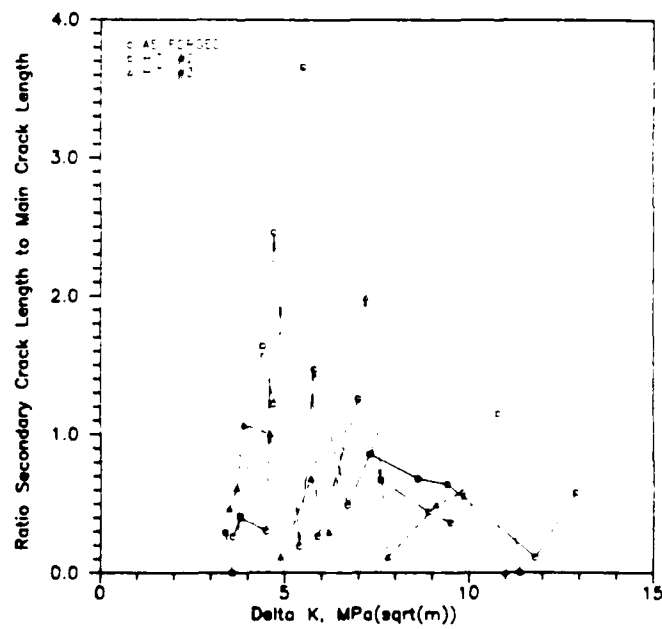


Fig. 3.3-56 Secondary cracking vs ΔK , forged material, heat treatment No. 1, 2 and 3, load increment data only, $R = 0.7$.



at the low ΔK region, which may account for the slightly lower crack growth rate for Condition No. 2 in the ΔK regime of $\sim 5\text{--}8 \text{ MPa}\sqrt{\text{m}}$. The relative degree of crack path tortuosity and secondary cracking among the three samples is similar to that observed for the forged material tested at $R = 0.1$.

Comparisons of crack growth behavior show that the cracks in the forging propagate at a rate similar to the rate of the most rapidly growing cracks in the plate material, cf. Figs. 3.3-54 and 3.3-48. That is, crack growth rates in the three forged material Conditions, Fig. 3.3-54, are approximately equivalent to the propagation rates measured for Heat Treat Conditions No. 1 and No. 2 of the plate material, Fig. 3.3-48. Condition No. 3 of the plate material exhibits the slowest crack growth rate of the six test conditions.

3.3.4.7 Forged Material, R Ratio Effects

The effects of R ratio on crack propagation rate in the forged material are shown for the three heat treat conditions in Figs. 3.3-57 through 3.3-59. As was the case

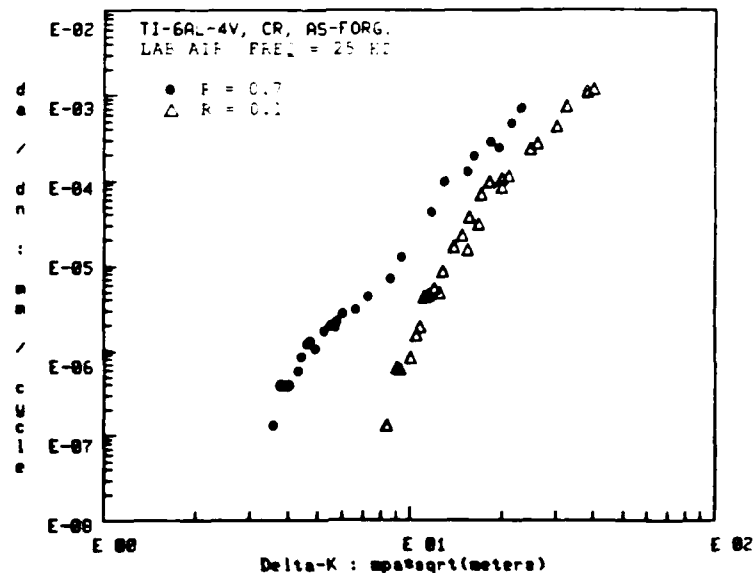


Fig. 3.3-57 da/dN vs ΔK , forged material, as-forged, at $R = 0.1$ and $R = 0.7$.

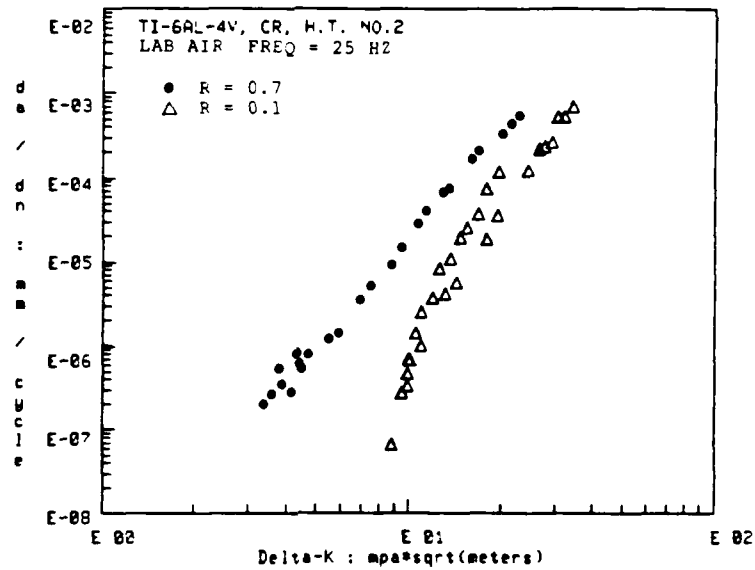


Fig. 3.3-58 da/dN vs ΔK , forged material, heat treatment No. 2, at $R = 0.1$ and $R = 0.7$.

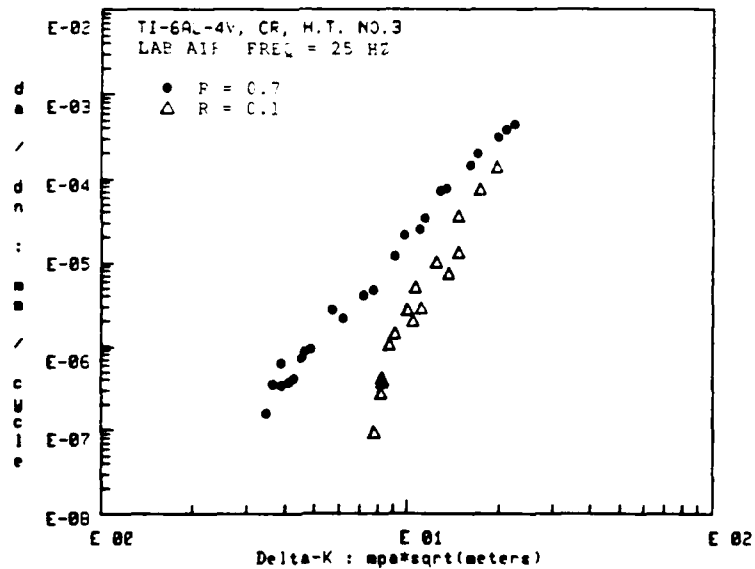


Fig. 3.3-59 da/dN vs ΔK , forged material, heat treatment No. 3, at $R = 0.1$ and $R = 0.7$.



for the plate material, the cracks propagate at significantly faster rates when tested at $R = 0.7$ compared to $R = 0.1$. The observation is consistent with the concept of a lower measured crack growth rate being the result of crack closure, which is reduced or eliminated at the higher R ratio (see Section 3.3.4.5).

3.3.4.8 Combined Results for Plate and Forged Materials, $R = 0.7$

The small differences in crack growth rates among five of the six tests indicates that microstructure has less influence on fatigue crack propagation resistance at the higher R ratio than was observed for the lower R ratio. Linear regression analysis of microstructural variables, then, might be expected to be less definitive in describing the influence of those variables on crack growth rate.

Multiple linear regression was nevertheless performed using the microstructural features quantified individually in Tables 3.3-2, 3.3-3, 3.3-5, and 3.3-6 (see also Section 3.3.4.3). The expression that comes from the analysis is

$$\ln da/dN = -8.3 + 18.6X1 - 0.11X2 + 0.11X3 - 0.0015X4 + 0.6X5 \quad (2)$$

where $X1$ = volume fraction beta phase,
 $X2$ = number of beta phase discontinuities $\times 10^{12} \text{ cm}^{-3}$,
 $X3$ = alpha phase plate width in micrometers,
 $X4$ = alpha colony size in micrometers,
 $X5$ = ΔK in $\text{MPa}\sqrt{\text{m}}$

and da/dN is in meters per cycle $\times 10^{-8}$. Figure 3.3-60 illustrates how well Eq. (2) predicts fatigue crack growth rates at $R = 0.7$. The correlation of calculated values with measured values is quite good at the slower growth rates, but deviates as da/dN exceeds 10^{-7} meters per cycle.

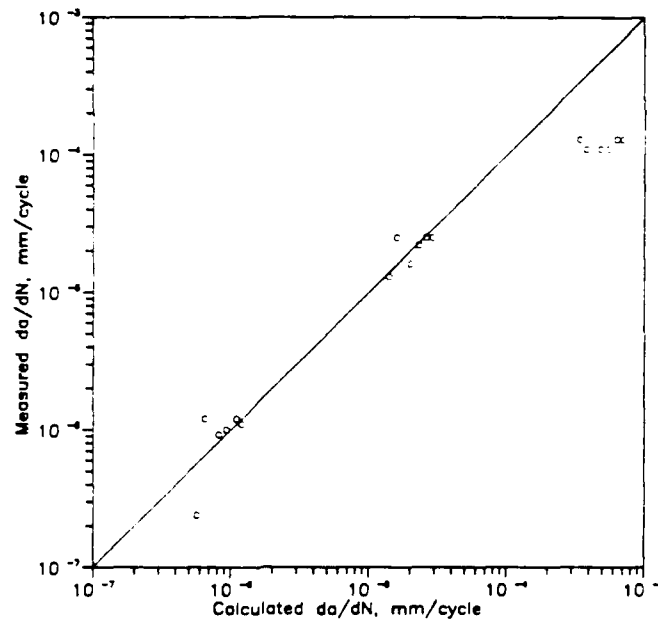


Fig. 3.3-60 Measured da/dN vs calculated da/dN at $R = 0.7$ for plate and forged materials using Eq. (2).

The relative contribution of the individual microstructural features to crack propagation resistance can be ascertained from the weighting factors (co-efficients) in Eq. (2). As was the case for $R = 0.1$ results, increasing the volume fraction of beta phase, the continuity of the beta phase, the size of alpha plates, or the stress intensity level increases the crack growth rate. Unlike the $R = 0.1$ case, Eq. (2) suggests that increasing the size of the colonies would decrease the crack growth rate. However, the relative contribution of the colony size is quite small, as indicated by the magnitude of the weighting factors, in both the $R = 0.1$ and $R = 0.7$ cases, see Eq. (1), Eq. (2), and Fig. 3.3-47.

Comparing the magnitudes of the coefficients, or weighting factors, of the individual microstructural features in Eqs. (1) and (2) is a measure of how the contribution of each parameter varies from $R = 0.1$ to $R = 0.7$. The weighting factor decreases for each microstructural feature as the test condition changes from $R = 0.1$ to $R = 0.7$. This result is consistent with the smaller observed differences in crack growth rates among the samples tested at $R = 0.7$.



It can be concluded from Eq. (2) that fatigue crack propagation resistance of beta processed Ti-6Al-4V exposed to an R ratio of 0.7 can be improved by reducing the volume fraction of beta phase and by reducing the alpha plate size.

3.4 Discussion

3.4.1 Microstructure

The heat treatments used in this program were designed to produce systematic and significant variations in microstructure such that the influence of beta processing on fatigue crack propagation in Ti-6Al-4V could be analyzed. Large variations in each of the parameters were indeed the result of the three heat treatments. It was also important that all the microstructural parameters not vary in the same way with heat treatment, e.g., in the plate material Conditions No. 2 and No. 3 produced similar values for beta phase discontinuities that were quite different from the value produced by Condition No. 1, whereas Conditions No. 1 and No. 2 generated similar values for alpha plate size compared to the value generated by Condition 3. Testing of three heat treat conditions in each of the two starting lots of material, then, was sufficient to evaluate the influence of individual parameters on fatigue crack propagation rates.

The objective of the heat treatments was not to produce any particular combination of microstructure sizes or distributions, but rather was to generate a spread in values of the significant features. It is therefore not important that heat treat No. 1 (or No. 2 or No. 3) did not produce exactly the same values in the plate material as it did in the forged material for each of the microstructural parameters. It is important, however, that material factors which could contribute to fatigue crack resistance but were not included in the quantitative analyses be constant from plate to forging. These factors that could influence fatigue crack growth behavior in the present study are the microstructural parameters prior beta grain size and the amount of grain boundary alpha and the non-microstructural feature, oxygen level. Each of these factors was relatively constant in the six different heat treat conditions. The quantified parameters were therefore sufficient to describe fatigue crack growth behavior in beta treated Ti-6Al-4V.



3.4.2 Fatigue Crack Propagation Behavior

3.4.2.1 Variation With Heat Treatment

Tables 3.3-2 through 3.3-6 demonstrate that a large distribution in microstructural variables was generated in the fatigue tested samples. However, Figs. 3.3-27 and 3.3-40, or 3.3-48 and 3.3-54, clearly indicate that large variations in beta phase distributions, alpha phase plate widths, or Widmannstatten colony size result in crack growth rates that vary, at most, by about a factor of two or three. This spread in the data is approximately equivalent to that reported in the literature for beta-treated (other than quenched) microstructures in Ti-6Al-4V.^{9,16,17}

Oxygen levels in the plate and forged materials were 1240 and 1300 ppm, respectively. So, although oxygen concentration can have an effect on fatigue crack growth rate⁹ in Ti-6Al-4V, the spread in data observed in this study is not influenced by oxygen. Analysis has shown that the variation in crack growth rate from sample to sample can, in fact, be correlated to changes in microstructure.

3.4.2.2 Effect of R-ratio on Crack Growth Rate

The increase in fatigue crack growth rate at $R = 0.7$ over that at $R = 0.1$ for identical stress intensity levels can be explained in terms of crack closure.^{14,15} The crack can close on itself during the minimum stress portion of the fatigue cycle if the minimum load is sufficiently low. Upon increasing the load from minimum stress to maximum stress level, a portion of the applied stress is consumed in reopening the crack before propagation can proceed. The effective stress intensity level, i.e., that acting on the growing crack, will be less than the apparent, or measured, stress intensity level. When closure occurs during the fatigue cycle, then, the crack will appear to grow at a slower rate when measured as a function of the uncorrected stress intensity level.

Crack closure during fatigue testing of titanium alloys has been measured by others.^{15,18} Gross and Bose¹⁸ have shown that for beta-annealed Ti-6Al-4V a significant amount of crack closure could be measured for tests run at $R = 0.1$, but no closure could be detected in tests run at $R = 0.2$, using the method developed by Gan.¹⁹ For the present case, crack closure would be expected at $R = 0.1$, and, whether or not there is closure at $R = 0.2$, most certainly no closure would be anticipated at $R = 0.7$.



Roughness induced closure is a prominent mechanism for slowing the apparent crack growth rate,^{14,15} and if it were to contribute to the differences in growth rates for the three microstructural conditions tested at $R = 0.1$ (see Figs. 3.3-27 and 3.3-40), the difference between growth rates at $R = 0.1$ and $R = 0.7$ should be greatest for Condition No. 3 of the plate material and Condition No. 2 of the forged material. Inspection of Figs. 3.3-51 through 3.3-53 reveals that, over the ΔK range of 10-15 $\text{MPa}\sqrt{\text{m}}$, Condition No. 3 has the largest difference in growth rates between $R = 0.1$ and $R = 0.7$, while Condition No. 2 exhibits the smallest difference. Similarly, for the forged material, Figs. 3.3-57 through 3.3-59 demonstrate that Condition No. 2 has the largest difference in growth rates between $R = 0.1$ and 0.7 over the ΔK range of 10-20 $\text{MPa}\sqrt{\text{m}}$. Such behavior is consistent with roughness induced closure occurring at $R = 0.1$ testing. This phenomenon, then, can account for the differences in crack growth rates at $R = 0.1$ and $R = 0.7$.

3.4.2.3 Differences Between K-Decreasing and K-Increasing Crack Growth Rates

Both the plate and forged materials exhibited faster crack propagation rates during load-shedding (K-decreasing) portions of the fatigue tests than during K-increasing segments, see Figs. 3.3-15 through 3.3-17 and 3.3-31 3.3-33. The special test results illustrated in Figs. 3.3-18 and 3.3-19 demonstrated that the load-shed/load-increment effect was not simply a crack length phenomenon. Crack path analyses, on the other hand, showed that there was significantly more crack tortuosity and secondary cracking during the K-increasing test segment, thereby correlating with slower growth rates.

The reasons for increased crack path tortuosity and branching during the K-increasing portions of the tests are not clear. It has been suggested by Mitchell²⁰ that load shedding, with decreasing crack opening displacements, results in lower compressive stresses during the minimum portion of the cycles than would be generated during load incrementing. The reduced compressive stresses translate to higher average mean stresses during load shedding, which can account for the faster growth rates observed. Although the precise mechanism for the variation in growth rates can only be speculated upon at this time, it is apparent that the stress conditions in and around the crack tip are different for the different test conditions.



When the minimum stress level of the fatigue cycle is increased ($R = 0.7$), the amount of crack closure that can occur during the minimum loading segment of each cycle is reduced.^{14,15} It has recently been reported that there is no measurable crack closure in Ti-6Al-4V tested at $R = 0.2$,¹⁸ so closure likely has no effect on crack growth rate for material tested at $R = 0.7$. Roughness induced closure, then, can make a significant contribution to the slower crack growth rates measured during increasing- ΔK portions of the tests conducted at $R = 0.1$, and is nonexistent at $R = 0.7$. Secondary crack-ing, which is more extensive during the K-increasing segments of the tests, is also a contributor to reduced crack growth rates.

3.4.3 Correlation of Crack Propagation With Microstructure

3.4.3.1 Effects of Microstructure on Crack Growth Rates

The linear regression analyses performed for $R = 0.1$ (Eq. (1)) and $R = 0.7$ (Eq. (2)) demonstrate the combined effects of the various microstructural features on fatigue crack growth rates in Ti-6Al-4V. Figure 3.3-43 clearly shows that Eq. (1) very reliably predicts crack growth rates over three orders of magnitude of growth rates. Such behavior indicates strongly that crack propagation rates at $R = 0.1$ are microstructure dependent at stress intensity levels up to about $20 \text{ MPa}\sqrt{\text{m}}$. On the other hand, Fig. 3.3-60 reveals that Eq. (2) is operative up to crack growth rates of 10^{-4} mm/cycle , but begins to fall off at faster rates. This would suggest that microstructural effects become less significant at stress intensity levels above about $10 \text{ MPa}\sqrt{\text{m}}$ for $R = 0.7$ testing. The difference between $R = 0.1$ and $R = 0.7$ test conditions, as discussed earlier, is most likely associated with crack closure effects.

Equations (1) and (2) also provide a quantitative measure of the relative contributions of individual microstructure features to the fatigue crack growth rates. For instance, it was shown in Figs. 3.3-44 and 3.3-45 that crack growth resistance can be improved by reducing the volume fraction and continuity of the beta phase. However, it is clear from Eq. (1) and Figs. 3.3-44 and 3.3-45 that volume fraction has a greater effect on crack growth rate than does beta phase continuity. That is borne out in the measured crack growth rates of plate Samples No. 1 and No. 3 in which these two parameters vary



in opposite directions. That is, plate Sample No. 1 has a larger volume fraction and a smaller beta phase continuity than plate Sample No. 3, and it is No. 3 which has the slower crack growth rate.

The effect of the Widmanstatten alpha colony size on crack growth rate was shown in Fig. 3.3-47. The reversed plastic zone sizes in all samples for the stress intensity range of 12-20 MPa \sqrt{m} are smaller than the respective colony size, a condition which Yoder et al.⁹ suggest represents a microstructure sensitive region. Specimen width: colony size ratios ($B:\bar{\lambda}$) for the six test specimens are given in Table 3.4-1. All six have $B:\bar{\lambda}$ values that fall between the two extremes studied by Yoder and Eylon,¹⁰ i.e., $2 < B:\bar{\lambda} < 668$. For tests in which $B:\bar{\lambda}$ was less than 2, Yoder and Eylon¹⁰ showed that colony size influenced da/dN in exactly the opposite manner as those tests wherein $B:\bar{\lambda}$ was greater than 668. The data in Table 3.4-1 and Eq. (1) (Fig. 3.3-47) indicate that colony size has little effect on fatigue crack growth rates for $67 < B:\bar{\lambda} < 423$. In contrast to Yoder's suggestions, it has recently been reported that crack closure effects, and not Widmanstatten colony size, most significantly influence fatigue crack growth rates.¹⁸ The results presented here strongly suggest that the synergistic effects of several microstructural parameters override the effect of any single parameter, and that it is probably an oversimplification to suggest otherwise.

Table 3.4-1
Specimen Width:Colony Size for Ti-6Al-4V

Condition No.	Colony Size (μm)	Specimen Width: Colony Size ($B:\bar{\lambda}$)	da/dN @ 10 MPa \sqrt{m}
Plate 3	190	67	1×10^{-10} m/cycle
Forging 3	189	67	1.5×10^{-9}
Forging 0	125	102	1.7×10^{-9}
Forging 2	124	102	5×10^{-10}
Plate 2	58	219	1.5×10^{-9}
Plate 1	30	423	5.5×10^{-10}



3.4.3.2 Effects of Microstructure on Crack Path

The cracks move through the microstructure in a similar manner in all six heat treat conditions: maintaining a large angle, when possible, with the longitudinal axis of the alpha plates resulting in deflection of crack direction when passing from one colony to the next. The crack direction will be determined by the orientation of the Widmanstatten colony with respect to the applied stress axis. It has been shown that a fatigue crack will propagate primarily along, or near, (0001) or, secondarily, on (1010) alpha phase planes.^{21,22} The Burgers orientation of alpha plates transformed from the beta in a Widmanstatten configuration is such that the basal plane is perpendicular the the longitudinal axis of the plate. Cracks that follow on, or near, basal planes, then, will maintain a large angle with the longitudinal axis of the alpha plates.

There was no evidence of significant crack propagation along alpha-beta boundaries or along prior beta boundaries with or without grain boundary alpha.

3.4.3.3 Effects of Microstructure on Secondary Cracking

Secondary, or branched, cracks appear to nucleate primarily when the crack front passes from one colony to the next. The two, or more, branches then propagate simultaneously during cycling, with one eventually continuing as the main crack, while the others are held up trying to cross boundaries.

The amount of secondary cracking does not directly correlate with any of the individual microstructural features quantified in this study. Secondary cracks are most extensive in Condition No. 3 of the plate material, which has the lowest volume fraction of beta phase, largest Widmanstatten colony size, and largest alpha plate width of the six different test conditions. However, Condition No. 1, which exhibits the largest volume fraction of betaphase, the smallest colony size, and the smallest alpha plate width, contains only slightly less secondary cracking than Condition No. 3 and considerably more than the other four conditions. The propensity for secondary cracking also does not correlate with yield strength.

The tendency for the crack to branch appears to be the result of a complex combination of microstructural parameters, much like that observed for the crack



growth rate. Although no regression analysis was performed on the secondary cracking phenomenon, such an analysis could define the relative contributions of the various microstructural features to this effect.

3.4.3.4 Effects of Microstructure on R-ratio Behavior

It was pointed out in Sect. 3.5.2.2 that the accelerated crack growth rates observed for testing at $R = 0.7$ compared to those at $R = 0.1$ could be attributed to crack closure during the latter condition. Any influence that microstructure might have on the R effect of fatigue crack growth behavior, then, would be its influence on closure. The analysis in Sect. 3.5.2.2 also indicated that, for these test conditions, roughness-induced closure was the most prominent of the closure mechanisms. Crack path tortuosity dictates the degree of roughness-induced closure, hence, any influence of microstructure on closure would be through its influence on tortuosity.

It has been suggested that, over a given stress intensity range, the degree of crack path tortuosity should increase with increasing Widmanstätten colony size.^{9,10} That generality, however, does not hold for the present case. For instance, although plate Condition No. 3 has the largest colony size and the greatest average crack path tortuosity, plate Condition No. 1 has the smallest colony size with the second greatest average tortuosity, Fig. 3.3-29. Similarly for the forged material, Condition No. 3 has the largest colony size, yet the average lineal roughness is about the same for the Conditions No. 0, 2, and 3.

There is no simple correlation of crack path tortuosity with any of the microstructural features quantified in this study. Regression analysis is one method that could be applied to discover the influence of the microstructural features on tortuosity, but it has not been done in this program.

3.5 Conclusions

This study has shown the following:

1. Microstructural variations can account for the spread in da/dN data reported in the literature for beta processed Ti-6Al-4V;



2. Linear regression analysis can be used to describe the manner by which volume fraction beta phase, continuity of beta phase, width of alpha phase plates, and size of Widmanstatten alpha colonies influence fatigue crack propagation rates in beta treated Ti-6Al-4V;
3. Fatigue crack propagation resistance of beta treated Ti-6Al-4V can be improved by decreasing the volume fraction and continuity of the beta phase, by decreasing the alpha plate width, or by decreasing the Widmanstatten alpha colony size;
4. Beta phase volume fraction is the most influential of the microstructural parameters, while colony size is the least influential;
5. The mechanisms by which microstructure influences crack propagation rates are (1) changing the inherent resistance to crack propagation by altering the reversed plastic zone size through changes in the yield strength, (2) changing the direction of the advancing crack to produce varying degrees of crack path tortuosity, and (3) changing the tendency for bifurcation of the crack;
6. Crack growth rates are significantly faster at $R = 0.7$ than at $R = 0.1$ for all microstructural conditions, which is suggested to be the result of crack closure at the lower R ratio tests;
7. Crack growth rates for material tested at $R = 0.1$ are faster during K-decreasing (load shedding) test segments compared to K-increasing (load increment) test regimes;
8. There was significantly more secondary cracking and crack path tortuosity during the K-increasing portion of the tests than during the K-decreasing segments.



3.6 Part I - References

1. C.G. Rhodes, M.R. Mitchell, and J.C. Chesnutt, "Fracture and Fatigue Characteristics in Ti Alloys," Final Report, SC5227.1FR, ONR Contract N00014-76-C-0567, June 1982.
2. "Development of Structural Titanium Alloy for Naval Application," Navy Contract N00024-79-C-5636.
3. J.E. Hilliard and J.W. Cahn, Trans. Met. Soc. AIME, Vol. 221, 1961, pp. 344-352.
4. K. Banerji and E.E. Underwood, Acta Stereol. 2, 65-70 (1983).
5. M.A.W. Loudon and W.B. Hutchinson, Met. Trans. 6A, 441-448 (1975).
6. A.W. Bowen, Mat. Sci. and Engr. 29, 19-28 (1977).
7. J.M. Fitzpatrick, F.A. Crossley, and R.E. Lewis, Met. Eng. Quart. 12, 27-31 (1972).
8. M.F. Amateau, D.L. Dull, and L. Raymond, Met. Trans. 5, 561-564 (1974).
9. G.R. Yoder, L.A. Cooley, and T. W. Crooker, Met. Trans., 9A, 1413-1420 (1978).
10. G.R. Yoder and D. Eylon, Met. Trans. 10A, 1808-1810 (1979).
11. C. G. Rhodes, Electron Microscopy 1982, vol. 1, The Congress Organizing Committee, eds., Deutsche Gesellschaft fur Elektronenmikroskopie, Frankfurt, 1982, pp. 663-664.
12. R.J. Bucci, in Fatigue Crack Growth Measurement and Data Analysis, ASTM-STP 738, ASTM, Philadelphia, PA, 1981, pp. 5.
13. A. Ayvazian and R. Colton, The Science, Technology and Application of Titanium, R.I. Jaffee and N.E. Promisel, eds., Pergamon Press, NY, 1970, pp. 897-899.
14. R.O. Ritchie, J. Eng. Mat. & Techn. 99(H) 195-204 (1977).
15. J.E. Allison and J.C. Williams, in Titanium Science and Technology, G. Lutjering, U. Zwicker, W. Bunk, eds., Deutsche Gesellschaft fur Metallkunde e. V., Oberursel, W. Germany, 1984, pp. 2243 - 2250.
16. J.C. Chesnutt, A.W. Thompson, and J.C. Williams, "Influence of Metallurgical Factors on the Fatigue Crack Growth Rate in Alpha-Beta Titanium Alloys," AFML-TR-78-68, May, 1978.



17. J.C. Chesnutt, A.W. Thompson, and J.C. Williams, Titanium '80 Science and Technology, H. Kimura and O. Izumi, eds., The Metallurgical Society, Warrendale, PA, 1980, pp. 1875-1882.
18. T.S. Gross and S. Bose, J. Metals 37, A107 (1985), presented at TMS-AIME annual meeting, New Orleans, 1986.
19. D. Gan and J. Weertman, Eng. Frac. Mech. 15, 87-106 (1981).
20. M. Mitchell, Rockwell International Science Center, Thousand Oaks, CA, private communication.
21. D. Schechtman and D. Eylon, Met. Trans. 9, 1018-1020 (1978).
22. K.S. Chan and D.A. Koss, Mat. Sci. and Engr. 43, 177-186 (1980).



4.0 PART II. MECHANISTIC ASPECTS OF SUPERPLASTICITY IN Al ALLOYS

4.1 Background

It has been shown recently that grain refinement in conventional high-strength Al alloy can lead to its superplastic capability.¹ This offers the potential for significant cost and weight payoff for aerospace structures, and it is likely that this emerging technology will impact the next generation of aircraft by offering this novel capability. While progress continues in the implementation of this technology, uncertainties and problems occur periodically during application because of poor understanding of the superplastic flow behavior and the underlying mechanisms. This three-year program has addressed several of these needs as well as the consolidation mechanics for P/M Al alloys.

The importance of grain boundary sliding and fine grain size on superplasticity is reasonably well accepted. However, the roles of significant distributions in grain size and microstructural changes occurring during superplastic deformation are poorly understood.²⁻⁴ Understanding was lacking as to whether the real behavior of materials follow iso-strain rate or iso-stress models of deformation in various grains. This is of particular importance in designing alloys with improved superplasticity, as well as in determining the optimum processing conditions for their fabrication. The presence of a strong bimodal grain size distribution, as often observed in production heats of Al alloys, may not influence the room-temperature service properties in any significant manner, but can drastically alter the superplastic properties.

In the majority of the mechanistic studies,⁵⁻¹⁰ a factor that has been ignored until recently^{11,12} is the existence of distributions in grain size. As shown in Ref. 11, while fine grain superplastic metals may have a grain size peak around 5-10 μm , a long tail may exist at much larger grain sizes ($\sim 30-40 \mu\text{m}$). Consequently, any real alloy behaves like a composite material, the fine grains having a different constitutive equation from the coarse grains. Two phase materials (e.g., Ti-6Al-4V, Zn-Al eutectoid, etc.) further possess differences in diffusion coefficients⁶ which allow a widely distributed constitutive behavior to be established. It has been possible to show that distributions in metallurgical features such as these could lead to transition from power law to diffusion



creep (i.e., region III) which is spread over several decades in strain rate. An assumption which has been tacitly made in such a model is that the same overall strain rate is imposed over a group of fine grains as that over a group of coarse grains. This method provides for the development of internal stress within the material, the coarse grains supporting a higher stress. As opposed to this parallel model, a series model would demand the imposition of iso-stress condition on all grains and allow the strain rates from fine and coarse grains to be added.

Experiments performed with a model material composed of fine and coarse grain sizes were performed to gain an understanding of the deformation mechanism as well as the microstructural changes during deformation. A new deformation model has been developed based on the observations of these microstructural changes which can explain the large strain flow characteristics of these materials.

It is known that the application of hydrostatic pressure during superplastic forming can suppress cavitation and enhance ductility.¹ It is not known, however, if the effect of hydrostatic pressure is one of suppression of the void nucleation process or the void growth process, or both. Since the nucleation mechanisms are believed to be diffusion-controlled and growth mechanisms are dislocation creep-controlled, the pressure required for suppression of cavitation could be significantly different for the two cases. Critical experiments were conducted in this program to gain an understanding of this process.

The advent of the RSR powder Al alloys promises higher strength and temperature capabilities in aircraft structures. To take advantage of the full potential of these materials, an understanding of the process mechanics and optimization must be made. An understanding of the void closure process and the flow of powder particle surface during multiaxial deformation has been developed here through the development of a deformation model of the powder mass and parallel experiments on 7075 Al powder. Additional insight is gained through experiments on premachined spherical voids in the 7475 Al alloy. These mechanistic aspects of superplasticity and processing of powder Al alloys are discussed in the following sections.



4.2 Objectives

The objectives of Part II of this program are to:

1. Determine the effect of grain size distribution on the superplastic flow behavior of fine grain 7475 Al, and examine its relationship to deformation.
2. Characterize the microstructural changes occurring in various grains during superplastic deformation of fine grain 7475 Al and develop a dynamic deformation model based on variable microstructures.
3. Assess the effect of hydrostatic pressure on cavity nucleation and cavity growth in fine grain 7475Al.
4. develop an understanding of the void closure process during consolidation of Al powder under a variety of stress states.

4.3 Progress

Significant process has been achieved in each of the areas outlined in the objectives above. These are described in the following sections.

4.3.1 Progress in Superplastic Mechanisms

A model material was fabricated by lamination of fine and coarse grain 7475 Al alloy sheets (containing 5.1% Zn, 2.1% Mg and 1.5% Cu in solid solution, as well as precipitate forming agents and 0.2% Cr as a dispersoid former). The fine grain sheet material was produced by thermomechanical processing from plate 7475 alloy using a patented process¹³ which involves overaging the alloy at 400°C for 8 h after solution treatment (516°C), rolling 90% at 200°C, and subsequently recrystallizing at 516°C. The average grain size of the 2.54 mm thick material so produced was in the neighborhood of 8-12 μm . To produce the coarser grain material, a portion of this sheet was given a 20% rolling reduction at room temperature, followed by a recrystallization treatment at



516°C. This produced grain sizes in the neighborhood of 75 μm . These sheets were thoroughly cleaned, surface abraded, and stacked alternately with fine and coarse grain sheets of 50 mm x 50 mm size to develop a composite with 61% fine grains mixed with 39% coarse grains by volume. The stack was placed inside a stainless steel vacuum bag and press consolidated at 516°C after vacuum outgassing long enough to reach 2×10^{-6} mm Hg in the vacuum gauge. This forge compaction step was carried out in two stages to a total reduction of 8:1 at an overall strain rate of $2 \times 10^{-4} \text{ s}^{-1}$ which has previously shown to generate negligible grain growth. The forged block has been sectioned and metallographically evaluated. The microstructures of starting fine and coarse grain materials and the laminated mixed grain size model material are shown in Fig. 4.3-1. As expected, the mixed nature of grain size is visible, however, some refinement of microstructure has taken place.

Tensile specimens were machined from the forged block in the plane of laminations (L and T), as well as perpendicular (S) to the lamination planes. The stress vs strain rate plots (from jump test) between the individual directions were not significantly different. However, the S direction had the lowest peak in value (0.60) as compared with 0.75 for the T direction. Figure 4.3-2a shows stress vs strain rate data for the fine grain, coarse grain and mixed grain size materials. For the coarse grain material, the results are shown at three different temperatures: 482°C, 516°C and 530°C, the highest temperature producing the most unstable flow. The data for mixed grain size fall between fine and coarse grain results with a slope approaching that of the fine grain Al. Also shown in Fig. 4.3-2a are calculated σ - $\dot{\epsilon}$ plots for mixed grain material obtained from the individual curves for fine and coarse grain materials based on iso-stress and iso-stress rate assumptions. Clearly, iso-strain rate assumption fits the experimental results on the mixed grain (61:39) size material well, except for the very low strain rates. This happens because of short transients for coarse grain materials and long transients for fine grain material at the lower strain rates, the calculation of steady-state flow stress is biased toward coarse grain size data. Since at low rates the mixed grain size also shows significant transients, the measured stresses are expected to be lower than the steady state values that are calculated. The strain-rate sensitivity values (m) determined from the slope of these curves are shown in Fig. 4.3-2b. Mixed grain size produced an intermediate value of m between the high of fine grain ($m = 0.9$) and the low of coarse grain ($m = 0.2$) materials, with a peak shifted to lower strain rate than that of fine grain materials.



SC5358.4FR

SC84-25980

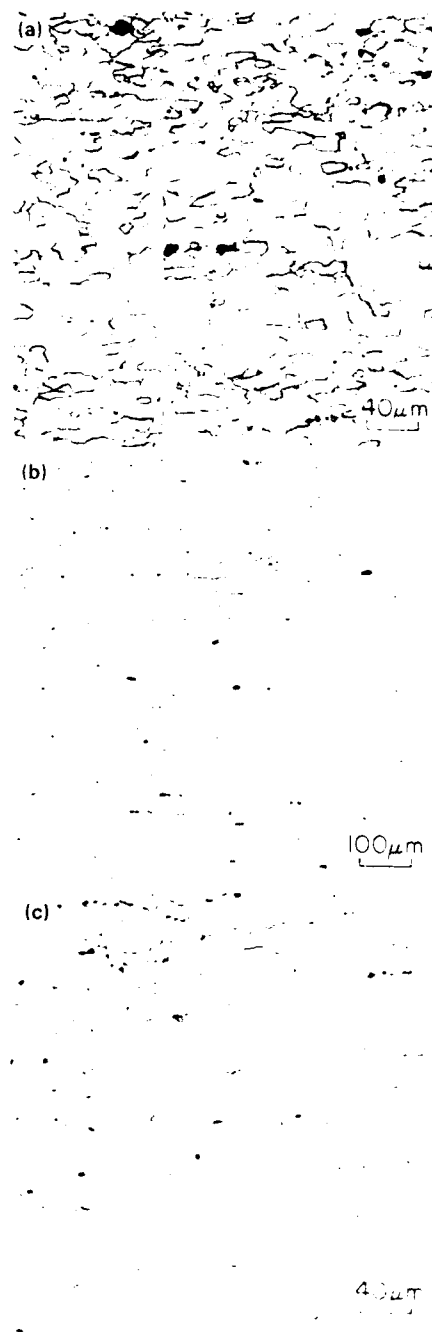


Fig. 4.3-1 Grain structures of the constituent fine grain (1), coarse grain (b) materials, and the resultant mixed grain model material (c). All sections in LS plane for 7475 Al. Average grain sizes are 12, 75 and 45 μm , respectively.

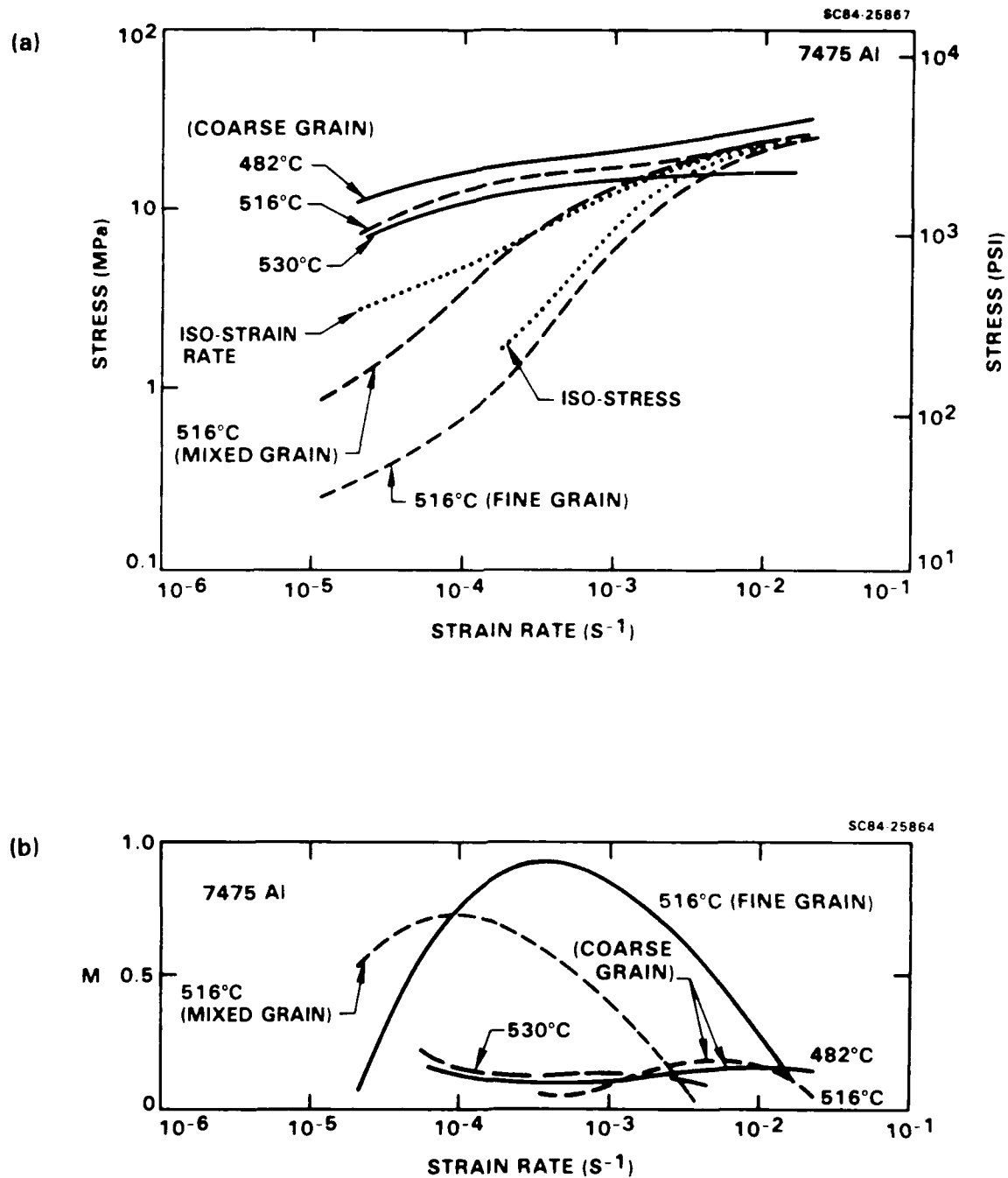


Fig. 4.3-2 (a) Stress vs strain-rate data from step strain-rate test, and (b) m (slope of (a)) vs strain rate for three different grain size conditions.



The mixed grain size produced intermediate elongation of 360% at $2 \times 10^{-4} \text{ s}^{-1}$ (516°C) as compared with 1072% for fine grain and 63% for coarse grain materials. While the S direction had a slightly lower flow stress, it also exhibited delamination at oxide layers, leading to low elongations. The application of a superimposed hydrostatic pressure,¹⁴ which aids in the suppression of superplastic cavities, was also found to help increase the elongation in the S direction to 122%. The typical σ - ϵ curves (at constant $\dot{\epsilon}$) for fine grain, coarse grain and mixed grain materials are shown in Fig. 4.3-3a, b and c. Again, fine grain materials exhibit significant flow hardening at all strain rates, coarse grain materials exhibit flow softening, and mixed grain materials exhibit a period of flow hardening, followed by a flow softening. It is believed that dynamic grain growth, along with a continuous change in the ratio of grain boundary sliding/dislocation creep, is responsible for the flow hardening behavior, whereas strain localization and dynamic recrystallization (grain refinement) of the coarse grains lead to flow softening.

Microstructural Changes

The most important microstructural changes observed during superplastic deformation of 7475 Al are dynamic grain growth at relatively low strain rates and/or fine grain sizes, and dynamic recrystallization (or grain refinement) at higher strain rates and/or coarse grain sizes. These processes appear to occur continuously as a function of strain rates in a given material. Grain growth occurs at $5 \times 10^{-5} \text{ s}^{-1}$ and $2 \times 10^{-4} \text{ s}^{-1}$ and grain refinement at 10^{-2} s^{-1} . The extent of dynamic grain growth is greater than static, as shown in the interrupted data of Fig. 4.3-4. There does not appear to be a strong strain-rate dependence of grain growth rate, although grain growth kinetics at 10^{-3} s^{-1} are somewhat more rapid. At 10^{-2} s^{-1} , there is no grain growth, simply grain deformation causing elongation along longitudinal and contraction along transverse directions. Since dynamic grain growth occurs at lower strain rates and dynamic recrystallization at higher strain rates, it is expected that grain size would remain unchanged at some intermediate strain rate. However, such a rate might be close to 10^{-2} s^{-1} and does not coincide with that of peak m or peak elongation ($\sim 2 \times 10^{-4} \text{ s}^{-1}$). Thus, the high flow stability at $2 \times 10^{-4} \text{ s}^{-1}$ is not related to a fixed microstructure and might be partly associated with flow hardening from dynamic grain growth.

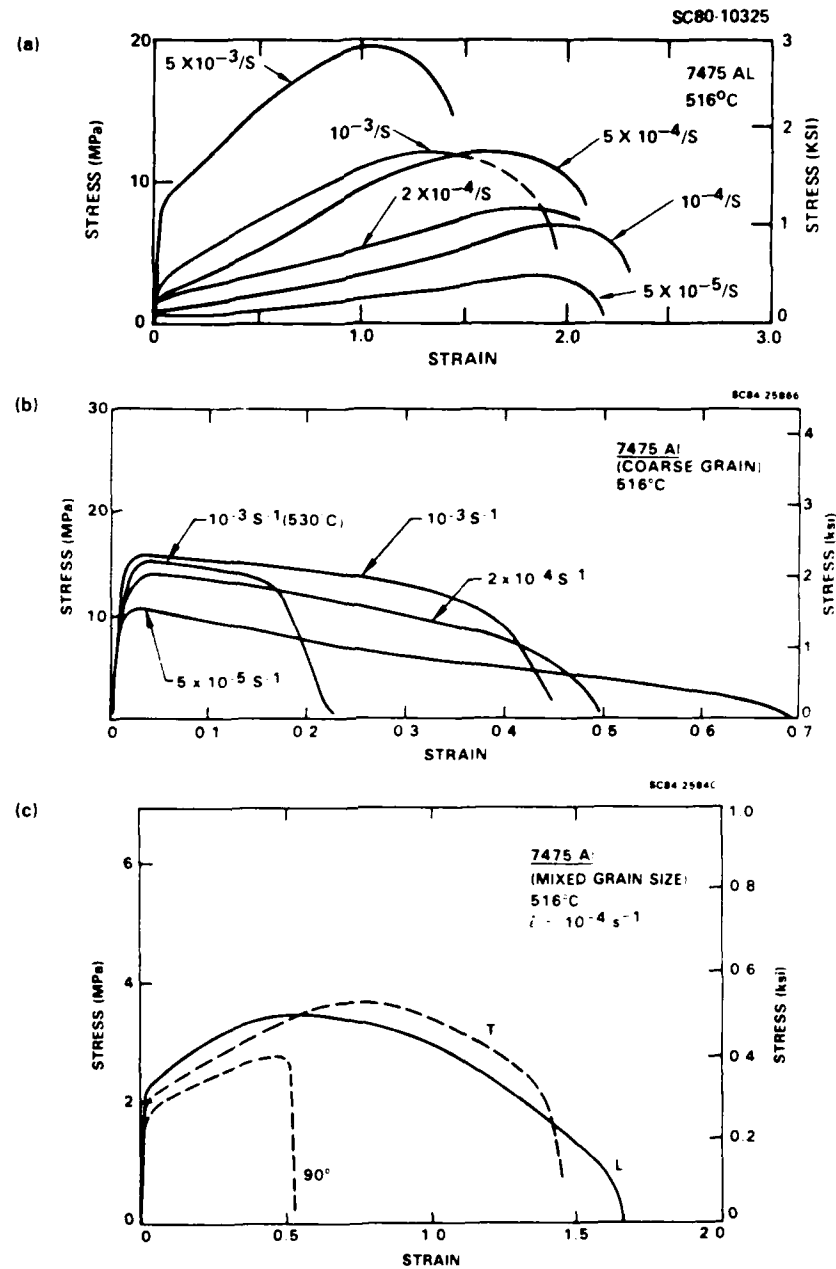


Fig. 4.3-3 Stress strain curves at various constant strain rates for (a) fine grain, (b) coarse grain, and (c) mixed grain size 7475 Al alloys.

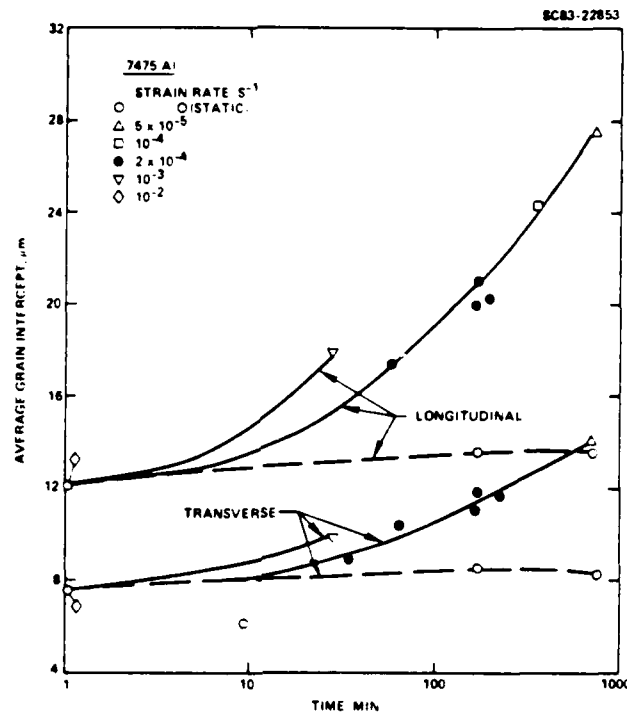


Fig. 4.3-4 Dynamic grain growth from interrupted tests at various constant strain rates compared with static grain growth for the fine grain 7475 Al.

Figure 4.3-5 shows dynamic recrystallization effects in the coarse grain material after modest amounts of deformation. At all strain rates, larger grains were found fragmented into finer grains. It appears that a critical plastic work for recrystallization is reached first in the larger grains, and subsequently in the smaller grains. It is also found that after a high strain-rate deformation at 10^{-1} s^{-1} (516°C), the fine grains elongate and slip bands (differing in orientation in the different grains) become visible. Figure 4.3-6 provides further quantitative evidence of this effect. Plots of grain intercept distribution for the fine grain (Fig. 4.3-6a) and coarse grain (Fig. 4.3-6b) materials illustrate that during dynamic grain growth (fine grain material), the entire distribution curve (including the median size) shifts to a larger size with an increasing degree of deformation. The reverse is true during dynamic recrystallization (Fig. 4.3-6b).



SC40708

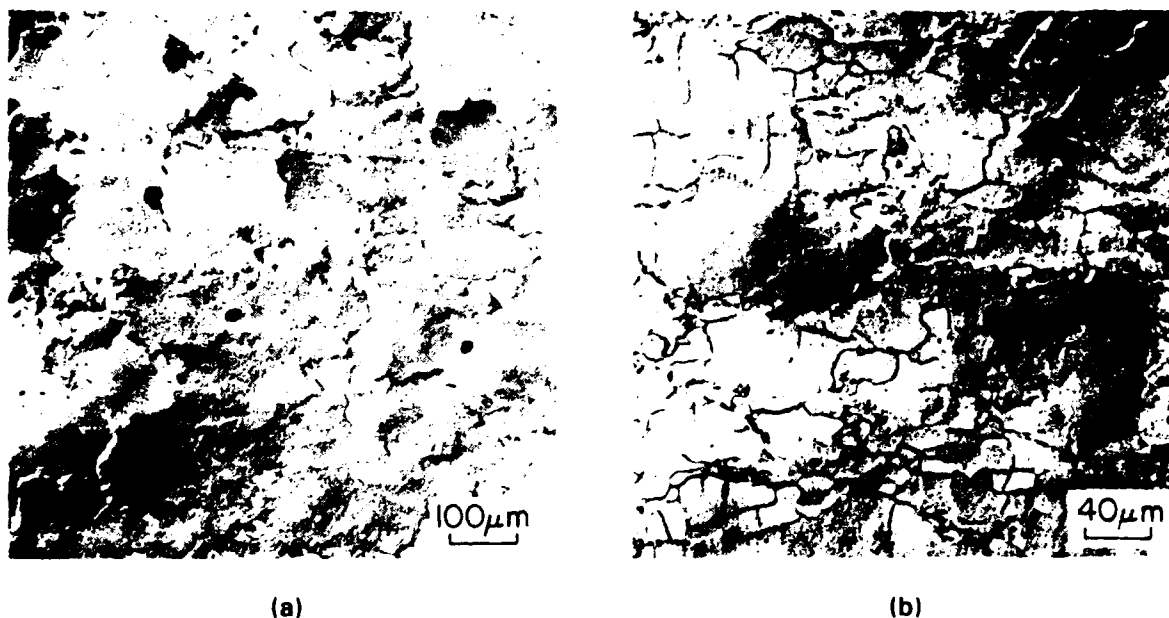


Fig. 4.3-5 Microstructure for coarse grain 7475 Al; (a) zero strain, (b) $\epsilon = 0.55$ at 516°C , $\dot{\epsilon} = 2 \times 10^{-4} \text{ s}^{-1}$.

4.3.1.2 Development of a Mechanistic Model

The space is limited here to discuss the model development work in its entirety. However, a brief summary is presented, and the details may be found in the papers.¹⁵⁻¹⁷ Based on the observations of slip during superplastic flow, the importance of dislocation processes during superplastic flow cannot be ignored. Recently, Arzt, Ashby and Verrall¹⁸ have considered grain boundary sliding occurring through the motion of grain boundary dislocations.

Since diffusional creep is grain-size-dependent and power-law creep is not, the transition from power-law to diffusional creep is a function of the grain size, L , as illustrated schematically in Fig. 4.3-7. While this transition does not occur at a single strain rate, for analytical convenience, power-law creep and diffusional creep are decoupled in this analysis. Thus, if applied strain rate, $\dot{\epsilon} < \dot{\epsilon}^*(L_1)$, grains smaller than L_1 will deform by diffusional creep and those larger by power-law creep. The transition strain rate $\dot{\epsilon}^*(L_1)$ can be calculated as a function of the grain size and the temperature by equating equations for diffusional creep⁸

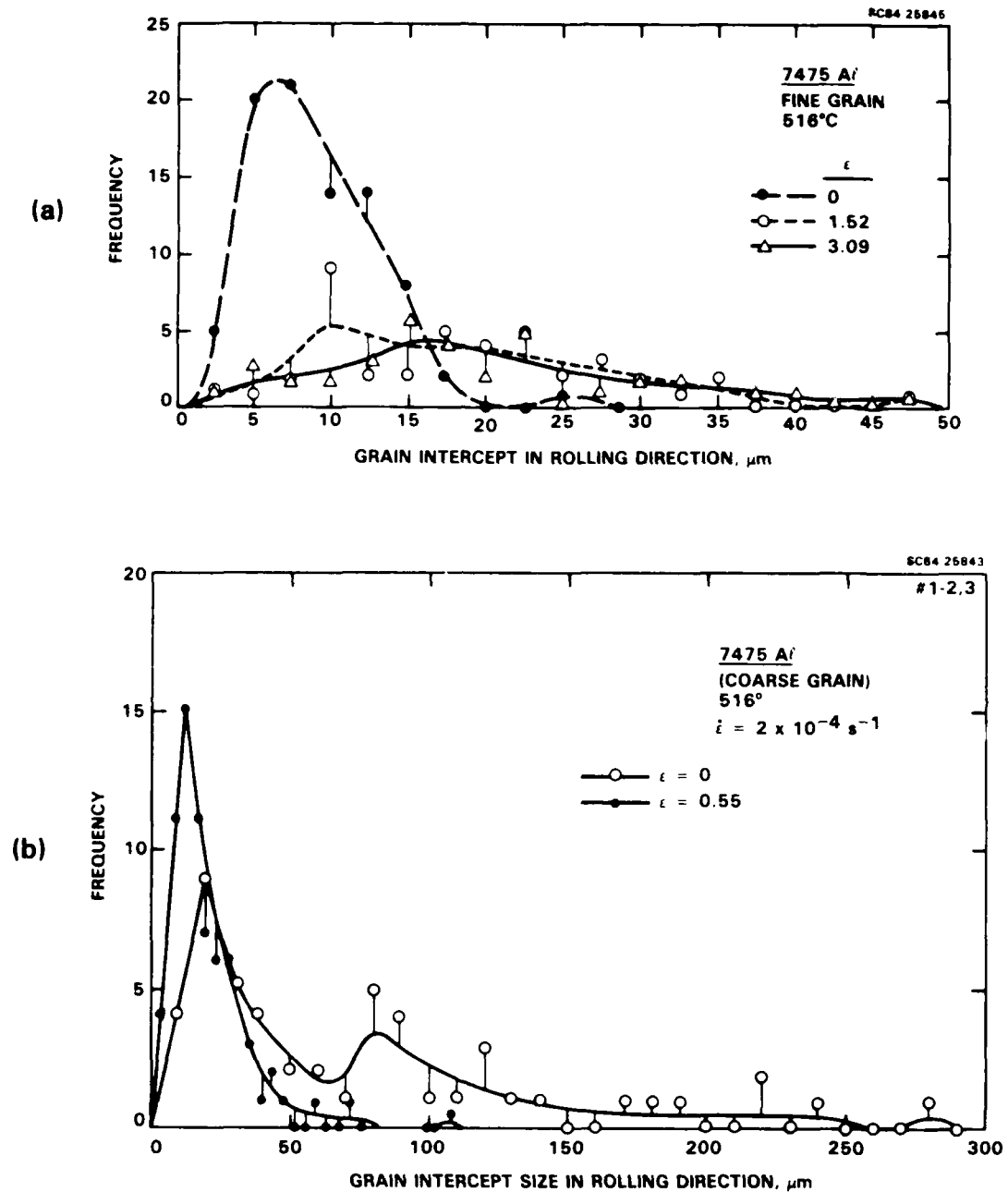


Fig. 4.3-6 Distribution of grain intercept along rolling direction after various strain levels for (a) fine grain and (b) coarse grain 7475 Al.

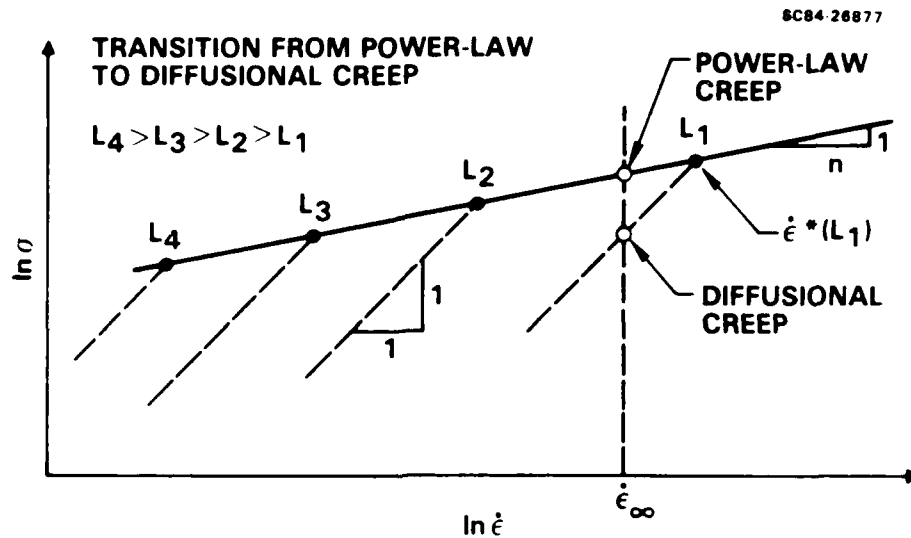


Fig. 4.3-7 The transition from diffusion to power-law creep depends on the grain size. This transition can be characterized in terms of a strain rate $\dot{\epsilon}^*(L)$ which is a function of the grain size L .

$$\dot{\epsilon}_d = 14\pi \frac{\sigma}{G} \frac{G\Omega}{kT} \frac{\delta D_b}{L^3} \quad (1)$$

and power-law creep:¹⁹

$$\dot{\epsilon}_p = A \frac{D_V G b}{kT} \left(\frac{\sigma}{G}\right)^n \quad (2)$$

In Eqs. (1) and (2), σ is the applied (deviatoric or tensile) stress, G is the shear modulus, A is a material constant, Ω is atomic volume, δD_b is the boundary diffusion width times the diffusion coefficient, and D_V is lattice diffusion coefficient.

Equating (1) and (2) and rearranging terms gives the following expression for the transition strain rate $\dot{\epsilon}^*(L)$, shown in Fig. 4.3-7:



$$\dot{\epsilon}^*(L) = \frac{G\Omega}{kT} \cdot (14 \pi \frac{\delta D_b}{L^3})^{\frac{n}{n-1}} (\frac{\Omega}{AD_V b})^{\frac{1}{n-1}} \quad (3)$$

At a constant temperature, the change in $\dot{\epsilon}^*$ with grain size is then given by:

$$\frac{\dot{\epsilon}^*(L_1)}{\dot{\epsilon}^*(L_2)} = (\frac{L_2}{L_1})^{\frac{3n}{n-1}} \quad (4)$$

Thus, a separation of a factor of 5 in grain size, with n being equal to 5, can lead to a spread of a factor of about 400 in strain rate for the transition from power-law to diffusional creep.

Now, we consider dynamic changes in grain size distribution with strain and its effect on the stress-strain curve when the applied strain rate is held constant. A typical experimental set of curves for a fine grained 7475 Al alloy (Al-Zn-Mg-Cu) is shown in Fig. 4.3-8. Especially noteworthy are the gradual changes in the flow stress with strain and the oscillations in the curves at the higher strain rates. These serrations are not an artifact of testing procedure and are usually observed in these alloys within the superplastic temperature range. They disappear at lower temperatures where no strain-induced recrystallization is observed. As shown in Fig. 5, dynamic recrystallization has been seen within the superplastic temperature and strain-rate regime, this effect being more visible when the grain size becomes large. It is believed that power-law creep in the coarse grain material causes accumulation of sufficient density of defects to allow the nucleation of new stress-free grains. In many materials, this process of dynamic recrystallization has shown to start the nucleation of new grains around the existing grain boundaries in a "necklace" form.

An initial log normal distribution in a fine grain material tends to flatten and spread out to larger grain sizes with increasing superplastic strain - a direct result of dynamic grain growth. On the other hand, a bimodal coarse grain distribution sharpens to a large peak of fine grain as newly nucleated grains form - a direct result of dislocation

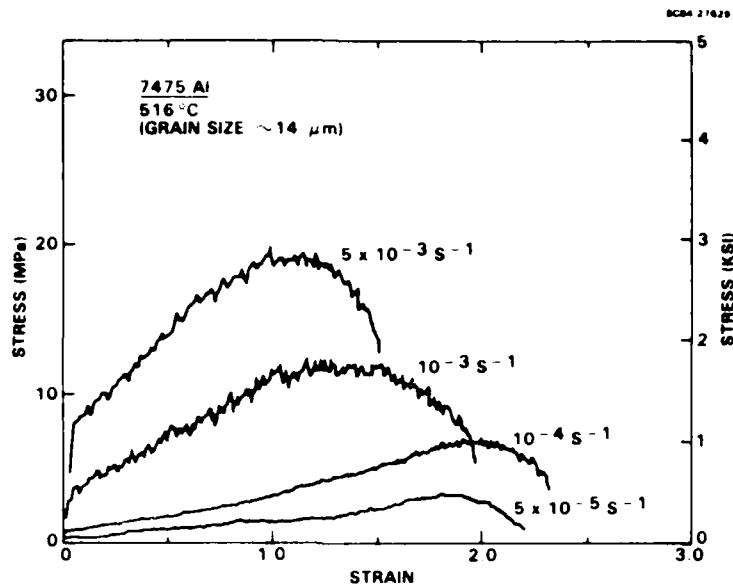


Fig. 4.3-8 Stress-strain curves for superplastic 7475 Al at various strain rates.

accumulation leading to dynamic recrystallization. Similar effects have also been observed for a fixed grain size, but as a function of strain rate. It is now believed that somewhere within the superplastic strain-rate range, a combination of the two processes might occur in such a manner as to not alter the overall average grain size in a significant way.

Normalization of Grain Size, Stress and Strain Rate

To carry out the numerical analysis, the grain size is normalized with respect to L_0 , where L_0 is the size of the new grains which form during dynamic recrystallization of material deforming by dislocation creep.^{8,14} L_0 then becomes the smallest possible grain size in the material. $\dot{\epsilon}_0^*$ is then defined as the highest possible transition strain rate by substituting $L = L_0$ in Eq. (3). The applied strain rates, $\dot{\epsilon}$, will be normalized with respect to $\dot{\epsilon}_0^*$. The flow stress, σ , will be normalized with respect to the flow stress, σ_0^* , at strain rate $\dot{\epsilon}_0^*$.



To simplify the notation even further, we designate $L_0 = 1$, $\dot{\epsilon}_0^* = 1$ and $\sigma_0^* = 1$. This permits us to omit L_0 , $\dot{\epsilon}_0^*$ and σ_0^* in the equations. The actual values of L , $\dot{\epsilon}$ and σ can be readily obtained by multiplying the values for L , $\dot{\epsilon}$ and σ by the actual values for L_0 , $\dot{\epsilon}_0^*$ and σ_0^* . It follows that the equation for power-law creep in Fig. 1 may be written as:

$$\dot{\epsilon} = \sigma^n \quad (5)$$

The equation for the transition strain rate, $\dot{\epsilon}^*(L)$, Eq. (4), then reduces to:

$$\dot{\epsilon}^*(L) = \left(\frac{1}{L}\right)^{3n/(n-1)} \quad (6)$$

and the equation for diffusional creep at grain size, L , then becomes:

$$\frac{\dot{\epsilon}}{\dot{\epsilon}^*(L)} = \frac{\sigma}{\sigma^*(L)} \quad (7)$$

where $\dot{\epsilon}^*(L)$ and $\sigma^*(L)$ satisfy Eq. (5), since the lines for diffusion and power-law creep intersect at that point. Using Eq. (5) to eliminate σ^* from Eq. (7) and further substituting from Eq. (6) for $\dot{\epsilon}^*(L)$, we obtain that:

$$\dot{\epsilon} = \frac{\sigma}{L^3} \quad (8)$$

for diffusional creep.

Thus, the flow behavior of a polycrystal at grain size L at a strain rate $\dot{\epsilon}$ will be governed by Eq. (5) if $\dot{\epsilon} > \dot{\epsilon}^*(L)$, and by Eq. (8) if $\dot{\epsilon} < \dot{\epsilon}^*(L)$, where $\dot{\epsilon}^*(L)$ is given by Eq. (6). In a polycrystal with a mixed grain size, different regions may deform by different mechanisms, but the strain rate throughout will be assumed to be equal to the applied strain rate.



Strain-Induced Grain Refinement During Dislocation Creep

In a polycrystal with a distributed grain size, the large grains are likely to deform by power-law creep. Dynamic recrystallization will produce a necklace of new small grains at the grain boundaries of these large grains. The volume of the new grains expressed as a fraction, q , of the volume of the large grains will increase with strain. q can be expected to be related to dislocation creep strain, ϵ , by a sigmoidal curve, typical of nucleation and growth phenomena. We assume that the sigmoidal behavior may be expressed by the following functional form:

$$\tan \left\{ \pi \left(\frac{1}{2} - q \right) \right\} = b \left(1 - \frac{\epsilon}{\epsilon_c} \right) \quad (9)$$

where ϵ_c is the critical strain for nucleation, and b is a constant which controls the sharpness of the inflexion. Plots of Eq. (9) for $b = 5$ and 10 are shown in Fig. 4.3-9a. The use of Eq. (9), which is plotted in Fig. 4.3-9a, allows for a broad distribution function rather than a step function for nucleation, as shown schematically in Fig. 4.3-9b. The difference between them can also be appreciated by considering the derivative of the curves, which will be the nucleation frequency. In Fig. 4.3-9a, bell-shaped curves with a peak in nucleation frequency at $\epsilon = \epsilon_c$ will be obtained, while in Fig. 4.3-9b the result would be a delta function located at $\epsilon = \epsilon_c$.

In the numerical analysis that follows, the size of the grains which have suffered dynamic recrystallization is decreased by an amount consistent with the volume fraction which has recrystallized. Therefore, if a volume fraction q of grains of size L_1 has recrystallized, then the grain size of the remaining unrecrystallized material, L_2 , will be given by $(L_2/L_1) = \sqrt{1-q}$, where the grain size is assumed to be defined by a two-dimensional cross section of the polycrystal.

Strain-Induced Grain Growth During Diffusional Creep

Grain growth in otherwise stable, fine grain superplastic alloys subjected to low stresses is a phenomenon of considerable recent interest. A mechanism is proposed here in which grain growth appears as a natural consequence of accommodation for the grain boundary sliding process. The following assumptions have been made to arrive at the proposed model:

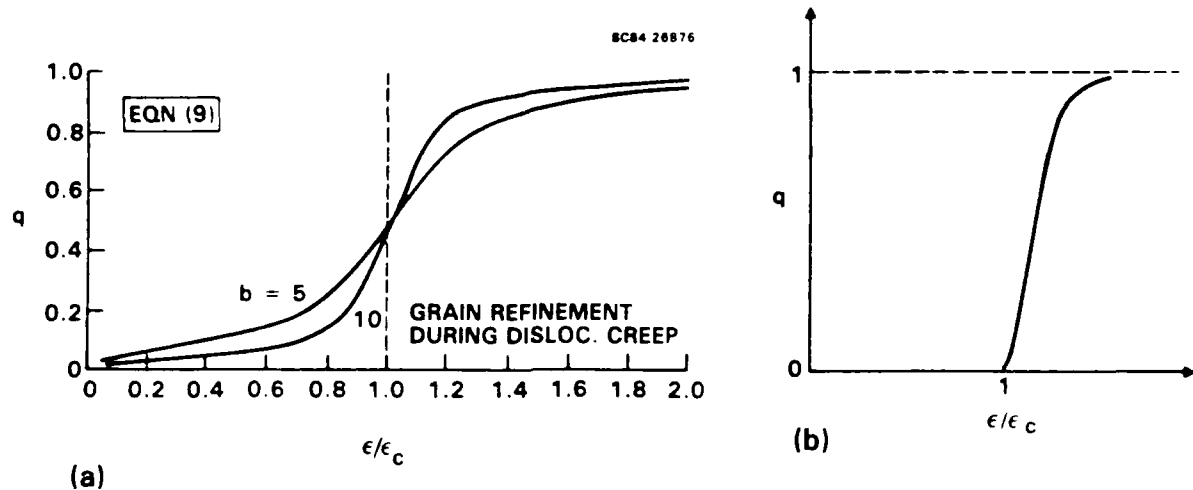


Fig. 4.3-9

Strain-induced grain refinement function assumed during dislocation creep. q is the volume fraction of the original material which is recrystallized, and ϵ_c is a pseudo-nucleation strain. A gradual transition in (a) might be justified on the basis that the nucleation strains may have a distribution of values. An alternative is a single value as illustrated in (b).

1. Grains are assumed as rigid blocks with a thin viscous region at the boundaries. This region is weak in shear so sliding is easy, however, it is stronger in tension so greater stress is required to separate the boundaries.
2. Surface diffusion is rapid and tends to maintain near-equilibrium dihedral angles.
3. Accommodation to sliding process is by diffusion near the grain boundary which is rapid enough so that any tendency for void formation is counteracted by rapid matter transport into those regions.

AD-A182 159

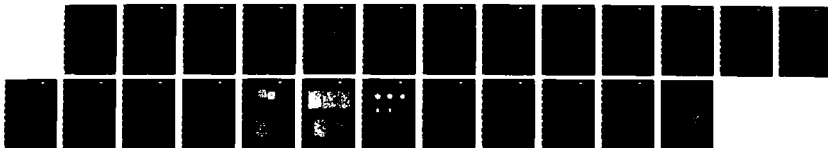
PROCESSING AND PROPERTIES OF AIRFRAME MATERIALS(U)
ROCKWELL INTERNATIONAL THOUSAND OAKS CA SCIENCE CENTER
C G RHODES ET AL JUN 87 SC5358-4FR AFOSR-TR-87-0815
F49620-83-C-0055

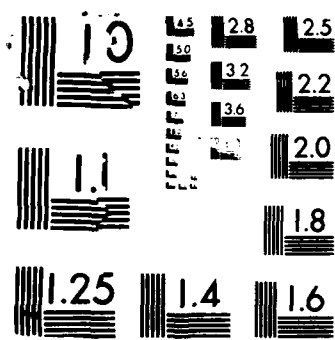
2/2

UNCLASSIFIED

F/G 1/3

NL







Now, let us consider the illustration in Fig. 4.3-10, in which the triple-point region is being examined at a very high magnification. If the applied shear stresses are such that grain (1) feels a traction \hat{T} as shown, and grains (2) and (3) feel the same traction in the opposite direction (Fig. 4.3-10a), then a relative translation (or shear strain) could begin if groups of grains above (1) cooperate with (1) and those below (2) and (3) cooperate with (2) and (3). Since no relative displacement occurs between grains (2) and (3), they are assumed to be fixed, while sliding occurring between grains (1) and (2) is described only by the motion of grain (1) relative to grain (1).

As a result of this traction on grain (1), a step may form in the vicinity of point A in grain (1), while at point B, the grains (1) and (3) are firmly attached. The approach toward equilibrium dihedral angles would therefore cause a change in the curvature of this boundary, as shown in Fig. 4.3-10b. While this configuration cannot exist without the process shown in Fig. 4.3-10c operating, this imaginary step provides a rationale for the changes which can occur. The boundary configuration of Fig. 10b is resisted by the need to minimize grain boundary surface area tending to round off grain corners C and A'. Furthermore, grain (3) conforms closely to point B due to surface tension forces. Now, the boundary curvatures in grains (1) and (2) drive their boundaries to cause migration in the directions shown in Fig. 4.3-10c with concurrent matter transport into grain (3). This causes bulging of grain (3) into the corner in an effort to counteract cavitation. If this process continues with simultaneous accommodation, boundary migration leads to the growth of grain (3) at the expense of grains (1) and (2). This matter transport, driven either by surface tension forces or by dislocation density from power-law creep accommodation, is believed to be the key for the strain-induced grain growth mechanism. In this process, the sliding grain loses volume by allowing the growth of the static grain.

Since the boundary migration distance is proportional to the sliding distance (or the step) and diffusional creep models preach the proportionality between sliding strain and diffusional creep strain, it is expected that grain size increase will also be proportional to diffusional creep strain.

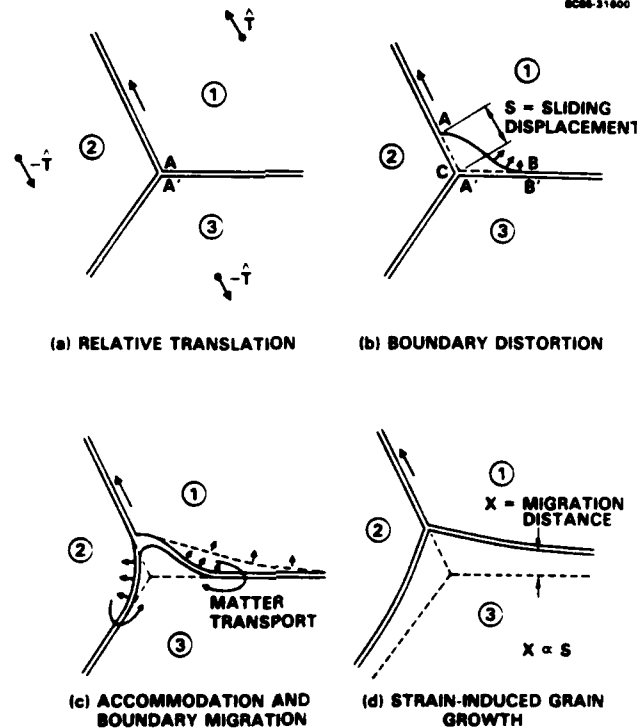


Fig. 4.3-10 Possible mechanism of strain-induced grain growth during superplastic flow.

Wilkinson and C'Aceres²⁰ have correlated grain size to strain and the strain rate during superplastic deformation in several materials, and found that the correlation is nearly linear and approaches a value which is independent of the strain rate at very slow strain rates. Accordingly, we assume that:

$$\frac{dL}{d\epsilon} = a \quad (10)$$

where ϵ refers to diffusion creep strain. In the numerical analysis, we will show that the general features of the stress-strain curves are not influenced by the magnitude of the parameter a .

The details of the numerical analysis are given in Ref. 21. However, a brief synopsis is presented here. First, the initial grain size distribution (v_i, L_i) is specified, where v_i is the volume fraction for a particular grain size, L_i . The constants b , ϵ_c and a , and the power-law stress exponent n are specified, and next the applied strain rate, $\dot{\epsilon}$, is input. The flow stress is calculated using the procedure described in Ref. 11, except for



the simplifying assumption that the stress supported by a region of a certain grain size, at a given strain rate, is given by dislocation creep equation, Eq. (5), if $\dot{\epsilon} > \dot{\epsilon}^*(L)$, and by the diffusion creep equation, Eq. (8), if $\dot{\epsilon} < \dot{\epsilon}^*(L)$. This decoupling assumption gives rise to an error which will be refined in a later paper. The total applied stress is then obtained through the equation $\sigma = \sum \sigma_i v_i$ which enforces equilibrium. The applied incremental strain, $\Delta \epsilon$, is counted as diffusional strain or dislocation strain for each region, v_i , depending on whether a given v_i is deforming by diffusional creep or by dislocation creep. Equations (10) or (9), respectively, are then used to update the grain size distribution. Before repeating the calculation for a new increment of strain, a check is done that $\sum v_j = 1$, where j is the suffix for the new grain size distribution.

The results for the stress-strain curves and the grain size distributions which develop as a result of the applied strain are shown in Figs. 4.3-11 and 4.3-12. The initial grain size distribution for these calculations is given in the top picture in Fig. 4.3-11, drawn in solid bars. The material constants were assumed to be $n = 5$, $a = 2.5$, $b = 5$ and $\epsilon_c = 4$. The following observations are interesting:

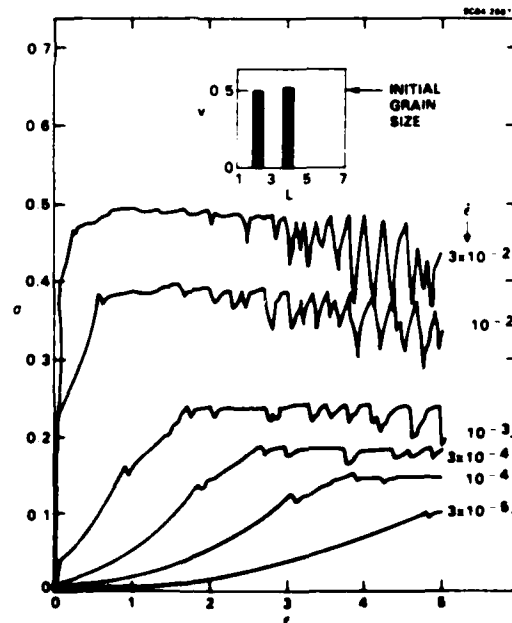


Fig. 4.3-11

The computed stress-strain behavior at various strain rates for a bimodal initial grain size. $a = 2.5$, $b = 5$ and $\epsilon_c = 4$. σ is normalized with respect to σ_0^* and ϵ is normalized with respect to ϵ_0^* .

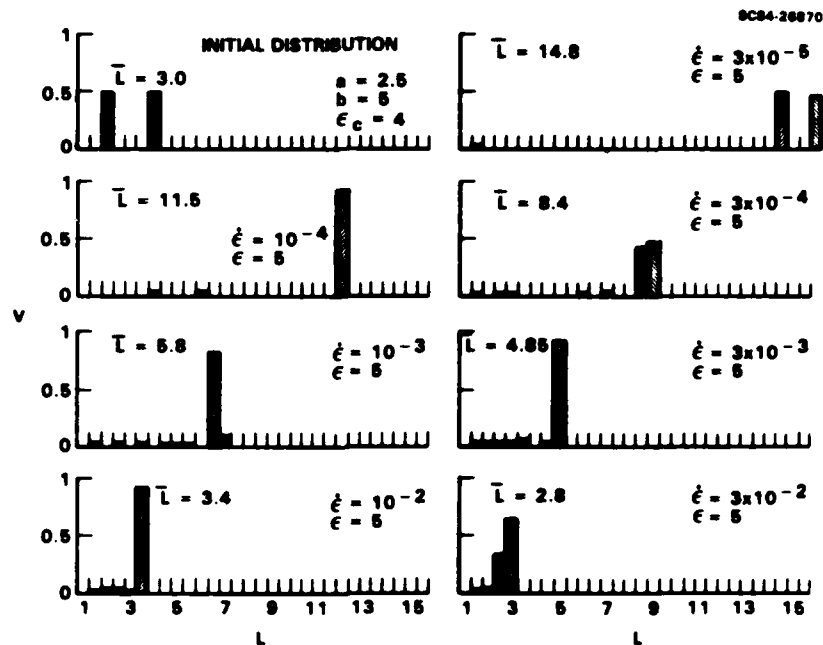


Fig. 4.3-12 Initial and final grain size distributions obtained for the stress-strain curves in Fig. 4.3-11.

1. The stress-strain curves show three stages of behavior (see Fig. 4.3-11). At small strains, there is a period of hardening (Stage I), which is followed by saturation stress (Stage II). In Stage III, the flow stress fluctuates with strain.
2. As shown in Fig. 4.3-11, at $\dot{\epsilon} = 10^{-2}$, all three stages of behavior are apparent. At slower strain rates, the hardening appears to be more prominent, while at the higher strain rates, the oscillatory behavior appears to dominate.
3. The stress amplitude of the oscillatory behavior increases as the strain increases. The period of the oscillations (in strain) appears to decrease as the strain rate increases.



4. The change in the grain size distribution after a strain of $\epsilon = 5$ at various strain rates is shown in Fig. 4.3-12. Although the initial grain size is bimodal, the distribution that develops subsequently is continuous. The average grain size decreases with increasing strain rate.

The influence of initial grain size distribution on the stress-strain curves and the development of grain size distribution with superplastic strain as predicted by the model agree well with experimental trends (given in Ref. 21), but will not be covered here due to limited space.

4.3.2 Progress in Superplastic Cavitation

In Ref. 4, a model for superplastic cavitation was put forth which incorporates both cavity nucleation and cavity growth considerations. Based on prior work of Dyson, cavity nucleation was deemed to be influenced by diffusional effects and rates were proportional to stress. Surface energy arguments also give the following relationship for a stable nucleating void:

$$\sigma - p \geq 2(\sigma_s - \sigma_p)/r \quad , \quad (11)$$

where σ is applied stress, p is superimposed hydrostatic pressure, σ_s is the surface energy of newly created void surface, σ_p is the surface energy of prior particle surface, and r is the radius of particle or stable void growing from it.

It was shown in Ref. 4 that growth of voids can occur primarily by a plastic flow process; however, because of increasing flow stress due to concurrent grain growth, the rate of void growth can continue to increase with increasing strain. Furthermore, the criterion for nucleation, Eq. (11), can be satisfied at yet smaller particles with increasing strain, thereby leading to a continuous void nucleation process.

Controversy does exist, however, on whether superimposed hydrostatic pressure can suppress cavity nucleation or cavity growth, or both. To address this issue, two critical experiments were performed with fine grain 7475 Al alloy, which will be



described below. Before this, test samples were strained at $2 \times 10^{-4} \text{ s}^{-1}$ and 516°C (optimum conditions) under ambient pressure levels. Samples were sectioned and used for measurements of density by a sink-float technique, as commonly carried out for overall void volume measurement. The density change values were calculated and used for signifying overall void volume. These are plotted as functions of strain as the baseline data in Figs. 4.3-13 and 1, curve 1.

In the first experiment, a sample was tested under the same test conditions, but with a superimposed hydrostatic pressure of 600 psi (sufficient to prevent all cavitation) up to a strain level of 1.0, followed by testing under ambient pressure. This curve is shown in Fig. 4.3-13 by curve 2. Also shown is a dashed curve which is parallel to curve 1, but starting at a strain of 1.0 to indicate that no cavities were present up to this point. Since curve 2 represents various strain levels from the same specimen, locations in the specimen accumulating a certain strain level during the first step can undergo higher levels of strain without hydrostatic pressure during the second step. Thus, the arrows qualitatively show how cavitation would increase in going from the first deformation step to the second - an effect strongly due to cavity growth upon release of hydrostatic pressure.

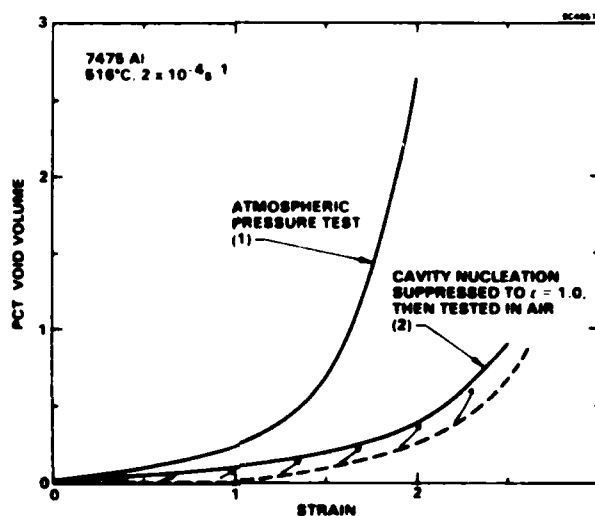


Fig. 4.3-13 Superplastic cavitation under two test conditions: (1) without hydrostatic pressure; and (2) with 600 psi pressure to a strain of 1.0, then no hydrostatic pressure.



In a second experiment, a sample was tested first under ambient pressure conditions up to a total strain of 1.0, followed by testing under superimposed hydrostatic pressure to failure. Figure 4.3-14 shows these data by curve 3, and arrows here indicate how cavities prenucleated (without any hydrostatic pressure) could undergo shrinkage first and subsequently small amounts of growth as the level of strain increases significantly. This ability for void shrinkage suggests that even if small preexisting voids remain in a fine grain processed sheet material, they will not form stable void nuclei as long as sufficient hydrostatic pressure is maintained on the sample. Thus, hydrostatic pressure can influence void nucleation and growth processes. These are not incorporated into the model given in Ref. 4 for a unified model of superplastic cavitation.²²

4.3.3 Progress in the Understanding of Consolidation of Al Alloy Powder

Consolidation of powder metals is routinely achieved by unidirectional hot pressing and hot isostatic pressing (HIP) operations. For structural metallic alloys, typically the compact is extruded or forged for developing full density and improved powder

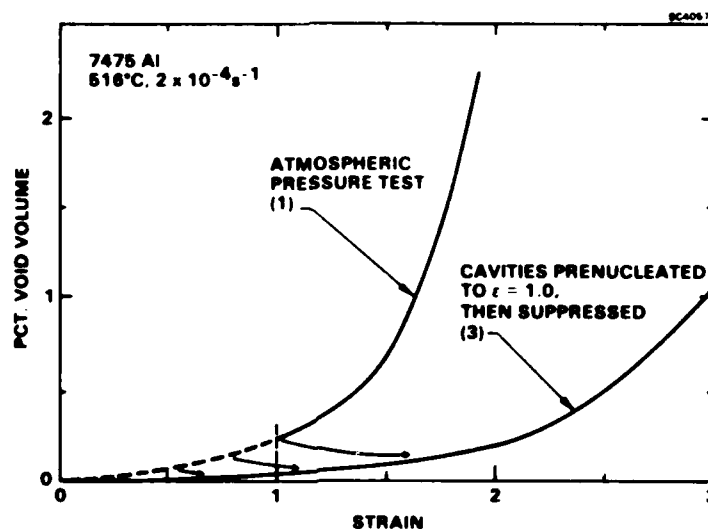


Fig. 4.3-14 Superplastic cavitation under two test conditions: (1) without pressure; and (3) without pressure up to $\epsilon = 1.0$, then with 600 psi pressure to failure.



surface deformation and bonding. For Al alloy powder, deformation is a key to breaking up of surface oxides and achieving superior mechanical properties. Therefore, consolidation and extrusion are typically done at temperatures in the range of 350-400°C, where surface diffusion effects are negligible, and the material can undergo large amounts of internal plastic flow. Since the presence of pores and voids in minor quantities can influence their mechanical behavior, the subject of void closure (or void elimination) during consolidation process is an important one to examine. Prior work along this direction have been performed by Budiansky et al²³ and Lenyi.²⁴ However, no specific attempt was made to represent the various deformation conditions for comparisons with experiments on metal powder.

The objective of this work is to study the void elimination process during deformation processing of a powder mass under a variety of process conditions. The first of these is hot pressing or unidirectional consolidation in a die. The second one is uniaxial compression without a die, i.e., without any lateral constraints, and the third situation is similar to isostatic pressing, except that surface compressive strains, not surface-applied pressures are maintained equal. Our approach has been to develop an understanding of the void elimination process through consideration of local states of stress within the solid. To develop this understanding, three different approaches have been pursued. The first one involves the development of an analytic formulation of void collapse process. The second one involves experimental consolidation of high-strength RSP 7075 Al powder, and the third one involves the collapse of premachined void in a 7475 Al. The following section summarizes the progress in each of these areas:

4.3.3.1 Analytic Formulation of Void Collapse

Figure 4.3-15 illustrates the three stress states for the void collapse problem studied. The uniaxial compression case is typically applied to partially consolidated powder without later constraints. The other two could be applied to either partially consolidated material or tapped powder. The constrained die compression is typically used for hot pressing of powders and uses total lateral constraint. As previously mentioned, the isostatic compression case as shown in Fig. 15 is not followed in an exact sense, but through surface displacements. The variable used to describe these three cases is the ratio of circumferential to axial strain ($\epsilon_\theta/\epsilon_z$) which is -1/2, 0 and 1, respectively.



8C35008

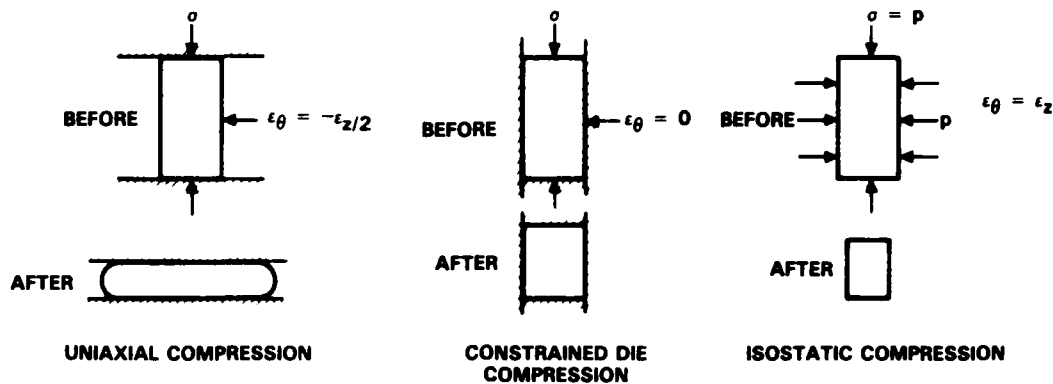


Fig. 4.3-15 Strain states in various powder compaction processes.

While individual voids in actual powder mass are created at the powder interstices and therefore typically contains convex inward boundaries, after some amount of preconsolidation the void shape is no longer the same. It is for starting at this stage that the present analysis is developed. Furthermore, the object of the present work is to examine the deformation consolidation process and not the effect of sintering or diffusion. For this reason, the void shape is not likely to be as important a factor in the consolidation process as the overall void density. Thus, a simple spherical geometry is assigned to starting voids for this analysis. Other void geometries may be examined in the future.

Figure 4.3-16a shows a representative volume element (cylindrical geometry) containing a single spherical void at its center. The partially consolidated powder mass may be assumed to be composed of many such volume elements arranged next to each other. In carrying out slab deformation analysis, the material surrounding the void could be divided into many horizontal slices (as shown), and each horizontal section is then divided in the vertical direction into many radial elements as shown. Thus, each horizontal slice is bounded by x_i and y_i and the radial distance r_j to any vertical slice lies between the inner radius x_i and the outer radius y_i . The initial values for y_i is R and x_i is a .

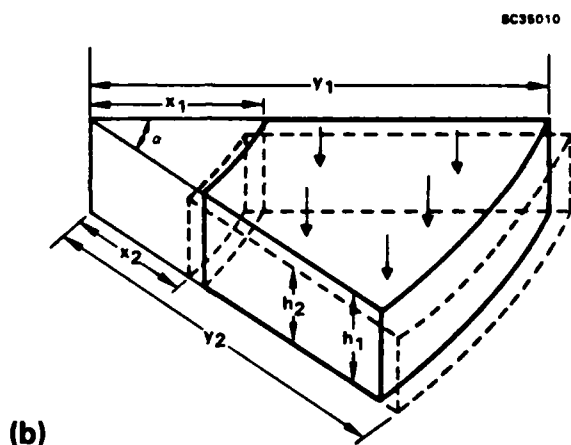
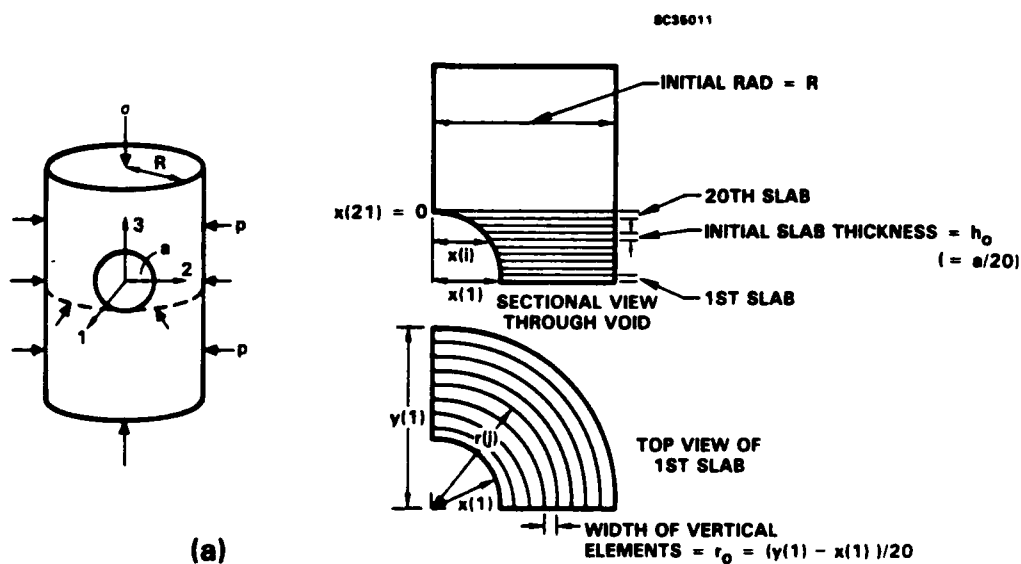


Fig. 4.3-16 (a) Representative volume element showing spherical void for analysis;
(b) a section of a horizontal slab for analysis.

The basic definitions of strain used in this calculation

circumferential strain, $d\epsilon_{\theta} = dr/r$

height strain, $d\epsilon_z = dz/z$

radial strain, $d\epsilon_r = -(d\epsilon_z + d\epsilon_{\theta}) = -(1 + \rho)d\epsilon_z$

(12)



where strain ratio $\rho = d\epsilon_\theta/d\epsilon_z$. ρ is $-1/2$ at the void surface for uniaxial state of stress and changes to 0 or 1 at the outer surface for constrained compression and isostatic compression respectively. Fig. 4.3-16b shows a pie-shaped horizontal slab section joining the void and the outer wall of the cylindrical cell under compressive deformation. This section is shown by solid outline in Fig. 4.3-16b, while the geometry after deformation is shown by dashed line. The strain in the z direction, ϵ_z , is assumed to be constant in each slice. Assuming the section shown in Fig. 4.3-16b to represent each radial section of the slab, volume constancy of this section provides

$$\alpha(y_1^2 - x_1^2) h_1 = \alpha(y_2^2 - x_2^2) h_2 \quad (13)$$

$$\text{or, } h_2/h_1 = (y_1^2 - x_1^2)/(y_2^2 - x_2^2)$$

when applied to incremental deformation, $h_2/h_1 = 1 + d\epsilon_z$. Further, since $y_2/y_1 = 1 + d\epsilon_\theta$, $y_2 = (1 + \rho d\epsilon_z)y_1$. Incorporating these relations in Eq. (13), we obtain after some algebra,

$$d\epsilon_\theta|_{x_1} = \sqrt{((y_1/x_1)^2 (2\rho+1) - 1) d\epsilon_z} - 1 \quad (14)$$

which can be approximated to

$$\rho_{x_1} = 1/2 ((y_1/x_1)^2 (2\rho_0 + 1) - 1) \quad (15)$$

This relationship provides a means of determining the strain ratio ρ_0 at location x_1 , if ρ is known at location y_1 . Thus, one can assign a ρ on the outer extremity of the cylindrical volume element and continue to calculate ρ in all internal elements of the material.



The analytical scheme is started by assigning a $\dot{\epsilon}_z$ at the bottom slab (i.e., center plane). After determining the strain ratio ρ , the stress ratio (α) is found from the associated flow rule:

$$\alpha = (1 + 2\rho)/(2 + \rho) = \sigma_\theta/\sigma \quad (16)$$

The effective strain rate is obtained from von Mises relation which can be rewritten as

$$\dot{\bar{\epsilon}} = \frac{2}{\sqrt{3}} (1 + \rho + \rho^2)^{1/2} \dot{\epsilon}_z \quad (17)$$

This can be plugged into the constitutive equation: $\dot{\bar{\epsilon}} = A\bar{\sigma} + k\bar{\sigma}^n$ to determine the effective stress, $\bar{\sigma}$. From this and von Mises effective stress relation: $\bar{\sigma} = (1 - \alpha + \alpha^2)^{1/2} \sigma_z$, the individual σ_z and σ_θ can now be obtained. In the event there is an external pressure p , at $y_1 = y(l)$, the effect of this in all internal elements may be calculated from the incremental equation

$$p_{j+1} = p_j + \sigma_\theta \ln(r_{j+1}/r_j) \quad (18)$$

which would be added onto the previous σ_z and σ_θ to obtain their actual values. The load in the z direction can then be found by elemental integration of (2π term be omitted for simplicity)

$$L = \int_{x_1}^{y_1} \sigma_z r dr \quad (19)$$

In carrying out the calculations on the slabs above the bottom one, $\dot{\epsilon}_z$ is varied to until equilibrium with the same vertical load is satisfied. In this manner, the deformation in all elements is determined and the current extremities of the void are calculated.

Figure 4.3-17 shows the progression of void collapse for three states of stress: uniaxial compression; constrained compression; and isostatic compression. For uniaxial compression, a circular cross section changes to ellipsoidal sections with increasing strain in the z -direction. Starting with an initial void volume of 0.2, at a

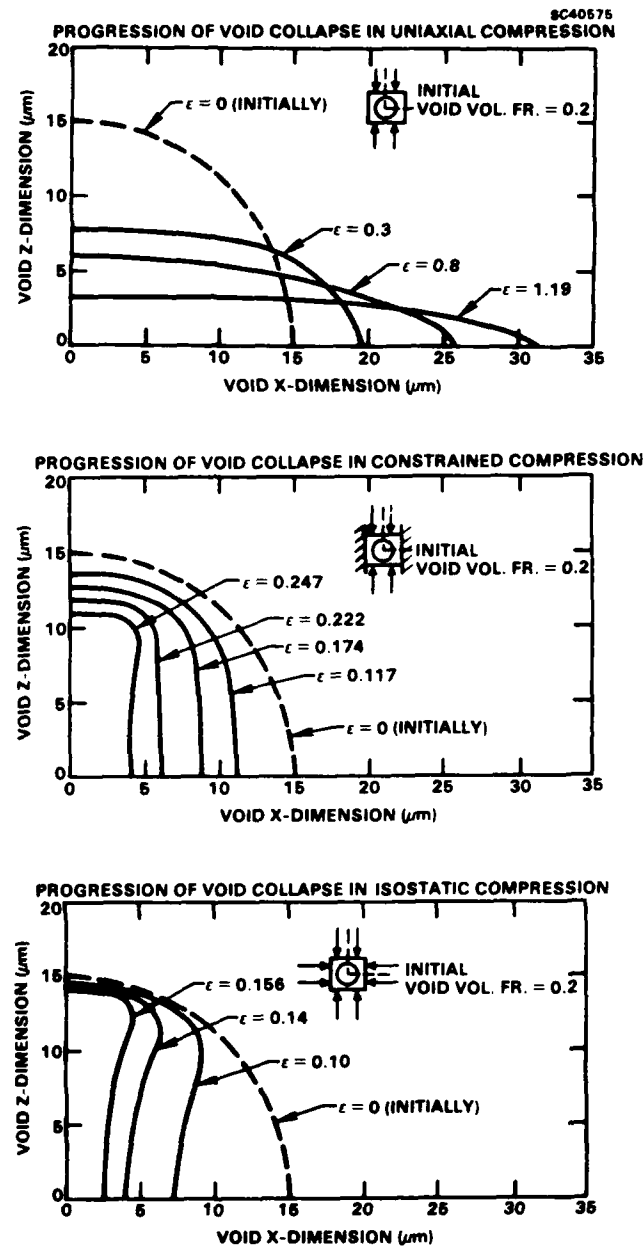


Fig. 4.3-17 Progressive closure of a spherical void under different states of deformation.



strain of 1.19, the void is considerably large in x and y-direction; however, it is far from complete collapse. With both constrained compression and isostatic compression, the void shrinks more in x- and y-directions, but less along the z-direction. Isostatic condition provides the most efficient void collapse per unit strain; however, the surface area of the void continues to decrease during these types of deformation. Figure 4.3-18a and b summarizes void collapse and void area change for the three deformation modes. An interesting aspect of the isostatic consolidation is shown in Fig. 4.3-17 where the collapse of a longer void appears to lead toward its breakup into smaller voids, which then would go through a similar process of consolidation. As discussed before, the uniaxial compression process produces the least void collapse; however, as shown in Fig. 4.3-18b, the overall void shows a significant reduction in surface area with void shrinkage. A small region near the void tip, however, does undergo considerable stretching. This is important for Al alloy powder since the breakup of surface oxide is important in achieving a good quality P/M alloy.

In spite of this benefit, however, uniaxial compression is not a suitable means of consolidation since excessive shape change has to occur for the small extent of consolidation achieved. A preferred process window may therefore be compression with partial constraints, as shown in Fig. 4.3-18a. This may be done by encasing the powder mass in a thick-walled container (made of a material which is somewhat stronger than the powder alloy and possessing sufficiently high ductility) and subjecting it to unidirectional compression. The flow maintains a high lateral constraint yet allowing significant shear to occur. An alternate approach is to use a two-step process: first, a fully constrained compression step (e.g., hot pressing) to achieve 80-90% theoretical density and then uniaxial compression to cause shear flow and enhanced particle bonding. The second step may be replaced by extrusion when this is convenient.

4.3.3.2 Consolidation of 7075 Al Powder

To examine the concepts forwarded in the previous section, controlled experiments were conducted with 7075 Al powder produced by inert gas atomization. The powder was -325 mesh in size and first consolidated in a graphite die by hot pressing (total lateral constraint) at 460°C which is well below the solidus temperature of the alloy

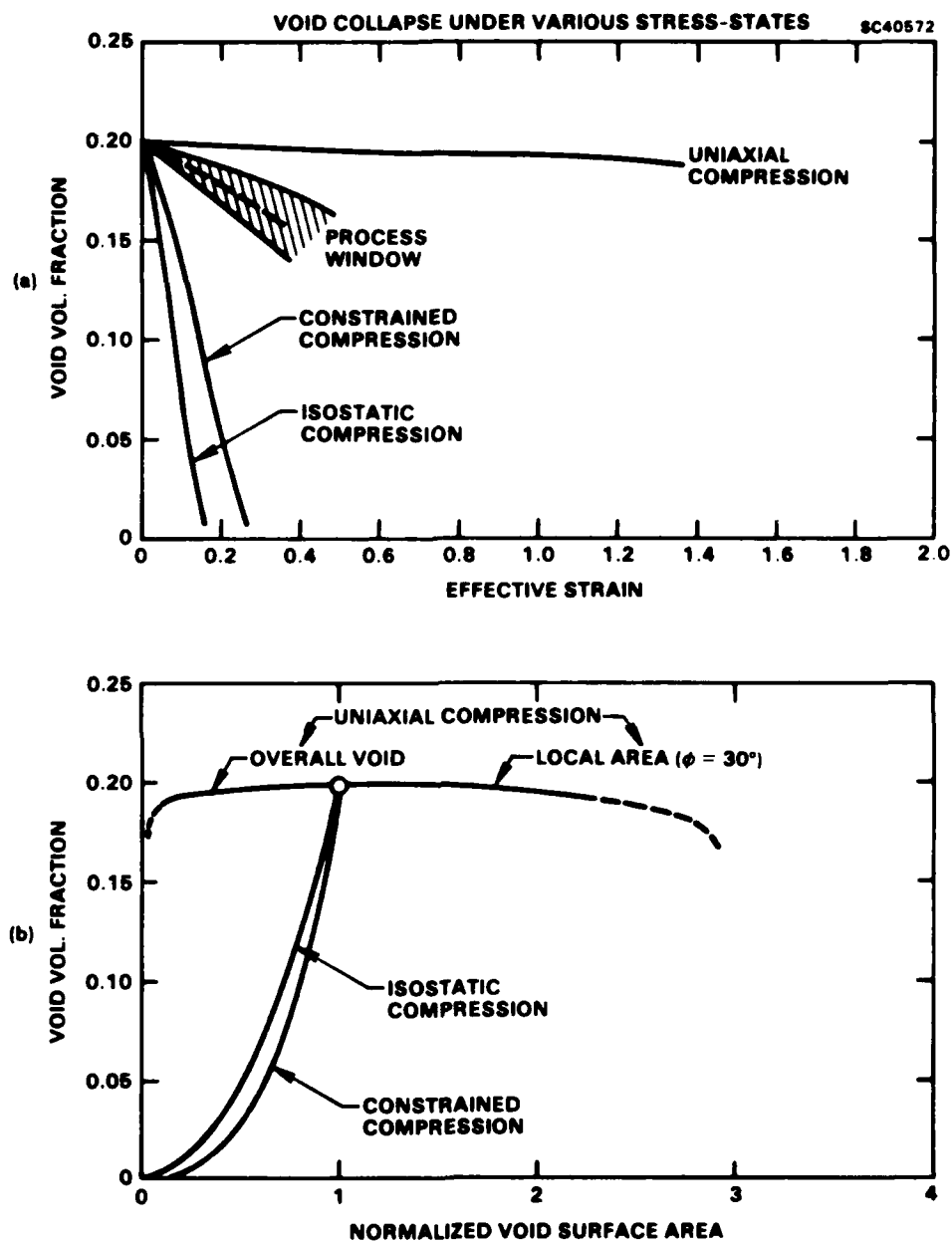


Fig. 4.3-18

Void closure under different states as functions of compressive strain and void surface area.



(~ 500°C). The first consolidation was made to a level of 35% porosity; subsequently, compression samples were machined and further compressed to a variety of reductions. From the consolidated compacts, metallographic sections were made and examined by using quantitative microscopy techniques. Figure 4.3-19 shows the microstructure and progressive void collapse in these compacts. The first part of this was done under constrained compression showing a more rapid collapse, and the latter part under uniaxial compression exhibiting a more gradual collapse, as analytically predicted.

Figures 4.3-20 and 4.3-21 compare the extent of compaction at two different temperatures (460°C and 482°C) for a relatively slow strain rate (crosshead speed = 0.02 in./min). At a strain of 1.39, the lower temperature shows greater deformation of individual powder particles as expected from a greater contribution of dislocation creep. However, the evidence of large flow along the particle boundary regions becomes evident at a much higher strain (2.12) at the higher temperature. It also appears that new grains might have nucleated deformed in these areas. Figure 4.3-22 provides a comparison for a higher strain rate compaction. It is seen that dynamic recrystallization can now set in at much lower strain level (0.69), leading to small grain necklace formation as well as large grain breakup. In comparison to the free edge of the compact, the center region shows large shear deformation of the powder particles and the newly formed grains. Thus it is the combination of hydrostatic compression and shear flow present near the center which is beneficial in particle surface flow and oxide breakup. Extrusion process provides such a state of deformation, and is therefore a highly preferred method of consolidation.

4.3.3.3 Collapse of Spherical Machined Void

This study was conducted to verify the analytical predictions of void collapse under constrained compression. Two cylindrical samples with half spherical voids were machined from 7475 Al and placed (on top of one another) with the half-voids facing. This assembly was deformed in a cylindrical steel die providing total lateral constraint during compression. Incremental tests were conducted with different samples whose cross sections are shown in Fig. 4.3-23. The shape change with strain agrees quite well with analytical predictions presented earlier. The collapse from the sides of the void



SC5358.4FR

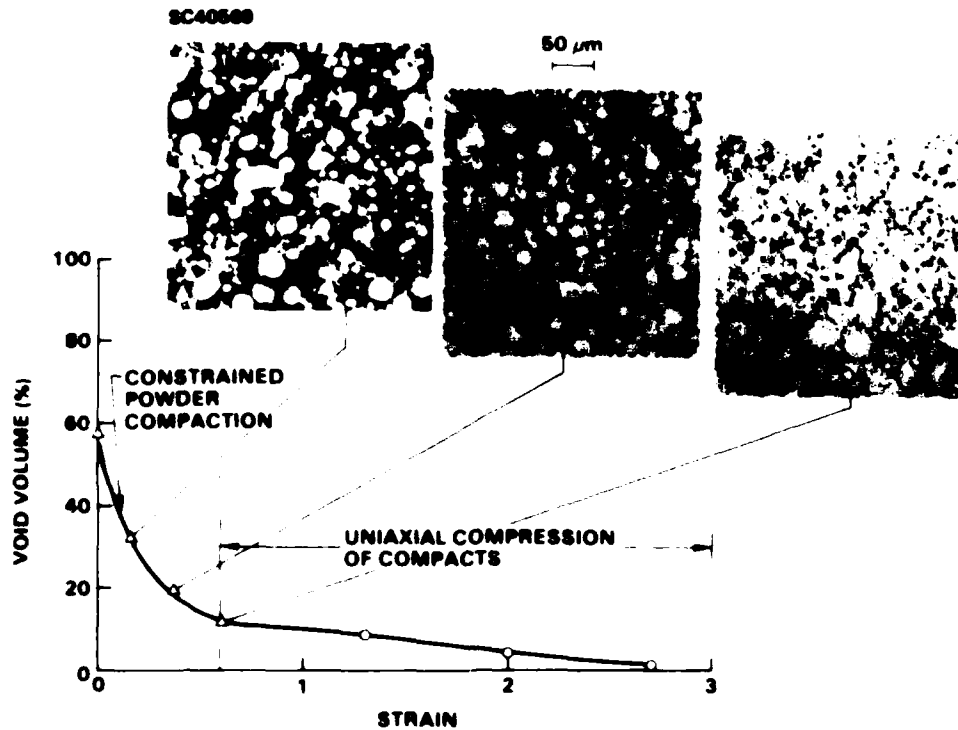


Fig. 4.3-19 Void closure in 7075 Al powder, first undergoing hot pressing, then pure compression.

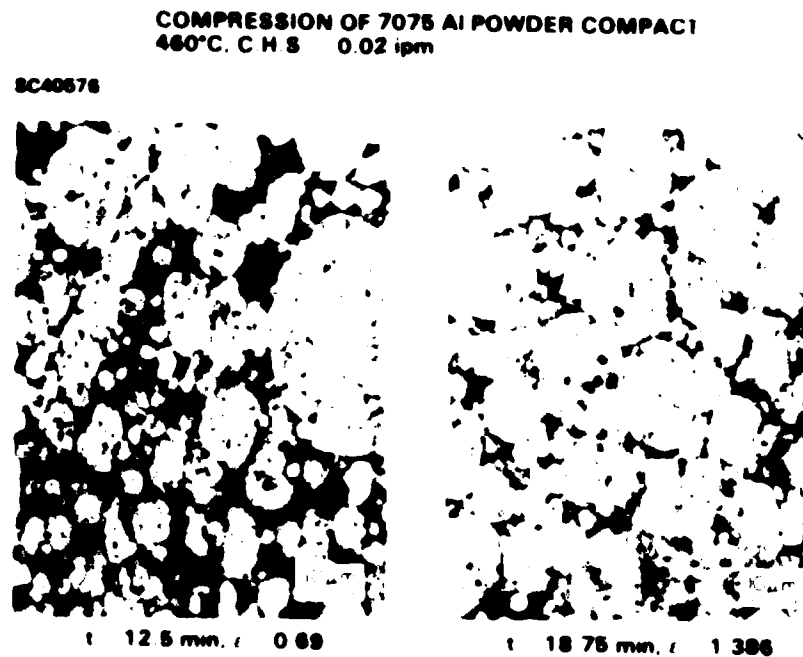


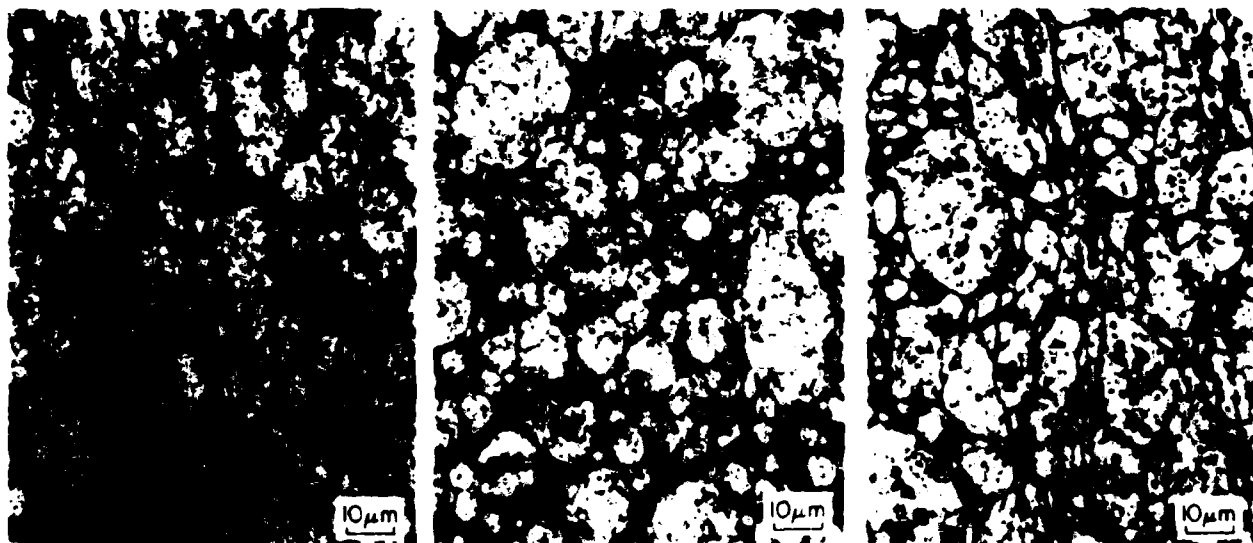
Fig. 4.3-20 Micrographs of 7075 Al powder compact at two stages of consolidation (460°C).



SC5358.4FR

COMPRESSION OF 7075 Al POWDER COMPACTS
482°C, C.H.S. = 0.02 ipm

SC40568



$t = 12.5 \text{ min}, \epsilon = 0.69$

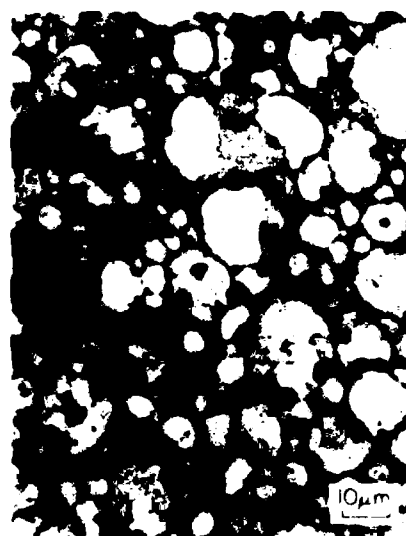
$t = 18.75 \text{ min}, \epsilon = 1.386$

$t = 22 \text{ min}, \epsilon = 2.12$

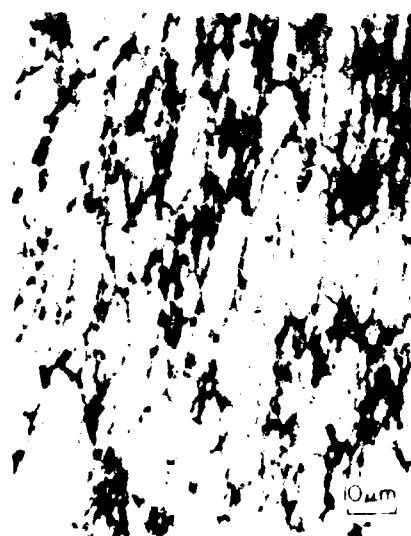
Fig. 4.3-21 Micrographs of 7075 Al powder compact at three stages of consolidation (482°C).

COMPRESSION OF 7075 Al POWDER COMPACT
460°C, C.H.S. = 2 ipm, $t = 7.5 \text{ sec}$
 $\epsilon = 0.69$

SC40570



EDGE



CENTER

Fig. 4.3-22 High rate compaction of 7075 Al powder showing dynamic recrystallization effects and particle flow.



SC5358.4FR

SC40671

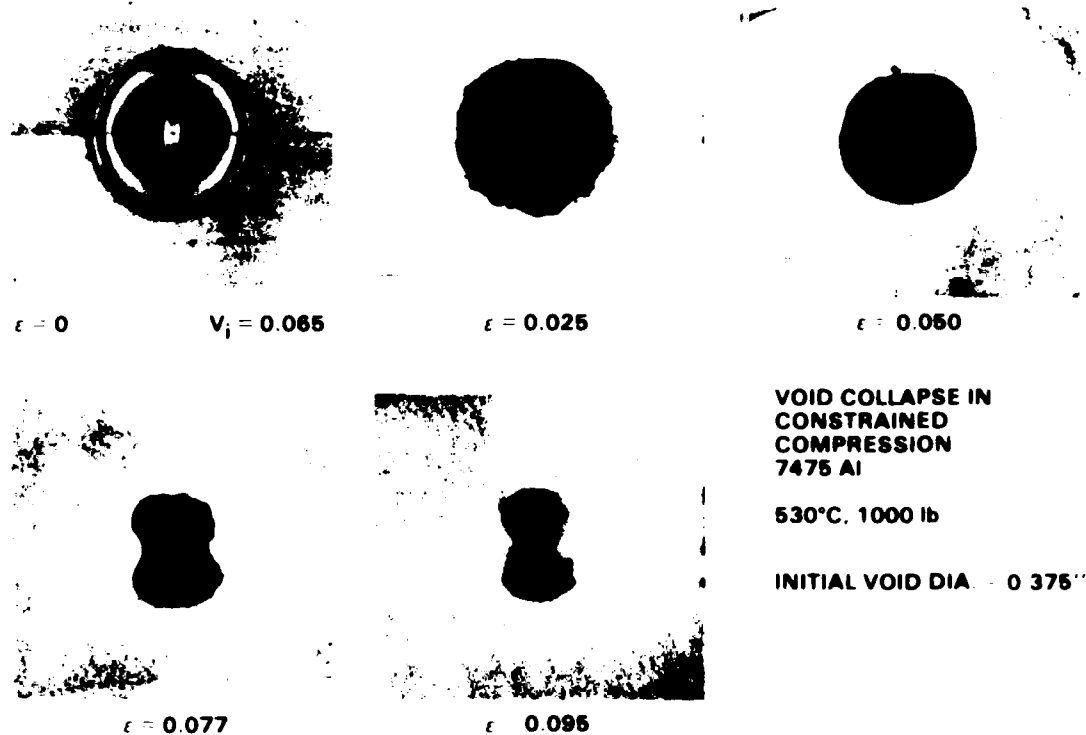


Fig. 4.3-23 Progressive void closure in samples containing premachined spherical voids.

indicate breakup into smaller voids before full consolidation. The void volume measured quantitatively from these as well as the 7075 Al powder compaction study are plotted in Fig. 4.3-24 against analytical data presented previously. The agreement appears to be quite excellent, thereby indicating that these simplistic models are capable of capturing the essential deformation features in powder compaction.

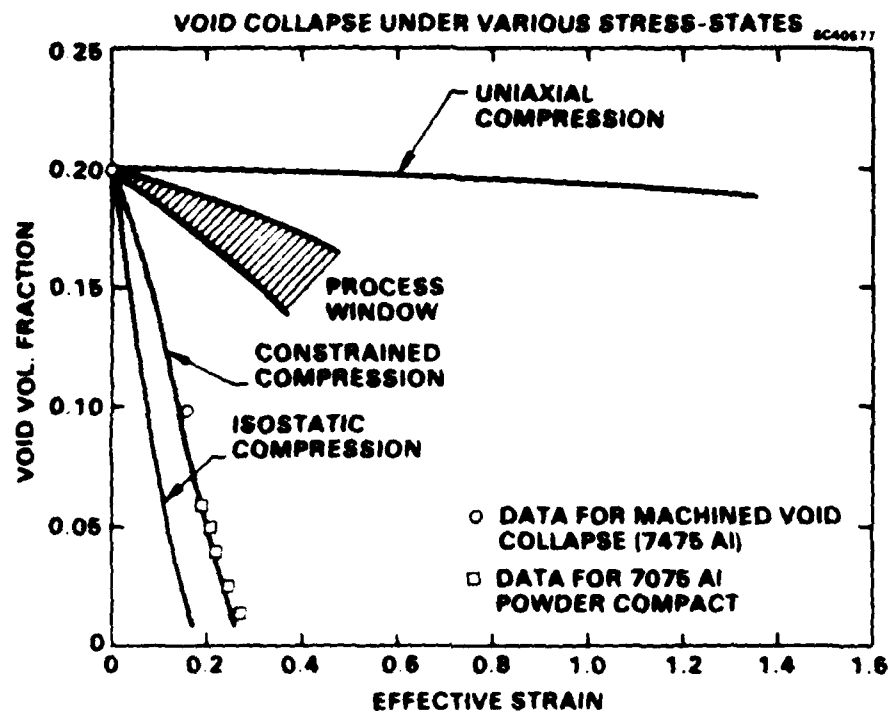


Fig. 4.3-24 Void closure under various stress states - prediction vs experiment.

4.4 Part II - References

1. M.W. Mahoney and C.H. Hamilton, "Superplastic Aluminum Evaluation," AFWAL-TR-81-3051.
2. A.K. Ghosh and C.H. Hamilton, Met. Trans. A 10A, 699 (1979).
3. A.K. Ghosh and C.H. Hamilton, Proc. 5th Int. Conf. on Strength of Metals and Alloys, P. Haasen, ed., Aachen, p. 905, August 1979.
4. A.K. Ghosh, "Deformation of Polycrystals-Mechanisms and Microstructures," Proc. 2nd Int. Symp. on Met. and Mat. Sci., N. Hansen et al, eds., p. 277, September 1981.
5. M.F. Ashby and R.A. Verrall, Acta Metall. 21, 149 (1973).
6. F.R.N. Nabarro, Proc. Conf. Strength of Solids, Phys. Soc. of London, Cambridge, p. 75 (1948).
7. C. Herring, J. Appl. Phys. 21, 437 (1950).



8. R.L. Coble, J. Appl. Phys. 34, 1679 (1963).
9. A. Ball and M. Hutchinson, Met. Sci. J. 3, 1 (1969).
10. A.K. Mukherjee, Mat. Sci. Eng. 8, 83 (1971).
11. A.K. Ghosh and R. Raj, Acta Metall. 29, 607 (1981).
12. R. Raj and A.K. Ghosh, Acta Metall. 29, 283 (1981).
13. N.E. Paton and C.H. Hamilton, U.S. Patent 4,092,181, May 1978.
14. C.H. Hamilton, "Method for Superplastic Forming," U.S. Patent No. 4,354,369, October 1982.
15. A.K. Ghosh, "Slip-Enhanced Diffusional Creep and Superplasticity," in preparation.
16. A.K. Ghosh, "A Model for Static and Dynamic Grain Growth at High Homologous Temperatures," in preparation.
17. A.K. Ghosh, "A Mechanistic Model for Superplastic Flow in Single Phase Materials," in preparation.
18. E. Arzt, M.F. Ashby and R.A. Verral, Acta Met. 31, (12), 1977 (1983).
19. A.K. Mukherjee, J.E. Bird and J.E. Dorn, Trans. Amer. Soc. Metals 62, 155 (1969).
20. D.S. Wilkinson and C.H. C'Aceres, "On Strain-Induced Grain Growth During Superplastic Deformation," Acta. Metall., in press.
21. A.K. Ghosh and R. Raj, Proc. Int. Conf. on Superplasticity, Grenoble, Sept. 1985, B. Bandedet, ed., editions du CNRS, Paris, 1985.
22. A.K. Ghosh, "A Unified View of Superplastic Cavitation Including Hydrostatic Pressure Effects," in preparation.
23. B. Budiansky, J.W. Hutchinson and S. Slutky, Mechanics of Solids, The Rodney Hill 60th Anniversary Volume, H.G. Hopkins and M.J. Sewell, eds., Pergamon Press, Oxford, 1982.
24. P. Lenji and W. Hermal, Powder Metallurgy 24 (2), 93 (1981).



5.0 ACTIVITIES

5.1 Publications

C.G. Rhodes, J.C. Chesnutt and J.A. Wert, "Influence of Microstructure on Fatigue Crack Growth Rate in Beta-Processing Ti-6Al-4V," submitted to Metallurgical Transactions.

C.G. Rhodes and J.C. Chesnutt, "Variations in Fatigue Crack Growth Rates and Load Application in Ti-6Al-4V," in preparation, to be submitted to Metallurgical Transactions.

A.K. Ghosh and R. Raj, Proc. Intl. Conf. on Superplasticity, Grenoble, Sept. 1985, B. Baudelet, Ed., Editions du C.N.R.S., Paris, 1985.

A.K. Ghosh and R. Raj, Acta Met. 34(3), 347 (1986).

A.K. Ghosh, "A Unified View of Superplastic Cavitation Including Hydrostatic Pressure Effects," in preparation.

A.K. Ghosh, "A Mechanistic Model for Superplastic Flow in Single Phase Material," in preparation.

A.K. Ghosh, "A Study of Consolidation of Aluminum Alloy Powder, in preparation.

5.2 Personnel Associated with Research, Part I

Cecil G. Rhodes, Principal Investigator
James C. Chesnutt
John A. Wert
Anita Warner
Robert A. Spurling
Michael Calabrese

5.3 Personnel Associated with Research, Part II

A.K. Ghosh, Principal Investigator
R. Raj, Consultant
L.F. Nevarez
J.M. Curnow
D. Tamir
M. Calabrese

5.4 Interaction (Coupling Activities)

"Effect of Beta Heat-treatment on Microstructure and Fatigue Crack Propagation in Ti-6Al-4V," C.G. Rhodes, J.C. Chesnutt and J.A. Wert, presented at TMS-AIME Annual Meeting, New York (1985).



"Influence of Microstructure on Fatigue Crack Propagation in Beta Heat-Treated Ti-6Al-4V," C.G. Rhodes and J.C. Chesnutt, presented at TMS-AIME Fall Meeting, Toronto (1985).

"Effect of Beta Heat Treatment on Microstructure and Fatigue Crack Propagation in Ti-6Al-4V," J.C. Chesnutt and C.G. Rhodes, presented at AIME Annual Meeting, New Orleans (1986).

"Influence of Transformed Beta Microstructure on Fatigue Crack Growth Rates in Ti-6Al-4V," C.G. Rhodes, J.C. Chesnutt and J.A. Wert, to be presented at TMS-AIME Annual Meeting, Denver (1987).

Discussions with Prof. Rishi Raj of Cornell University several times during 1983 and 1984 are acknowledged. Prof. Raj visited the Science Center during April 1984, when joint work was done.

Discussions with Prof. D. Wilkinson of McMaster University, Canada, June 1983, and A.K. Mukherjee, University of California, Davis, 1984-1986.

A.K. Ghosh, invited presentations in 1983 and 1985, Gordon Research Conferences on Physical Metallurgy, Plymouth, NH. Presentations were based on this research.

Invited papers at several TMS-AIME Symposia based on work performed under this contract.

Discussion with Prof. E. Nes, Norwegian Institute of Technology, Trondheim, Norway, June 1983.

Discussions with Prof. W.D. Nix, Stanford University, several times during 1983-1985.

END

8-87

DTIC